UNIVERSITAT ROVIRA I VIRGILI

DYNAMICS AND STRUCTURE OF LIQUIDS UNDER SPECIAL CONDITIONS: WATER CONFINED IN GIANT POLYOXOMETALATES AND CO2-BRINE MIXTURES

Miquel Alexandre García Ratés

Dipòsit Legal: T. 1457-2011

ADVERTIMENT. La consulta d'aquesta tesi queda condicionada a l'acceptació de les següents condicions d'ús: La difusió d'aquesta tesi per mitjà del servei TDX (www.tesisenxarxa.net) ha estat autoritzada pels titulars dels drets de propietat intel·lectual únicament per a usos privats emmarcats en activitats d'investigació i docència. No s'autoritza la seva reproducció amb finalitats de lucre ni la seva difusió i posada a disposició des d'un lloc aliè al servei TDX. No s'autoritza la presentació del seu contingut en una finestra o marc aliè a TDX (framing). Aquesta reserva de drets afecta tant al resum de presentació de la tesi com als seus continguts. En la utilització o cita de parts de la tesi és obligat indicar el nom de la persona autora.

ADVERTENCIA. La consulta de esta tesis queda condicionada a la aceptación de las siguientes condiciones de uso: La difusión de esta tesis por medio del servicio TDR (www.tesisenred.net) ha sido autorizada por los titulares de los derechos de propiedad intelectual únicamente para usos privados enmarcados en actividades de investigación y docencia. No se autoriza su reproducción con finalidades de lucro ni su difusión y puesta a disposición desde un sitio ajeno al servicio TDR. No se autoriza la presentación de su contenido en una ventana o marco ajeno a TDR (framing). Esta reserva de derechos afecta tanto al resumen de presentación de la tesis como a sus contenidos. En la utilización o cita de partes de la tesis es obligado indicar el nombre de la persona autora.

WARNING. On having consulted this thesis you're accepting the following use conditions: Spreading this thesis by the TDX (www.tesisenxarxa.net) service has been authorized by the titular of the intellectual property rights only for private uses placed in investigation and teaching activities. Reproduction with lucrative aims is not authorized neither its spreading and availability from a site foreign to the TDX service. Introducing its content in a window or frame foreign to the TDX service is not authorized (framing). This rights affect to the presentation summary of the thesis as well as to its contents. In the using or citation of parts of the thesis it's obliged to indicate the name of the author.

Miquel A. Garcia Ratés

Dynamics and structure of liquids under special conditions:
Water confined in giant polyoxometalates and CO_2-brine mixtures

Doctoral Thesis

UNIVERSITAT ROVIRA I VIRGILI

Miquel A. Garcia Ratés

Dynamics and structure of liquids under special conditions:
Water confined in giant polyoxometalates and CO_2-brine mixtures

Doctoral Thesis

Supervised by Dr. Josep Bonet Avalos

Department of Chemical Engineering
Universitat Rovira i Virgili

UNIVERSITAT ROVIRA I VIRGILI

Tarragona
2011

UNIVERSITAT
ROVIRA I VIRGILI
Escola Tècnica Superior d'Enginyeria Química
Departament d'Enginyeria Química
Campus Sescelades,
Avinguda dels Països Catalans, 26
43007 Tarragona (Spain)
Tel: 977 558675
Fax: 977 559621

FAIG CONSTAR que aquest treball titulat "*Dynamics and structure of liquids under special conditions: Water confined in giant polyoxometalates and CO_2-brine mixtures*" que presenta Miquel A. Garcia Ratés per a l'obtenció del títol de Doctor, ha estat realitzat sota la meva direcció al Departament d'Enginyeria Química d'aquesta universitat i que acompleix els requeriments per poder optar a Menció Europea.

Tarragona, 23 de juny de 2011

El director de la tesi doctoral

Dr. Josep Bonet Àvalos

Acknowledgments

First of all, I would like to thank my supervisor Dr. Josep Bonet Avalos who admitted me doing research with him. Without his support, guidance and wide scientific knowledge, this work would have not been possible. I am also grateful to all the members of the Molecular Simulation group in Tarragona, especially to Allan Mackie and Teresa Marmol.

A special thanks to Carles Bo and Pere Miró from the Institute of Chemical Research of Catalonia (ICIQ), both for their scientific guidance and constructive discussions about polyoxometalates.

My sincere gratitude goes to Carlos Nieto Draghi for having supervised my work during the stage at the Institute Français du Pétrole (IFP) at Rueil-Malmaison. I also would like to acknowledge Jean Charles de Hemptinne for his contribution to our calculations. I would like to emphasize my acknowledgments to all the members of the Department of Thermodynamics and Molecular Simulation, especially to Javier Pérez Pellitero, Pierre-Yves Prodhomme, Mireille Lontsi-Fomena, Michelle Aquing, Hedi Amrouche, Theodorus de Bruin, Benoît Creton and Romain Raucoules. I felt like if I was at home during the whole stage.

I also would like to thank all the members of the thesis committee; Drs. Frank Florian Müller Plathe, Giancarlo Franzese, Allan Mackie, Carlos Nieto-Draghi, Josep Maria Poblet, Carles Bo and Ignacio Pagonabarraga for having accepted to supervise this manuscript and the corresponding talk, and to Drs. Javier Pérez-Pellitero and Fabrice Thalmann for accepting the arduous task of being external reporters.

I am also indebted to the Ministerio de Ciencia e Innovación of the Spanish

Government for grant CTQ2008-06469/PPQ and the Programa d'ajuts de Recerca Cooperativa URV/ICIQ 2007 for financial support.

Finally, my special gratitude goes to my parents for their unequivocal support.

List of Figures

List of Tables

Introduction

Real substances, whatever is their phase, are made of molecules composed of atoms. The whole understanding, for instance, of the behavior of a liquid, both at the microscopic and macroscopic scales, is given by the understanding of its microscopic details, as Statistical Mechanics postulates.[1] In this sense, several macroscopic physical properties can be obtained from experiments. Other quantities, however, do not have an experimental setup counterpart, or their measure is not allowed due to the extreme thermodynamic conditions associated. For several industrial applications it is nevertheless important to predict which will be the behavior of those substances under a wide range of thermodynamic conditions. Hence, some parallel alternative to experiments is needed to predict physico-chemical properties.

The increase of computer processing capacity in the last half-century has made computers changing from simple computers with few processors to the so-called *supercomputers*, involving hundreds of processors working ensemble. This capacity of performing a massive number of calculations in short times makes computers suitable for solving problems in the fields of physics, chemistry or biology. The use of computers to calculate physico-chemical properties in molecular systems is referred in the literature as *molecular simulation* or *molecular modeling* techniques.[2,3] These methods depend, at first, on the level of accuracy used for the modeling of the molecules. The most accurate description of molecules involves the treatment of electrons and nuclear cores separately. However, to reduce the computational cost associated to a simulation, *coarse-grained* models are also used. Here, atoms are the molecular units or even groups of atoms are treated as single entities. When, electronic degrees of freedom are explicitly taken into account, a part of the calculations involves solving quantum mechanical equations. When coarse-grained models are used instead, an approximate treatment of such degrees of freedom can be done and the forces acting on the atoms in the system derive from effective potential surfaces called *force fields*.

A well-known computer simulation technique to calculate equilibrium and dynamic properties for molecular systems is the so-called *molecular dynamics* (MD) technique. This technique can be divided into *ab initio* MD methods, where the electronic degrees of freedom are accounted for, and classical MD simulations, where the dynamics of a molecular system as a whole is solved by integrating the classical equations of motion.[4] In this case, the interactions between atoms are calculated from the force field. The obtained quantities are the positions and velocities of all atoms in the system at different times. Hence, this method simulates, in some sense, a real experiment. With these molecular trajectories, microscopic and macroscopic properties are calculated from Statistical Mechanics. Typical MD simulated space- and time scales are those of systems at the nanoscale. As a consequence, MD simulations are clearly appropriate to simulate liquid systems, as the structure and dynamics for those systems are governed by phenomena at these scales.

One of the most studied molecules due to its role in biological and industrial processes is water.[5] The ability of water molecules to form hydrogen bonds (HB) between each other in a cooperative way results, at the macroscopic level, in the so-called anomalies of water, which become evident in many structural and dynamic properties such as its volume, the thermal expansion coefficient, the self-diffusivity, or the viscosity.[6] Water is an excellent solvent for polar and ionic species due to the asymmetry in its charge distribution, but a poor solvent at low temperatures for nonpolar solvents. Due to this capacity of forming hydrogen bonds, water presents a rich phase diagram. However, several regions such as the supercooled region are difficult to understand through experiments due to ice nucleation which can not be always prevented. Water also presents a different structural and dynamic behavior when confined at the nanoscale as compared to its bulk phase. Water confining structures range from graphite channels,[7] carbon nanotubes,[8–10] or reverse micelles, among others.[11–17] The different geometry and internal surface potential of these structures forces water molecules to form a different HB network than in the bulk phase. This fact permits the study of water phases which experimentally are difficult to maintain but which, under confinement, are more easily formed. As some of these confining structures have, for instance, industrial applications, the study of confined water permits to assess the suitability of these molecules for the confinement of other species.

An example of confining molecules are the giant Mo_{132} polyoxometalates.[18,19] These nanocapsules, which are synthesized in the laboratory, have an internal available cavity for host molecules and 20 pores in their surface, which allow molecules to transfer from inside to outside and vice versa. The size of the internal cavity depends on the choice of the internal ligands and also depends on the presence of specific ions closing the pores. Recently, molecular dynamics simulations of water confined inside $Mo_{132}(SO_4)$ and $Mo_{132}(HCO_2)$ polyoxomolybdates have been performed, and the obtained results successfully reproduce the X-ray data giving the positions of water oxygens inside the capsule.[20] However, a detailed analysis of the causes of the different structures in both capsules and the associated dynamics were not done.

In chapter 2 we have studied precisely the structure and dynamics of water confined inside a polyoxomolybdate molecular cluster $Mo_{132}(SO_4)$ metal oxide nanocapsule by means of MD simulations at ambient conditions. Concentric layers of water molecules are observed from radial density profiles of water oxygens inside the cavity. From hydrogen bonding, tetrahedral order parameter, and orientational distribution results, we have suggested that the layered structures should belong to the so-called *buckyball* family. This statement has lead to a redefinition of the proposed structures in ref [20]. An innovative way to study the main modes of motion of water layers and the transfer of water molecules between them has been introduced in this chapter through the principal component analysis of the fluctuation of the number of water molecules in the different layers. The obtained results suggest that the layers oscillate with a given frequency but that the transfer of water molecules between layers rarely occur. We have also studied the relaxation of the HB network at each layer through the power spectra of quantities such as the total dipole moment. In addition, to better understand the dynamics of water molecules inside the $Mo_{132}(SO_4)$ capsule, we have calculated hydrogen-bond and orientational-time correlation functions. The latter has been compared to theoretical and experimental data for reverse micelles, and then, it has permitted to infer the grade of the slowering in water dynamics as compared to water confined in other similar systems.

The effect of the ligand on the structure and dynamics of Mo_{132}(ligand) nanocapsules has been studied in chapter 3. For that purpose we have considered the previous SO_4^{2-} sulfate ligand and also the HCO_2^- formate ligand. As seen from X-ray measurements in ref [20] of water confined in both structures, minor changes in the structure of the internal ligands lead to different water HB networks. Then, the understanding of the causes of these changes is one of the main objectives of this work. We have studied the radial and spatial density profiles of water oxygens in both structures at ambient conditions. Although a given water structure is observed inside the $Mo_{132}(HCO_2)$ capsule, the larger available volume in the cavity makes water not to form the well-defined buckyball structures as observed inside the $Mo_{132}(SO_4)$. However, a detailed structure of how water organizes inside the Mo_{132} cavity when formates functionalize the capsule at $T = 298.15$ K is given in this chapter. In order to understand the suggested layered structures in ref [20] for water inside the $Mo_{132}(HCO_2)$, an MD simulation at $T = 198$ K has also been performed. We have shown that at this low temperature water tends to form buckyball structures similar to those observed inside the $Mo_{132}(SO_4)$. We have compared the translational diffusion of water molecules in both structures. A faster diffusion is observed for water inside the $Mo_{132}(HCO_2)$ as compared to that in the $Mo_{132}(SO_4)$. This situation is directly related to the global hydrogen bond network in the $Mo_{132}(HCO_2)$ capsule. Finally, we have also calculated orientational correlation functions for water molecules when formates are the internal ligand and compared to similar data for reverse micelles of similar size and to the same results obtained in the previous chapter for water in the $Mo_{132}(SO_4)$ capsule. These results can be experimentally tested.

The comparison made in this chapter together with the results obtained in the previous chapter provide a rather complete description of the structure and dynamics of water inside Mo_{132}(ligand) cavities. The choice of the selected ligands results in a quite different dynamics and structure of water molecules at ambient conditions. This study gives the keypoints which cause these differences and provides experimentally measurable data to check the proposed scenario in both capsules and also to check the validity of the models used for both the Mo_{132}(ligand) capsules and water molecules.

The behavior of liquids is not only affected under confinement at the nanoscale, but also in the presence of ions and particular solvents at larger scales. Polar substances as water organize differently around ions than in the bulk. A special case of a molecule whose dynamics gets affected in ionic solutions is carbon dioxide (CO_2). This molecule has a quadrupole moment which interacts with charged species and polar substances. Carbon dioxide has attracted many attention recently due to the need of reducing its emissions to the atmosphere which contribute to the so-called greenhouse effect. The sequestration of CO_2 in deep saline aquifers has become a real option to reduce CO_2 emissions. These deep geological formations involve high pressures, temperatures and salinities.[21,22] The knowledge of the mass diffusion coefficient of CO_2 in brine at different thermodynamic conditions is needed in order to simulate its behavior in these deep formations through reservoir simulation models. In this sense, molecular dynamics simulations permits the calculation of the *Maxwell-Stefan* (MS) diffusion coefficients. These quantities combined with the so-called thermodynamic factor, which can be obtained either from equations of state or from Monte Carlo simulations, permit the calculation of the mass diffusion coefficient or Fick diffusion coefficient of CO_2 in brine.[23–25]

In chapter 4 we calculate CO_2 mass diffusion coefficients in brine at thermodynamic conditions of deep saline aquifers using MD simulations. The potentials for the different species have been taken from the literature.[26–28] We have studied the effect of the temperature, the CO_2 concentration and the salinity on the Maxwell-Stefan diffusion coefficient. Although an effect of the temperature can be observed, no clear trends are observed by changing either CO_2 concentration or salinity. In addition, we have calculated self-diffusion coefficients of CO_2 which show a much lower dispersion as compared to MS or Fick diffusion coefficient of CO_2 in brine. We have also calculated rotational relaxation times of several vectors defined both in water and CO_2 molecules. Here, a clear effect of temperature and salt concentration is observed. Then, we have proposed a correlation between CO_2 self-diffusion coefficients and rotational relaxation times in order to predict mutual diffusion coefficients. This is one of the most important contributions made in this chapter as it provides an alternative way to test the obtained diffusion coefficients using Maxwell-Stefan formalism. Finally, we have also calculated the electrical conductivity of the solution at the same thermodynamic conditions. Here, not only the electrical conductivity is a function of temperature, but it is also a clear function of salinity, increasing when the salt concentration increases. We have not observed an effect with CO_2 concentration for this quantity. The simulated electrical conductivities have been compared at some thermodynamic conditions with Fleury-Deschamps correlation. Although qualitative agreement is observed between both simulation and correlation results, a shift is observed between both results.

The present manuscript is organized as follows: In chapter 1 we first give an overview of the fundamentals needed to describe the dynamics of a physical system and we provide the link between microscopic and macroscopic observables. This part can be skipped by readers who are active in computer simulation or statistical mechanics. In this same chapter, we present the basics of molecular dynamics and describe the different methodologies needed for each step. Although expert readers may understand the physics behind each of the techniques described in this chapter, the particular implementation of the corresponding algorithms have some peculiarities when applied to molecular systems as those modeled in this thesis. Moreover, the discussion of such techniques is quite fragmented in the literature. Hence, the author considers appropriate to discuss this part in detail. Some measurable properties from molecular dynamics data are also included in this chapter. Although particular cases of these properties are defined in detail in the results chapters, we encourage the reading of this part and, particularly, the principal component analysis technique. Finally, we give an small overview of water molecule and polyoxometalates which can be useful to those readers less familiar with the latter molecules.

In this manuscript, two rather different systems are studied; water confined in giant polyoxometalates and CO_2-brine mixtures. Hence, the part of this thesis devoted to the results is divided into two blocks of chapters. On the one hand, the first block involves chapters 2 and 3. Chapter 2 is devoted to the study of the dynamics of encapsulated water inside $Mo_{132}(SO_4)$ cavities. In chapter 3 we have studied the effect of the ligand on the structure and the dynamics of encapsulated water inside Mo_{132} cavities. In order to help the reading of the text, most of the calculated properties for this part are defined in the same chapters. On the other hand, in chapter 4, we address the results for the second system studied in this thesis; CO_2-brine mixtures. In particular, the analysis of the diffusivity and the ionic conductivity of CO_2 in brine is provided. Finally, although the conclusions of each of the studies are described at the end of the corresponding chapters, we have listed the major conclusions in chapter 5.

Contents

Chapter 1

Fundamentals

1.1 Classical mechanics

In a system of N particles whose velocities are far from the speed of light, the dynamics of a particle i follows Newton's equations of motion,[29]

$$\frac{d\vec{r_i}}{dt} = \vec{v_i} = \frac{\vec{p_i}}{m_i} \tag{1.1}$$

$$\frac{d\vec{p_i}}{dt} = \sum_{\substack{j=1 \\ j\neq i}}^{N} \vec{F}_{ji} + \vec{F_i}^{e} \tag{1.2}$$

where $\vec{r_i}$ and $\vec{v_i}$ are the position coordinates of particle i and its velocity, respectively, and $\vec{p_i}$ its momentum. $\vec{F_i}^{e}$ stands for an external force acting on particle i, and $\vec{F}_{ij}$ is the force exerted by particle j on particle i. For conservative forces, $\vec{F}$ derives from a potential $V(r)$,

$$\vec{F} = -\nabla V(r) \tag{1.3}$$

If both internal and external forces derive from a potential, labelled V_{ij} for the former, and V_i^e for the latter, then the total potential energy V is defined as,

$$V = \sum_{\substack{i,j \\ i<j}} V_{ij} + \sum_{i=1}^{N} V_i^e \tag{1.4}$$

The kinetic energy of a system of N particles is,

$$K = \frac{1}{2}\sum_{i=1}^{N} m_i \vec{v_i}^2 \tag{1.5}$$

Then, the total energy of the system is defined as,

$$E = K + V \tag{1.6}$$

However, it is not always enough solving Newton's equations of motion 1.1 and 1.2 as they stand. There can exist additional constraints. For example, the distance between some particles can be fixed, or the particles can be forced to move in a box. Constraints which can be written as follows,

$$f(\vec{r_1}, \ldots, \vec{r_N}, t) = 0 \tag{1.7}$$

are called *holonomous* constraints. When it is not possible to write the constraints in this way, they are called non holonomous constraints. If there exist k equations like eq 1.7, then, instead of dealing with $3N$ positions, is better to introduce $3N-k$ new independent coordinates q_j, called *generalized coordinates.* Generalized coordinates do not have to be necessarily position coordinates, but they can be angles, distances and other variables which are enough to completely describe the dynamics of a constrained system. Real and generalized coordinates can be transformed. If a new quantity L, called *Lagrangian* of the system, independent of the chosen set of generalized coordinates, is introduced such that,[29]

$$L \equiv K - V \tag{1.8}$$

then, it can be demonstrated that the dynamics of the given set of generalized coordinates is described by the so-called Euler-Lagrange equations

$$\frac{d}{dt}\left(\frac{\partial L}{\partial \dot{q_j}}\right) - \frac{\partial L}{\partial q_j} = 0 \tag{1.9}$$

A conjugate momentum p_j is related to L as follows,

$$p_j = \frac{\partial L}{\partial \dot{q_j}} \tag{1.10}$$

$$\dot{p_j} = \frac{d}{dt}\left(\frac{\partial L}{\partial \dot{q_j}}\right) = \frac{\partial L}{\partial q_j} \tag{1.11}$$

An analogous way to derive the equations of motion for the pair (q_j, p_j) of conjugate variables is done by defining a new quantity called Hamiltonian, H, such that,[29]

$$H = \sum_j \dot{q}_j p_j - L(q_j, \dot{q}_j, t) \tag{1.12}$$

The Hamiltonian has always to be written in terms of q, and p. If the equations defining the relationships between real and generalized coordinated do not depend explicitly on time and if the forces derive from a potential which do not depend on $\dot{q_j}$, the Hamiltonian gives directly the energy of the system as defined in eq 1.6. A set of canonic equations of hamilton are derived from H as follows,

$$\dot{q_j} = \frac{\partial H}{\partial p_j} \qquad , \qquad \dot{p_j} = -\frac{\partial H}{\partial q_j} \tag{1.13}$$

When non holonomous constraints are present in the system, then, eq 1.9 can be generalized to

$$\frac{d}{dt}\left(\frac{\partial L}{\partial q_j}\right) - \frac{\partial L}{\partial q_j} = G_j \quad , \quad j = 1, \ldots, k \tag{1.14}$$

where G_j are the generalized forces, also named constraining forces, and k is the number of generalized coordinates. The effect of G is that of an external force maintaining the constraints in the system. Eq. 1.14 is reasonably treated when the non holonomous constraints are written as,

$$\sum_{j=1}^{k} a_{lj} dq_j + a_{lt} dt = 0 \tag{1.15}$$

Here a_{lj} and a_{lt} are coefficients which can be functions of q and time. The index l indicates that there can be more than an equation like 1.15. We denote by k' the total number of these equations. The generalized forces, then, can be written in terms of the coefficients a_{lj} and a set of Lagrangian multipliers λ as,

$$G_j = \sum_{l=1}^{k'} \lambda_l a_{lj} \tag{1.16}$$

If holonomous constraints are present in the system, it is also possible to use the concept of generalized force. In that case, if the constraint is given by a set of k equations like eq 1.7, then it can be demonstrated that,[29]

$$a_{lj} = \frac{\partial f}{\partial q_j} \quad , \quad a_{lt} = \frac{\partial f}{\partial t} \tag{1.17}$$

With these quantities, it is possible to obtain the value of the Lagrangian multipliers, λ, satisfying the holonomous constraints in the system from eqs 1.16 and 1.14.

1.2 Statistical mechanics

Statistical Mechanics aims at modeling and predicting the properties of materials from the behavior of the atoms and molecules that comprise them. In this subsection, we give the basis of statistical mechanics and we show how macroscopical measurable properties can be obtained from microscopical variables.

1.2.1 Basics

Let's have a system composed of N particles confined in a volume V. The total energy E of the system depends on the energy of the particles, and the interaction between them. In a typical physical system, N is of the order of the Avogadro number, $N_A \approx 10^{23}$, and, hence, we can adopt the thermodynamic limit, $N \to \infty$, and $V \to \infty$ with N/V finite. In this limit, the total energy of the system can be regarded as a continuous variable. The specification of the values of N, V, E defines a *macrostate* (N, V, E) of the system. However, there are multiple ways in which the N particles can arrange to give a total energy E. Each of these ways is called a *microstate* of the system. The number of possible microstates compatible with a macrostate (N, V, E) is denoted by $\Omega(N, V, E)$. A microstate is defined by specifying the set of positions $\vec{r}^N$ and momenta $\vec{p}^N$ of all the particles in the system. This requires the specification of $3N$ position coordinates and $3N$ momentum coordinates. This set of possible coordinates $\Gamma = (\vec{r}^N, \vec{p}^N)$ can be regarded as a point in a $6N$-dimensional space called *phase space*. A phase space point follows a trajectory given by eq 1.13.

The basic assumption of statistical mechanics is that, at equilibrium, a system, for instance, with fixed N, V, and E, is equally likely to be found in any of the $\Omega(N, V, E)$ microstates. If we release internal constraints of an isolated system, the most probable final macrostate will be that with the largest number of microstates. This state is known as the equilibrium state of the system. It can be shown that the condition for equilibrium between the parts is that they share the observable[1]

$$\beta = \left(\frac{\partial \ln \Omega(N, V, E)}{\partial E} \right)_{N,V,E} \tag{1.18}$$

where $\beta = 1/k_B T$, and k_B is Boltzmann's constant, which in S.I. units has the value $1.38066 \cdot 10^{-23}$ J/K. If S is the thermodynamic entropy of the system, the second law of thermodynamics states that the energy of a system with N, V and E is at is maximum when the system is in thermal equilibrium. It can be demonstrated that the entropy of our system follows from the fundamental equation

$$S(N, V, E) = k_B \ln \Omega(N, V, E) \tag{1.19}$$

Notice that if the macrostate (N, V, E) has only one microstate, then $S = 0$. Several thermodynamical variables can be then obtained by derivatives of the entropy. However, one does not know a priori $\Omega(N, V, E)$. If we consider a system with fixed N, V, and E values, then, as time passes, the system will change from one microstate to another. We can consider at a single instant of time, several systems, being each of them a microstate of the macrostate characterizing the original system. This collection is called *ensemble*. When N, V, and E are constant, the resulting ensemble is known as *microcanonical ensemble*. In real experiments, however it is hardly to control the total energy. It is much simpler to control the temperature by coupling our system to a heat reservoir keeping fixed the temperature. In this case, the macrostate of the system is defined through N, V and T and the ensemble is referred to as a *canonical ensemble*. Other ensembles are the isobaric-isothermal ensemble or NPT ensemble where N, P and T are held constant, or the grand-canonical ensemble, in which our system can exchange both energy and particles with a reservoir.

If we select a particular ensemble, then, at any time, its members will occupy different points in the phase space associated to each of the microstates. Then, it is meaningful to define a *density function* $\rho_\Gamma(\vec{r}^N, \vec{p}^N; t)$ giving the number of members of the ensemble in the volume element $d\Gamma = d\vec{r}^N d\vec{p}^N$ around the point $\Gamma = (\vec{r}^N, \vec{p}^N)$ of the phase space. In fact,this function gives a measure of the distribution of members of the ensemble over the possible microstates.

We can define an ensemble average $\langle f \rangle$ of a physical quantity f by using ρ_Γ as follows,

$$\langle f \rangle = \frac{\int f(r,p)\rho_\Gamma(q,p;t) d\vec{r}^N d\vec{p}^N}{\int \rho_\Gamma(q,p;t) d\vec{r}^N d\vec{p}^N} \tag{1.20}$$

When a system is in thermal equilibrium ρ_Γ is independent of time. However, one may have a large set of data measured at different times. In this case, if we employ a sufficiently long interval of time, the system may be expected to pass through almost all possible microstates and the averaging process depends only upon the macrostate of the system. Hence, ensemble averages can be replaced by time averages.

$$\langle f \rangle_{\text{eq}} = \lim_{t\to\infty} \frac{1}{t} \int_0^\infty f(t')dt' \tag{1.21}$$

This statement is known as *ergodic hypothesis*. Although it is not the interest of this section, ensemble averages are used in Monte Carlo methods, while time averages are calculated in molecular dynamics methods as described in Section 1.3.

In this study, we work with NVT and NPT ensembles. In the following subsections, we give the basics to compute properties from those ensembles.

1.2.2 Canonical ensemble

In the canonical ensemble, we have a system with constant volume V, and number of particles N immersed in a very large heat reservoir at temperature T. At equilibrium, our system reaches the temperature T, but its energy can change due tot he contact with the bath. As we said before, for sufficient large systems with a large number of particles, one may regard the total energy of our system, E, as a continuous variable. In this case, one can define $P(E)dE$ as being the probability that a given system in the canonical ensemble has a energy in the range $(E, E+dE)$. This probability can be assumed to be proportional to the number of microstates $\Omega(N,V,E)$, $P(E)dE \propto \Omega(E)$, as the larger the number of available microstates consistent with macrostate (N,V,E), the larger the probability for the system to have an energy E. From this assumption, using eq 1.18 and doing an expansion of $\ln\Omega(N,V,E)$ we obtain that,[1]

$$P(E)dE \propto \exp(-\beta E)g(E)dE \tag{1.22}$$

where $\exp(-\beta E)$ is the so-called *Boltzmann factor*, and $g(E)$ is the *density of states* around energy E. The normalized equation for the probability is then,

$$P(E)dE = \frac{\exp(-\beta E)g(E)dE}{\int_0^\infty \exp(-\beta E)g(E)dE} = \frac{\exp(-\beta E)g(E)dE}{Q_N(V,T)} \tag{1.23}$$

The denominator $Q_N(V,T)$ is the partition function. The integration in eq 1.23 is computed over energy states, however, we usually have positions and momenta of a set of particles, and we may be interested in replacing those sums by integrations over phase space. In this case, the function measuring the probability of finding a microstate around phase space point $(\vec{r}^N, \vec{p}^N)$ is the density function $\rho_\Gamma(\vec{r}^N, \vec{p}^N)$. Similarly to eq 1.22 we have that,

$$\rho_\Gamma \propto \exp\{-\beta H(\vec{r}^N \vec{p}^N)\} \tag{1.24}$$

where H is the Hamiltonian of the system. Hence, the ensemble average of a quantity f in the canonical ensemble, can be computed from the following equation,

$$\langle f \rangle = \frac{\int f(\vec{r}^N, \vec{p}^N)\exp(-\beta H(\vec{r}^N, \vec{p}^N))d\vec{r}^N d\vec{p}^N}{N! h^3 Q_N(V,T)} \tag{1.25}$$

where h is the Planck's constant. As the Hamiltonian is a sum of a kinetic term and a potential term, the partition function $Q_N(V,T)$ can be expressed as the product of a kinetic term Q_{kin} which is integrated over the momenta, and a potential Q_{pot} term which depends only on the positions of atoms. For the kinetic term we have that,[1]

$$Q_{\mathrm{kin}} = \frac{1}{N!\Lambda^{3N}} \tag{1.26}$$

where Λ stands for the de Broglie wavelength $\Lambda = h/\sqrt{2\pi m k_B T}$. The factor $1/N!h^{3N}$ is the classical approximation of the quantum mechanical partition function, which includes the indiscernibility of the particles as well as the minimal volume in phase space. The potential term also called configurational integral is calculated from the particular form for the potential $V(r)$ between particles,

$$Q_{\mathrm{pot}} = \int \exp(-\beta V(\vec{r}^N))d\vec{r}^N \tag{1.27}$$

A thermodynamic quantity which can be obtained from the partition function is the Helmholtz free energy A, given by

$$A(N,V,T) = -k_B T \ln Q_N(V,T) \tag{1.28}$$

This quantity is very important as many thermodynamic quantities like the internal energy U, the chemical potential μ, the pressure P or the entropy S of a given system can be obtained from derivatives of eq 1.28.

In a computer simulation, there exist several methods to keep the system at constant temperature. These methods are described in Section 1.3.3.1. We can estimate the temperature of our system from the theorem of *equipartition of energy*. From this theorem, we know that each quadratic term in the Hamiltonian makes a contribution of $\frac{1}{2}k_B T$ towards the internal energy of the system. The kinetic energy depends quadratically on the velocities of the atoms in the system. Then, its average is related to the temperature of the system through the following equation,

$$\langle \frac{1}{2}mv^2 \rangle = \frac{1}{2}k_B T \tag{1.29}$$

If we have a set of data measured at different times, the ensemble average has to be replaced by a time average as known from the ergodic hypothesis, and the temperature is estimated

$$\bar{T} = \sum_{i=1}^{N} \frac{m_i v_i^2}{k_B N_d} \tag{1.30}$$

where N_d is the number of degrees of freedom for a system of N particles. If the number of particles goes to infinity, $\bar{T}$ tends to the thermodynamic temperature of the system.

1.2.3 Isothermal-isobaric ensemble

In the isothermal-isobaric ensemble, the temperature T of the system is maintained by coupling it with a heat reservoir, and the pressure P is held constant by changing the volume V of the system. It can be shown that in this ensemble the density function ρ_Γ is such that,

$$\rho_\Gamma \propto \exp\{-\beta[H(\vec{r}^N, \vec{p}^N) + PV]\} \tag{1.31}$$

The appropriate isothermal-isobaric partition function $Q_N(P,T)$ is given by

$$\begin{aligned} Q_N(P,T) &= \frac{\beta P}{h^{3N} N!} \int_0^\infty dV \int\int \exp\{-\beta[H(\vec{r}^N, \vec{p}^N) + PV]\} d\vec{r}^N d\vec{p}^N = \\ &= \beta P \int_0^\infty \exp(-\beta PV) Q_N(V,T) dV \end{aligned} \tag{1.32}$$

The factor βP is included to make $Q_N(P,T)$ dimensionless. The link between macroscopic observables is made through the relation of the isobaric-isothermal partition function with the Gibbs, free energy, G

$$G = -k_B T \ln Q_N(P,T) \tag{1.33}$$

The pressure can be computed numerically through the positions of the atoms and the forces acting on them,

$$P = \frac{1}{3V} \left\langle \sum_{i=1}^{N} m_i \vec{v_i}^2 + \sum_{i>j} \vec{r_{ij}} \vec{F_{ij}} \right\rangle \tag{1.34}$$

and, hence, it can be controlled, for instance, in a computer simulation at each time. The numerical method used to along this study to hold the temperature and the pressure constant is given in Section 1.3.3.2.

1.3 Molecular dynamics

Computer simulations of real systems involve a large variety of methods depending on the time and length scales of the processes involved. As finite computational resources are used when performing molecular simulations, there is a competition between the desired level of accuracy in the representation of our system and the total CPU time required to obtain significative results. For systems at the nanoscale, that is, involving time scales $\approx 10^{-15} - 10^{-9}$ s, and length scales $\approx 0.1 - 10$ nm, there are two main techniques: Monte Carlo methods (MC), and molecular dynamics techniques (MD).[2] MC methods are stochastic methods in which the configuration of a physical system is made to evolve according to a stochastic process in which the transition probability is such that the Markov chain leads to $\Pi = \exp(-\beta H)/Q$ as its unique probability distribution.[30] The main idea under MC methods is to start from a configuration of the system and generate successive new configurations which are accepted or rejected according to a particular criteria, which usually depends on the ratio of the Boltzmann factors between old and new configurations. When equilibrium has been reached, averages of some properties over different configurations are calculated. Nevertheless, these averages do not correspond to time averages but to ensemble averages. Hence, the dynamics of the system does not correspond to real dynamics and dynamic quantities such as time correlations or transport coefficients cannot be computed from a pure MC method. When we are interested in studying the structure and dynamics of a given system at the nanoscale, it is better to use MD simulation techniques. Molecular dynamics (MD) is a technique for the calculation of the motion of molecular systems at liquid, solid or gaseous phase from the integration of classical equations of motion. From a set of initial conditions for the set of phase space coordinates $(\vec{r}^N, \vec{p}^N)$, and from the knowledge of the interaction forces between atoms, given a phase space point, its dynamics in time is straightforwardly obtained. As we have seen in Section 1.2.1, given a set of long time trajectories for $(\vec{r}^N, \vec{p}^N)$, equilibrium and transport properties can be computed by averaging over the time-evolved phase space coordinates. Hence, once the system to study is chosen at the desired thermodynamic conditions, average properties are obtained in an MD simulation.

The basic structure of a MD program is as follows:

1. Input parameters are introduced and read by the MD program. These include:
    - Number of N atoms present, its type and number of molecules they form.
    - Parameters for the interactions between atoms and molecules.
    - Thermodynamic conditions.
    - Details for the simulation box where atoms are placed.
    - Chosen algorithm to integrate the equations of motion in the chosen ensemble and associated details.

2. Initial values for the positions and momenta for the N atoms are read.
3. Forces between particles are computed.
4. Equations of motion for the different degrees of freedom in the system are integrated in time. Notice that steps 3 and 4 are computed until the simulation ends in a loop structure.
5. Average properties are calculated from trajectories.

In this thesis, we have studied the structure and dynamics of systems at the nanoscale, then, the use of these techniques is justified. Along the whole study, the MD trajectories have been generated from DLPOLY v2.19 code, developed at Daresbury Laboratory.[31]

The scheme presented above is quite simple and, in particular, steps 3 and 4 can differ substantially depending on the molecules present in the system, the kind of interactions between them, or the ensemble in which the system is simulated. Hence, in the following subsections, we explain in more detail the most important features of an MD simulations, giving a special importance to the used methods along this study.

1.3.1 Boundary conditions

Real experiments involve a large amount of atoms as only 1 mol of a substance contains N_{A} particles. In an MD simulation, however, the motion of atoms is simulated in a box (*simulation box*) which can adopt different geometries such as cubic, hexagonal or dodecahedral. The number of atoms in the simulation box ranges from 10^2 to 10^8 atoms. If the system to study is reduced to the simulation box and the particles inside, then, we will have an undesired effect arising from the boundaries of the box as an important number of particles will interact with them. A solution is to apply periodic boundary conditions (PBC). That is, replicas of the simulation box are placed along the three coordinate axes. Hence, if a particle i is at position $\vec{r_i}$ in a cubic cell, according to some system of reference, replicas of atom i are placed at positions $\vec{r_i} + \vec{n}L$, where $\vec{n} = (n_x, n_y, n_z)$ is a vector whose components are integers and L is the box side length. See that $\vec{n} = \vec{0}$ corresponds to the main cell. Nevertheless, for such an infinite system, the calculation of properties such as the total energy, or the total force acting on a given particle, involves computing an infinite sum

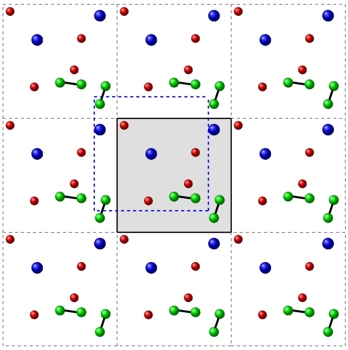

Figure 1.1: Scheme of periodic boundary conditions in 2D. The simulation box, or main cell, is shown in gray. For short range interactions, particles only interact with the nearest image of the other atoms. For example, the blue atom located at the left of the main cell only interacts with those atoms located inside the blue dashed square.

over all particles in the main cell and all its replicas. As we will see in Section 1.3.4.3, the interaction between particles can be divided into short-ranged, and long-ranged, depending on the distance at which these interactions vanish. For short-ranged, the contribution to the energy coming from a particle i is mainly due to the interaction with its neighbors at a distance closer to a cut-off r_c. In that case, the short-range energy of the N particles system, which is assumed to be pairwise additive, is written as,

$$U_{sh} = \sum_{i<j} u_c(r_{ij}) + u_{r>r_c} \tag{1.35}$$

where u_c is the truncated potential, and $u_{r>r_c}$ is the contribution of those particles located at $r > r_c$. Different approaches can be used to truncate short range interactions. In this study, we use the so-called *minimum image convention* where each atom in the main cell interacts with the nearest image of every atom excepts its own image. Then, r_c has to be chosen $r_c < L/2$. As molecules are considered along this study, a fraction of a given molecule can cross a boundary and appear on the other side of the box. In this case, for a given atom i, the nearest image of an atom j is located at a position, $\vec{r_{j'}}$ given by

$$\vec{r_{j'}} = \vec{r_j} - L \cdot \mathrm{nint}\left[\frac{\vec{r_j} - \vec{r_i}}{L}\right] \tag{1.36}$$

where $\vec{r_j}$ is the position of atom j in the main cell, and $\mathrm{nint}(x)$ refers to the nearest integer of x.

For systems which are spatially correlated even at a long distance ξ, the choice of a box side $L < \xi$ leads to unphysical effects in some of the studied magnitudes. In this sense, for strongly correlated systems or highly dense systems, a solution is to perform different simulations changing the volume of the simulation box to see if important changes are observed in the calculated properties, or to find how they scale with the size of the system.[32] For the systems to study along this work, temperature is high enough to avoid any significant spatial correlation at a distance larger than L, however, different system sizes have been chosen as to avoid undesired finite size artifacts in our results.

1.3.2 Integrating the equations of motion

Once the forces acting on the particles in the system and, hence, their accelerations, have been derived, the equations of motion can be integrated. For molecular systems, however, the nature of the bonds between atoms involves using slightly different approaches to obtain the correct dynamics for each molecule. Molecules can be separated into three groups, depending on the nature of their bonds:

1. Molecules whose bonds are entirely described by the potentials of Sec. 1.3.4.
2. Molecules with constraints, such as bond angles or bond lengths, in some of the bonds or parts of the molecule.
3. Rigid molecules.

In the present study we have simulated systems where the three kind of molecules are present. Then, in this section, we describe the methodology used to integrate the equations of motion for each case.

1.3.2.1 Translational motion

Velocities and positions of the particles in time are obtained integrating Newton's equations of motion. There exist different algorithms for that purpose. One of the simplest and most widely used algorithms is the Verlet algorithm.[2,3] To derive Verlet algorithm, we start by doing Taylor expansions of the position $\vec{r}$ of a particle around time t,

$$\vec{r}(t+\Delta t) = \vec{r}(t) + \vec{v}(t)\Delta t + \frac{\vec{a}(t)}{2}(\Delta t)^2 + \frac{1}{3!}\frac{d^3\vec{r}(t)}{dt^3}(\Delta t)^3 + \mathcal{O}(\Delta t)^4 + \dots \tag{1.37}$$

$$\vec{r}(t-\Delta t) = \vec{r}(t) - \vec{v}(t)\Delta t + \frac{\vec{a}(t)}{2}(\Delta t)^2 - \frac{1}{3!}\frac{d^3\vec{r}(t)}{dt^3}(\Delta t)^3 + \mathcal{O}(\Delta t)^4 + \dots \tag{1.38}$$

where Δt is the chosen timestep. The position, of the particle at time $t + \Delta t$ is obtained then by summing eqs 1.37 and 1.38,

$$\vec{r}(t+\Delta t) = 2\vec{r}(t) - \vec{r}(t-\Delta t) + \vec{a}(t)(\Delta t)^2 + \mathcal{O}(\Delta t)^4 \tag{1.39}$$

where the terms of order $(\Delta t)^3$ have cancelled out. See that no velocities are needed to compute the new position of the particle at time $t + \Delta t$. However, it may be useful to have the velocities $\vec{v}$ of the particles in order to compute the kinetic energy of the system. From the definition of the time derivative of a function, the velocity of a particle at time t is given by

$$\vec{v}(t) = \frac{\vec{r}(t+\Delta t) - \vec{r}(t-\Delta t)}{2\Delta t} + \mathcal{O}(\Delta t)^2 \tag{1.40}$$

The Verlet algorithm is time-reversible as it can be see from eq 1.39. At the same time, if we consider, at a fixed time, the set of phase space points compatible with a given energy E, filling a hyper volume Ω, and let them evolve following Verlet equation of motion, the volume after a given time t' will still be Ω. This area-preservation is an important property of this algorithm leading to little energy drift for long time simulations. If no long time steps are chosen, Verlet algorithm is simple, fast and gives good average system properties when the time step is small. However, we need to store the positions of a particle at three different time steps to compute velocities at time t. A modification of this algorithm which solves this problem is the leap-frog algorithm.[2,3] First, we obtain the values for the velocities at $t \pm \Delta/2$ from the definition of the time derivative,

$$\vec{v}(t-\Delta t/2) = \frac{\vec{r}(t) - \vec{r}(t-\Delta t)}{\Delta t} \tag{1.41}$$

$$\vec{v}(t+\Delta t/2) = \frac{\vec{r}(t+\Delta t) - \vec{r}(t)}{\Delta t} \tag{1.42}$$

From the last equation, the positions at time $t + \Delta t$ are

$$\vec{r}(t + \Delta t) = \vec{r}(t) + \Delta t \vec{v}(t + \Delta t/2) \tag{1.43}$$

Subtracting eq 1.41 to eq 1.42 and combining with eq 1.39, the velocities of the particles are written as follows,

$$\vec{v}(t + \Delta t/2) = \vec{v}(t - \Delta t/2) + \vec{a}(t)\Delta t \tag{1.44}$$

Then, positions are calculated at times $t-\Delta t, t, t+\Delta t, t+2\Delta t \dots$, while velocities are computed a half step behind. The kinetic energy of the system can also be evaluated with the leap-frog algorithm from velocities at time t calculated as,

$$\vec{v}(t) = \frac{\vec{v}(t + \Delta t/2) - \vec{v}(t - \Delta t/2)}{2\Delta t} \tag{1.45}$$

Due to the symmetric form of the leap-frog algorithm, it is time reversible, and also preserves phase space volume. Within this study we have used the leap-frog algorithm to integrate the translational equations of motion both in the NVT and NPT ensembles as we will see later.

As said above, single ions or molecules, whose bonds are described by stretching potentials (see Sec. 1.3.4.2), follow a dynamics calculated from the leap-frog algorithm. In that case, there is no need to define rotational equations of motion as in other systems.

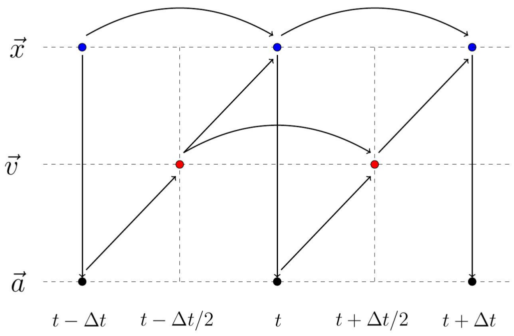

Figure 1.2: Scheme of the leap frog algorithm.

1.3.2.2 Constraints; shake algorithm

Stretching of chemical bonds in polyatomic molecules requires very small timesteps for the integration of the equations of motion. This makes the total time for an MD simulation much larger than in the case where only translational or/and rotational degrees of freedom are considered. At the same time, the quantum nature of some of these bonds makes the use of classical potentials inappropriate to predict some of the properties. The adopted solution, if classical simulations are performed, is to freeze these vibrational degrees of freedom constraining some of the distances between the atoms in the molecules. In this subsection, we introduce the procedure used along this study to include the constraints in the integration of the equations of motion.

Let consider a system of N atoms subject to p constraints. The constraining, in this case, is the distance between two given atoms i, and j,

$$C_k(r_i, r_j) = \vec{r_{ij}}^{\,2} - d_{ij}^2 = 0 \qquad , \qquad k = 1, \ldots, p \tag{1.46}$$

where d_{ij} are the rigid bond distances between atoms i and j. In an N particle system subjected to a number of constraints, there exist two kind of forces which act on each atom i. On the one hand, the force $\vec{F_i}$ derived from the potential energy, and on the second hand, the constraining force $\vec{G_i}$ maintaining the constraints, if they exist, to which atom i is subjected. The constraining force can be written as (see eq 1.16, and eq 1.17),

$$\vec{G_i} = -\sum_{j=1}^{p} \lambda_j \frac{\partial C_j}{\partial \vec{r_i}} \tag{1.47}$$

where λ_j is a Lagrangian multiplier. Then, the equations of motion for each atom i contain the contribution of the two kinds of forces,

$$m_i \frac{d^2 \vec{r_i}}{dt^2} = \vec{F_i} + \vec{G_i} \tag{1.48}$$

The most used method to consider the constraining forces in the equations of motion is the shake method.[33] Firstly, the method uses the Verlet algorithm to obtain a provisional set of positions, $\vec{r_i}^{p}$ for each atom i without considering the constraining forces,

$$\vec{r_i}^{p}(t + \Delta t) = 2\vec{r_i}(t) - \vec{r_i}(t - \Delta t) + \frac{\vec{F_i}}{m_i} \Delta t^2 \tag{1.49}$$

This provisional positions are corrected, then, to obtain the positions at $\vec{r_i}(t+\Delta t)$. To do this the whole expression for the resultant force acting on particle i has to be included in the Verlet integrator equation for positions as follows,

$$\vec{r_i}(t+\Delta t) = \vec{r_i}^p(t+\Delta t) - \frac{\Delta t^2}{m_i}\sum_{j=1}^{p}\lambda_j \frac{\partial C_j(t)}{\partial \vec{r_i}} \tag{1.50}$$

From eq 1.46 it can be easily deduced that,

$$\frac{\partial C_k(r_i,r_j)}{\partial \vec{r_i}} = -2\vec{r_{ij}} \qquad , \qquad \frac{\partial C_k(r_i,r_j)}{\partial \vec{r_j}} = 2\vec{r_{ij}} \tag{1.51}$$

If we put the values of these derivatives in eq 1.50, and combine the resulting equation with eq 1.46, we would obtain the p eigenvalues. However, this process would be computationally very expensive. However, for a pair of constrained atoms i and j, it can be shown through eqs 1.46-1.51 that the Lagrangian multiplier λ has the following expression,

$$\lambda = \frac{(\vec{r_{ij}}^p(t+\Delta t))^2 - d_{ij}^2}{4(m_i^{-1}+m_j^{-1})\Delta t^2 \vec{r_{ij}}^p(t+\Delta t)\cdot \vec{r_{ij}}(t)} \tag{1.52}$$

Shake method uses this result to correct the positions of the different pairs of atoms (i,j) in an iterative process until the distances $\vec{r_{ij}}$ converge to the desired d_{ij} with a given tolerance δ. An scheme of the shake method is as follows,

1. For all possible constrained pairs $(i-j)$, positions $\vec{r_i}^p(t+\Delta t)$ and $\vec{r_j}^p(t+\Delta t)$ are calculated using Verlet algorithm through eq 1.49.
2. The corresponding eigenvalue λ for each pair is calculated through eq 1.52.
3. Positions $\vec{r_i}(t+\Delta t)$, and $\vec{r_j}(t+\Delta t)$ are corrected with the obtained eigenvalue using eq 1.50.
4. If for all the pairs $(i-j)$, $|\vec{r_{ij}}^2 - d_{ij}^2| \leq \delta$, then we go to point 5, otherwise, if $|\vec{r_{ij}}^2 - d_{ij}^2| > \delta$ for some pair $(i-j)$ then we return to point 1.
5. Corrected positions are taken as new positions at $t+\Delta t$. Velocities $\vec{v_i}(t+\Delta t/2)$, and $\vec{v_i}(t)$ are then calculated through the leap frog equations of motion. New positions $\vec{r_i}(t+2\Delta t)$ are calculated.

Tolerances δ are commonly chosen in the range $[10^{-8}, 10^{-4}]$.

1.3.2.3 Rigid body

The use of the shake algorithm to constraint bonds in molecules is recommended when the number of constraints is small or when the molecule has a simple geometry. For molecules such as planar rings, the number of constraints exceeds the number of bonds in the molecule to obtain planarity. In that case, the process of maintaining the constraints becomes very slow, and not always converging, as usually, tolerances are chosen small. The alternative is to consider the molecule as a rigid body. A rigid body can be defined as a collection of material points where the distance of every pair of points remains constant during its dynamics. To correctly describe the motion of a rigid body, it has to be separated into a translation of its center of mass (CM), and a rotation around it.[29] For a rigid body, in our case, a molecule with N_a atoms, the position of the center of mass (CM) is given by,

$$\vec{R}_{\mathrm{CM}} = \frac{\sum_{i=1}^{N_a} \vec{r_i} m_i}{\sum_{i=1}^{N_a} m_i} \tag{1.53}$$

The CM moves with a translational velocity, $\vec{V}_{\mathrm{CM}}$, defined by,

$$\vec{V}_{\mathrm{CM}} = \frac{\sum_{i=1}^{N_a} \vec{v_i} m_i}{\sum_{i=1}^{N_a} m_i} \tag{1.54}$$

Hence, if the resulting force acting on the CM, $\vec{F}_{\mathrm{CM}}$, is the sum of the forces, $\vec{F_i}$, acting on each atom i of the molecule,

$$\vec{F}_{\mathrm{CM}} = \sum_{i=1}^{N_a} \vec{F_i} \tag{1.55}$$

then, the translational dynamics of a rigid body is obtained, in an MD simulation, by integrating the associated equation of motion with the corresponding algorithm, which in our case is the leapfrog algorithm as described in Section 1.3.2.1.

The orientation of a rigid body, can be described by the so-called *Euler angles*; ϕ, θ, and ψ.[29] It is possible to transform a cartesian coordinate system to another by three successive rotations according to the Euler angles in the appropriate order. If we call $\vec{r_l}$, the position of an atoms in the rigid body, relative to its CM, seen in a frame located in the body (local frame), and $\vec{r_e}$ the same position relative to the CM of the rigid body, but in an external frame of reference, then the effect of the three rotations by the Euler angles can be mathematically treated as a rotation matrix **A** which acts on the local frame to give the position in the external frame,

$$\vec{r_e} = \mathbf{A} \cdot \vec{r_l} \tag{1.56}$$

The form of the matrix **A** (not shown), involves the product of many trigonometric functions which makes its calculation quite expensive. The same matrix can be written in terms of quaternions $\vec{q} = (q_0, q_1, q_2, q_3)$. The four components are function of the Euler angles,

$$q_0 = \cos\frac{\theta}{2}\cos\left(\frac{\phi+\psi}{2}\right) \quad , \quad q_1 = \sin\frac{\theta}{2}\cos\left(\frac{\phi-\psi}{2}\right) \tag{1.57}$$

$$q_2 = \sin\frac{\theta}{2}\sin\left(\frac{\phi-\psi}{2}\right) \quad , \quad q_3 = \cos\frac{\theta}{2}\sin\left(\frac{\phi+\psi}{2}\right) \tag{1.58}$$

satisfying that: $q_0^2 + q_1^2 + q_2^2 + q_3^2 = 1$. The rotation matrix, **A**, is then expressed as,

$$\mathbf{A} = \begin{pmatrix} q_0^2 + q_1^2 - q_2^2 - q_3^2 & 2(q_1q_2 - q_0q_3) & 2(q_1q_3 + q_0q_2) \\ 2(q_1q_2 + q_0q_3) & q_0^2 - q_1^2 + q_2^2 - q_3^2 & 2(q_2q_3 - q_0q_1) \\ 2(q_1q_3 - q_0q_2) & 2(q_2q_3 + q_0q_1) & q_0^2 - q_1^2 - q_2^2 + q_3^2 \end{pmatrix} \tag{1.59}$$

If the rigid body rotates around the CM, then its angular momentum, $\vec{L}$ is

$$\vec{L} = \sum_{i=1}^{N} m_i \vec{d_i} \times \vec{v_i} \tag{1.60}$$

where $\vec{d_i} = \vec{r_i} - \vec{R}_{\mathrm{CM},i}$. The components of $\vec{L}$ are related to the components of the angular velocity $\vec{\omega}$ by the elements of the moment of inertia matrix **I**,

$$\vec{L} = \mathbf{I} \cdot \vec{\omega} \tag{1.61}$$

whose elements, I_{jk}, are function of the vectors $\vec{d_i}$ as

$$I_{jk} = \sum_{i=1}^{N_a} m_i (\vec{d_i}^{\,2} \delta_{jk} - d_{i,j} d_{i,k}) \tag{1.62}$$

where δ_{jk} is the Kronecker delta, and $d_{i,j}$ is the jth component of $\vec{d}$ for particle i.

If a force $\vec{f_i}$ is acting at the position of atom i in the rigid molecule, then the resulting torque, $\vec{\tau}$ around the CM is

$$\tau = \frac{d\vec{L}}{dt} = \sum_{i=1}^{N_a} \vec{d_i} \times \vec{f_i} \tag{1.63}$$

All the last quantities are given in an external frame of reference, even if they are expressed relative to the CM of the rigid body. However, if the frame of reference is chosen such that the 3x3 moment of inertia matrix is diagonal, then, $\vec{L}$ is parallel to ω. That is, $\vec{L} = (I_{xx}\omega_x, I_{yy}\omega_y, I_{zz}\omega_z)$. This frame is called principal frame. The transformation from the principal frame to the external frame can be done through the quaternions. From now onwards, the subscript p indicates a quantity expressed in the principal frame.

Eq. 1.63 can be rewritten in the principal frame in terms of the diagonal elements of $\mathbf{I}$ to give the so-called Euler equations of motion for $\vec{\omega}_p$. However, an analogous equation can be obtained for the dynamics of the quaternions,[34]

$$\begin{pmatrix} \dot{q_0} \\ \dot{q_1} \\ \dot{q_2} \\ \dot{q_3} \end{pmatrix} = \frac{1}{2} \begin{pmatrix} q_0 & -q_1 & -q_2 & -q_3 \\ q_1 & q_0 & -q_3 & q_2 \\ q_2 & q_3 & q_0 & -q_1 \\ q_3 & -q_2 & q_1 & q_0 \end{pmatrix} \begin{pmatrix} 0 \\ \omega_{p,x} \\ \omega_{p,y} \\ \omega_{p,z} \end{pmatrix} = \mathbf{Q} \cdot \vec{\omega} \tag{1.64}$$

Notice that if the dynamics of the quaternions is known, then, we know the new orientation of every bond or vector in the rigid molecule by applying the rotation matrix $\mathbf{A}$. In this study, we have adopted the Fincham's algorithm as it implements the integration of the rotational motion for the leapfrog algorithm.[35] The desired quantities are $\vec{\omega}_p(t + \Delta t/2)$, and $\vec{q}(t + \Delta t)$. First, a set of auxiliary equations are derived to finally calculate these quantities. The auxiliary part of the algorithm begins with the calculation of the angular moment, $\vec{L}(t)$ in the external frame of reference,

$$\vec{L}(t) = \vec{L}(t - \Delta t/2) + \frac{\Delta t}{2}\vec{\tau}(t) \tag{1.65}$$

The angular momentum in the principal frame is obtained through

$$\vec{L}_p(t) = \mathbf{A}^{-1}\vec{L}(t) \tag{1.66}$$

and the angular velocity in the principal frame is obtained straightforward through the diagonal elements of $\mathbf{I}_p$

$$\omega_{p,i}(t) = \frac{L_{p,i}}{I_{ii}} \tag{1.67}$$

Quaternions at halftimestep are derived using eq 1.64,

$$\vec{q}(t+\Delta t/2) = \vec{q}(t) + \frac{\Delta t}{2}\mathbf{Q}(t)\cdot\vec{\omega}(t) \tag{1.68}$$

With $\vec{q}(t+\Delta t/2)$, we can now calculate $\mathbf{A}(t+\Delta t/2)$ using eq 1.59 and $\mathbf{Q}(t+\Delta t/2)$ as seen in eq 1.64. The main set of equations to derive $\vec{\omega}_p(t+\Delta t/2)$, and $\vec{q}(t+\Delta t)$ can now be stated. As for the auxiliary set of equations, the first quantity to be computed is $\vec{L}$ but at halftimestep,

$$\vec{L}(t+\Delta t/2) = \vec{L}(t-\Delta t/2) + \Delta t\vec{\tau}(t) \tag{1.69}$$

This quantity is transformed to the local frame using the value of $\mathbf{A}(t+\Delta t/2)$ computed from $\vec{q}(t+\Delta t/2)$,

$$\vec{L}_p(t+\Delta t/2) = \mathbf{A}^{-1}(t+\Delta t/2)\vec{L}(t+\Delta t/2) \tag{1.70}$$

The angular velocity is then obtained as in eq 1.67,

$$\omega_{p,i}(t+\Delta t/2) = \frac{L_{p,i}(t+\Delta t/2)}{I_{ii}} \tag{1.71}$$

With this quantity and the values for $\mathbf{Q}(t+\Delta t/2)$ calculated from eq 1.68, the new quaternions at $t+\Delta t$ are obtained from eq 1.64,

$$\vec{q}(t+\Delta t) = \vec{q}(t) + \Delta t\mathbf{Q}(t+\Delta t/2)\cdot\vec{\omega}(t+\Delta t/2) \tag{1.72}$$

1.3.3 Simulations in different ensembles

As most experiments are performed under conditions of constant temperature or pressure, in this section we present the used algorithms along this study to include such control in the equations of motion for our systems. First, the method used to simulate systems in the canonical ensemble (NVT) is presented, while in second term, we present the method to simulate the isobaric-isothermal ensemble (NPT).

1.3.3.1 NVT simulations

Thermostating a system in an MD simulation can be achieved by several approaches. The most simple method is the so-called simple velocity scaling method.[36] As seen from eq 1.30, the instantaneous temperature, $T(t)$, of a system of N particles is obtained from their velocities. Then, a simple way to thermostat such a system to a temperature T_0 is to rescale their velocities by a factor $\lambda = \sqrt{T_0/T(t)}$. Then, after a short period to reach equilibrium, this method maintains the kinetic energy of any particle strongly constant during the simulation. However, even in the canonical ensemble, there exist fluctuations in the kinetic energy per particle proportional to N^{-1}, hence, the scaling method does not generate a canonical ensemble. Other methods, as Andersen method introduce stochastic processes to reach the desired temperature T_0.[37] In this case, at some timesteps during the simulation, a particle is selected at random, and its velocity is replaced by a new velocity sampled from a Maxwell-Boltzmann velocity distribution. The frequency of the trial moves, ν, determines the degree of coupling with the bath. Andersen method generates a canonical ensemble, however, as in accepted trial moves velocities change their initial direction considerably, the obtained dynamics is strongly biased with respect to the real dynamics that a system in such conditions would follow. Hence, the dynamics of the system depends too much on the frequency ν, and the use of such a method is not recommended for the study of dynamical properties.

A third group of methods to keep the system at constant temperature are the *extended Lagrangian methods.* These kind of methods introduce artificial degrees of freedom in the Lagrangian of the system accounting for the bath. The most rigorous method to simulate the canonical ensemble is the Nosé-Hoover method, used along this study. Nosé modified the Lagrangian of an N particle system,[38] by considering explicitly the coupling of the system with a heat bath through a parameter s with an associated effective mass $Q > 0$.

$$\mathcal{L}_N = \sum_{i=1}^{N} \frac{m_i}{2} s^2 \dot{\vec{r}}^2 - U(\vec{r}^N) + \frac{Q}{2}\dot{s}^2 - \frac{g}{\beta}\ln s \tag{1.73}$$

From Lagrange equations, the Hamiltonian of the system is obtained,

$$H_N = \sum_{i=1}^{N} \frac{\vec{p}_i^2}{2m_i s^2} + U(\vec{r}^N) + \frac{p_s^2}{2Q} + \frac{g}{\beta}\ln s \tag{1.74}$$

where $\vec{p}_i$, and p_s account for the momenta of conjugate variables $\vec{r}_i$, and s. Nosé defined a new momenta p', and a scaled time t' as

$$p' = \frac{p}{s} \tag{1.75}$$

$$t' = \int_0^t \frac{dt}{s} \tag{1.76}$$

In that case, the associated equations of motion for $\vec{r} = \vec{r}', \vec{p}', s$, and p_s are,

$$\frac{d\vec{r_i}'}{dt'} = \frac{\vec{p_i}'}{m_i} \tag{1.77}$$

$$\frac{d\vec{p_i}'}{dt'} = F(r'^N) - \frac{s'p_s'}{Q}\vec{p_i}' \tag{1.78}$$

$$\frac{ds'}{dt'} = \frac{s'^2 p_s'}{Q} \tag{1.79}$$

$$\frac{dp_s'}{dt'} = \frac{1}{s}\left(\sum_{i=1}^{3N} \frac{\vec{p_i}^2}{m_i} - \frac{g}{\beta}\right) - \frac{sp_s^2}{Q} \tag{1.80}$$

Nosé equations are simple, time reversible and generate a canonical ensemble when $q = N_d$. However, from eq 1.76, the new time step fluctuates in a simulation and the sampling of a trajectory is performed at no constant time intervals. Hoover simplified these equations by defining a friction term ξ defined as[39]

$$\xi = \frac{s'p_s'}{Q} \tag{1.81}$$

If we now call the prime variables, real variables, we can drop the primes and consider them the real observables. With this change and introducing the ξ variable, the following set of Nosé-Hoover equations is obtained:

$$\frac{d\vec{r_i}}{dt} = \vec{v_i} \tag{1.82}$$

$$\frac{d\vec{v_i}}{dt} = \frac{F(\vec{r}^N)}{m_i} - \xi\vec{v_i} \tag{1.83}$$

$$\frac{d\xi}{dt} = \frac{N_d k_B}{Q}(T_i(t) - T_0) \tag{1.84}$$

Where we have replaced momenta $\vec{p_i}$ by velocities $\vec{v_i}$ ($\vec{p_i} = m_i\vec{v_i}$). The instantaneous temperature, $T(t) = \sum_{i=1}^{N} \frac{m_i \vec{v_i}^2(t)}{k_B N_d}$, have also been included in eq 1.84, and g has been replaced by N_d.

From eq 1.84, we can see the effect of Q on the tendency of the system to reach the bath temperature T_0. On the one hand, for large Q values, the coupling with the bath is very small and velocities are slightly changed at each timestep. Then, the obtained ensemble is closer to an NVE than to an NVT. On the other hand, when Q is small, the coupling with the bath is strong, and the time needed to reach T_0 is also very small. In simulations, however, it is more frequent to use the so-called relaxation time τ_{NH} to control the coupling with the bath. It can be written as a function of Q as follows,

$$\tau_{\mathrm{NH}}^2 = \frac{Q}{N_d k_B T_0} \tag{1.85}$$

Typical values for τ_{NH} range from . With all these considerations, the Hamiltonian of the system which is a conserved quantity during the simulation is given by,

$$\mathcal{H}_{\mathrm{NH}} = \sum_{i=1}^{N} \frac{m_i \vec{v}_i^{\,2}}{2} + U(\vec{r}^N) + \frac{\xi^2 Q}{2} + \frac{Q}{\tau_{\mathrm{NH}}^2} \int_0^t \xi(t')dt' \tag{1.86}$$

Once known the Nosé-Hoover equations of motion, we must implement them in the selected time integrator scheme for positions and velocities of the particles in the system. When adopting the leap-frog scheme, firstly, the friction term ξ is calculated at half timesteps from eq 1.84.

$$\xi(t+\Delta t/2) = \xi(t-\Delta t/2) + \Delta t \frac{N_d k_B}{Q}(T_i(t) - T_0) \tag{1.87}$$

Similarly to eq 1.45 for the velocity, we obtain $\xi(t)$,

$$\xi(t) = \frac{1}{2}[\xi(t-\Delta t/2) + \xi(t+\Delta t/2)] \tag{1.88}$$

Equation 1.44 for the velocities at half timesteps is modified to include the effect of the coupling with the bath as given in eq 1.83

$$\vec{v}(t+\Delta t/2) = \vec{v}(t-\Delta t/2) + \Delta t[\vec{a}(t) - \xi(t)\vec{v}(t)] \tag{1.89}$$

$$\vec{v}(t) = \frac{1}{2}[\vec{v}(t-\Delta t/2) + \vec{v}(t+\Delta t/2)] \tag{1.90}$$

Finally, the new positions are calculated as in eq 1.43

$$\vec{r}(t+\Delta t) = \vec{r}(t) + \Delta t \vec{v}(t+\Delta t/2) \tag{1.91}$$

Notice that in this set of equations, the value of $\vec{v}(t)$ is required both to compute the instantaneous temperature $T_i(t)$ in eq 1.87, and to compute $\vec{v}(t)$ from eqs 1.87-1.89. To solve this problem, an iteration of eqs 1.87-1.90 is performed to obtain self consistency. First, through the standard Verlet algorithm, one obtains, $\vec{r}(t), \vec{v}(t), T(t)$, and $\vec{a}(t)$, then, the iteration process begins. In that case, the process is stopped after 4 iterations.

1.3.3.2 NPT simulations

To perform NPT MD simulations, the volume of the simulation box changes with time in order to make the internal pressure of the system, P_{int}, equal to a desired reference pressure P_0. This is analogous to having a piston coupled with our system which changes its volume at a given rate. Such an effect was included by Andersen in an extended Lagrangian method.[37] Firstly, the coordinates $\vec{r_i}$ are scaled by a factor $V^{1/3}$ as follows,

$$\vec{\rho_i} = \frac{\vec{r_i}}{V^{1/3}} \tag{1.92}$$

Andersen included the volume as a new degree of freedom in the Lagrangian of an N particle system,

$$\mathcal{L}_A = \sum_{i=1}^{N} \frac{V^{2/3} m_i \vec{\rho_i}^2}{2} - U(V^{1/3}\vec{\rho}^N) + \frac{M}{2}V'^2 - P_0 V \tag{1.93}$$

where M accounts for the mass of a piston changing the volume V of the simulation box. The term $P_0 V$ is a potential derived from the external pressure P_0 acting on the piston. Notice that the piston does not only act on a side of the simulation box, but it isotropically decreases or increases the volume of the system. From eq 1.93, the Hamiltonian of the system (not shown here) can be derived, and then the equations of motion for the unscaled coordinates and velocities $\vec{r_i}$, and $\vec{v_i}$ can be easily obtained from eqs 1.13. If we define a new variable $\chi(t)$ as,

$$\chi(t) = \frac{1}{3}\frac{d \ln V(t)}{dt} \tag{1.94}$$

the resulting equation of motion are,

$$\frac{d\vec{r_i}}{dt} = \vec{v_i} + \chi \vec{r_i} \tag{1.95}$$

$$\frac{d\vec{v_i}}{dt} = \frac{F(\vec{r}^N)}{m_i} - \chi\vec{v_i} \tag{1.96}$$

$$M\frac{d^2V}{dt^2} = -P_0 + \frac{1}{3V}(\sum_{i=1}^{N} m_i\vec{v_i}^2 + \sum_{i>j}\vec{r_{ij}}\vec{F_{ij}}) \tag{1.97}$$

The equation accounting for the variation of V is given by eq 1.94. See that eq 1.97 is the Newton's third law for V. Here, the first term in the right gives minus the external pressure acting on the piston, while the positive term accounts for the internal pressure exerted by the fluid. As a consequence, when an imbalance exists between these two terms, the volume of the box fluctuates and only it remains constant when the difference of both terms equals zero. Using the Melchionna modification of the Hoover algorithm, the equations of motion of Andersen can be coupled to a Nosé-Hoover thermostat,[40]

$$\frac{d\vec{r_i}}{dt} = \vec{v_i} + \chi(\vec{r_i} - \vec{R}_{\mathrm{CM}}) \tag{1.98}$$

$$\frac{d\vec{v_i}}{dt} = \frac{F(\vec{r}^N)}{m_i} - (\xi + \chi)\vec{v_i} \tag{1.99}$$

$$\frac{d\xi}{dt} = \frac{N_d k_B}{Q}(T(t) - T_0) + \frac{1}{Q}(M\chi^2 - k_B T_0) \tag{1.100}$$

$$\frac{d\chi}{dt} = \frac{3}{M}V(P(t) - P_0) - \xi\chi \tag{1.101}$$

where $\vec{R}_{\mathrm{cm}}$ is the center of mass of the system in the simulation box. Analogously to the Nosé-Hoover thermostat case, the effective mass M is related to a relaxation time τ_P controlling the pressure fluctuations,

$$\tau_P^2 = \frac{M}{N_d k_B T_0} \tag{1.102}$$

In MD simulations, τ_P is usually chosen an order of magnitude larger than τ_{NH}. If not only box size variation is desired but also shape variation, then, the last set of equations has to be modified. However, the anisotropic version of Lagrangian 1.93 is mainly used when crystal structures are taken into account, as this is not the case for our simulations, we use the isotropic version.

Once derived the equations of motion, they can be implemented easily. First, the terms ξ and χ are calculated at half timesteps to then, be computed at time t,

$$\xi(t+\Delta t/2) = \xi(t-\Delta t/2) + \frac{\Delta t N_d k_B}{Q}(T(t)-T_0) + \frac{\Delta t}{Q}(M\chi(t) - k_B T_0) \tag{1.103}$$

$$\xi(t) = \frac{1}{2}[\xi(t+\Delta t/2) + \xi(t-\Delta t/2)] \tag{1.104}$$

$$\chi(t+\Delta t/2) = \chi(t-\Delta t/2) + \Delta t[\frac{3V(t)}{W}(P(t)-P_0) - \chi(t)\xi(t)] \tag{1.105}$$

$$\chi(t) = \frac{1}{2}[\chi(t+\Delta t/2) + \chi(t-\Delta t/2)] \tag{1.106}$$

Secondly, the leap-frog scheme is followed for velocities and positions,

$$\vec{v}(t+\Delta t/2) = \vec{v}(t-\Delta t/2) + \Delta t[\vec{a}(t) - (\xi(t)+\chi(t))\vec{v}(t)] \tag{1.107}$$

$$\vec{v}(t) = \frac{1}{2}[\vec{v}(t+\Delta t/2) + \vec{v}(t-\Delta t/2)] \tag{1.108}$$

$$\vec{r}(t+\Delta t) = \vec{r}(t) + \Delta t[\vec{v}(t+\Delta t/2) + \chi(t+\Delta t/2)(\vec{r}(t+\Delta t/2) - \vec{R}_{\mathrm{CM}})] \tag{1.109}$$

$$\vec{r}(t+\Delta t) = \frac{1}{2}[\vec{r}(t) + \vec{r}(t+\Delta t)] \tag{1.110}$$

As for the Nosé-Hoover thermostat, this set of equations has to be solved iteratively to obtain estimates for $T(t), P(t), \vec{v}(t)$, and also for $\vec{r}(t+\Delta t/2)$ which is used in eq 1.109. The initial values are obtained through a normal leap-frog integration and then iterated 5 times to obtain self consistency. Finally, the equation for the volume of the simulation box is obtained from eq 1.94,

$$V(t+\Delta t) = V(t)\exp[3\chi(t+\Delta t/2)] \tag{1.111}$$

Simulations at NPT conditions are also very useful if one is interested in simulate a system in the NVT ensemble. In that case, the initial box size is determined from the equilibrium average volume obtained from a long NPT simulation of the same system at the same temperature and number of particles. In this study, we have used the NPT method described above for this purpose.

1.3.4 Force field

The description of the interaction between atoms and molecules is probably the most important step in MD simulations. In this case, forces are derived from potentials and, hence, structure and dynamics for a given system are highly dependent on their chosen form. Classical MD simulations, however, are based on the integration of the Newton's or Lagrange's equations of motion for each atom in the system, being the electronic degrees of freedom not treated explicitly. Other MD simulation techniques, called ab initio methods, consider electronic variables as active degrees of freedom. Nevertheless, even if electronic degrees of freedom are not considered explicitly in a particular MD simulation, they have an important paper in the interactions between atoms. Then, there is a need to do some approximation in order to include them, at least, in an approximate way. Such a way, is to split the Schrodinger equation describing the behavior of nuclei and the electrons into two coupled equations, one for the nuclei and the other for the electronic degrees of freedom. For classical MD simulations, a further approximation is done, and nuclei move according to classical equations of motion being the forces acting on each atom derived from an effective potential surface called force field. The functional form of such potentials comes from quantum mechanical computational methods, or from fits to experimental results.

In this section, we present first, the main approximations needed to include the electronic degrees of freedom in the effective potential surface,[4] and then, we describe the different contributions in the resulting force field from intramolecular, and intermolecular interactions.

1.3.4.1 Derivation

Let's have a system with N nuclei and k electrons. The associated Hamiltonian operator, H, is given by,

$$\begin{aligned} H &= \underbrace{-\frac{\hbar}{2}\sum_{i=1}^{N}\frac{1}{M_i}\nabla^2_{\vec{R}_i}}_{K_n} \underbrace{-\frac{\hbar}{2m_e}\sum_{i=1}^{k}\nabla^2_{\vec{r}_i}}_{K_e} + \underbrace{\frac{e^2}{4\pi\epsilon_0}\sum_{i=1}^{k}\sum_{j=1}^{N}\frac{Z_j}{|\vec{r_i}-\vec{R_k}|}}_{U_{en}} + \\ &+ \underbrace{\frac{e^2}{4\pi\epsilon_0}\sum_{i<j}^{k}\frac{1}{|\vec{r_i}-\vec{r_j}|}}_{U_{ee}} + \underbrace{\frac{e^2}{4\pi\epsilon_0}\sum_{i<j}^{N}\frac{Z_iZ_j}{|\vec{R_i}-\vec{R_j}|}}_{U_{nn}} \end{aligned} \tag{1.112}$$

where e and m_e stand for the charge and the mass of an electron, respectively, Z is the atomic number, M_i is the mass of a nuclei i, and $\hbar$ is the reduced Planck Constant $\hbar = h/2\pi$. Notice that the positions and masses for nuclei, are given in capital letters to differentiate from electron positions and masses. Different contributions to the Hamiltonian operator from electrons and nuclei have been indicated below eq 1.112 with subscript e for the electrons, and n for the nuclei. In this sense, the Hamiltonian can be decomposed into the operator for the kinetic energy of the nuclei, K_n, and a Hamiltonian operator H_e accounting for the kinetic energy of the electrons and the potential energies, $H_e = K_e + U_{en} + U_{ee} + U_{nn}$.

From quantum mechanics, the state of such a system is characterized by the wave function ψ being the solution of the Schrödinger equation,

$$i\hbar\frac{\partial\psi(\vec{R},\vec{r},t)}{\partial t} = H\psi(\vec{R},\vec{r},t) \tag{1.113}$$

As we are interested in performing classical MD simulations, a first step is to separate ψ into a product of a normalized nuclear wave function $\chi(\vec{R},t)$, and a normalized electronic wave function $\phi(\vec{r},t)$,

$$\psi(\vec{R},\vec{r},t) \approx \chi(\vec{R},t)\phi(\vec{r},t)\exp\left[\frac{i}{\hbar}\int_{t_0}^{t} E_e(t')dt'\right] \tag{1.114}$$

where the phase factor E_e is given by $E_e = \int d\vec{r}d\vec{R}\phi^*(\vec{r},t)\chi^*(\vec{R},t)H_e\phi(\vec{r},t)\chi(\vec{R},t)$.

Inserting eq 1.113 into eq 1.114, and doing some extra calculations,[4] separated Schrödinger equations are obtained for χ, and ϕ. However, it is not our objective to show all the steps needed to derive classical equations of motion from the Schrödinger as they can be found in the literature, we just want to present those more important. If nuclei are, then, approximated as classical point particles, one obtains Newton's equations of motion for the positions of the nuclei,

$$M_i\frac{d^2\vec{R}_i(t)}{dt} = -\nabla_{\vec{R}_i}\int\phi^* H_e\phi d\vec{r} = -\nabla_{\vec{R}_i}U_e^E(\vec{R}(t)) \tag{1.115}$$

This equation means that nuclei move according to classical mechanics in an effective potential U_e^E due to the electrons but which is only function of nuclei coordinates and time. For the electrons, we have a time-dependent wave equation,

$$i\hbar\frac{\partial\phi(\vec{R},\vec{r},t)}{\partial t} = H_e\phi(\vec{R},\vec{r},t) \tag{1.116}$$

Then, nuclei move like classical particles, while electrons move in a self-consistent way, being treated as quantum objects. Approaches derived from such a couple of equations are often called Ehrenfest molecular dynamics. These equations, however, involve electronic excited sates, and transition between these states are allowed. An approximation comes from expanding ϕ in a basis ϕ_j of electronic states such that,

$$\phi(\vec{R},\vec{r},t) = \sum_{j=0}^{\infty} c_j(t)\phi_j(\vec{r},\vec{R}) \tag{1.117}$$

where $c_j(t)$ are complex coefficients. In this case, if the difference in energy between the ground state ϕ_0 and the first excited state is larger than k_BT for a given system, electronic transitions will be unlikely, and the total electronic wave function ϕ can be restricted only to its ground state ϕ_0. The nuclei, then, move according to eq 1.115 under a potential energy surface given by,

$$U_e^E(\vec{R}) = \int \phi_0^*(\vec{R},\vec{r})H_e(\vec{R},\vec{r})\phi_0(\vec{R},\vec{r})d\vec{r} \tag{1.118}$$

whose value is obtained from the time-independent electronic Schrödinger equation,

$$H_e(\vec{R},\vec{r})\phi_0(\vec{R},\vec{r}) = U_e^E(\vec{R})\phi_0(\vec{R},\vec{r}) \tag{1.119}$$

In ab initio molecular dynamics methods, electronic Schrödinger equation is solved approximately to determine the effective potential energy of the nuclei. Then, forces acting on the nuclei are derived straightforwardly. In classical molecular dynamics, however, U_e^E is approximated by a truncated expansion of many-body contributions, named $U(\vec{R})$, being the electronic degrees of freedom replaced by interaction potentials $\{U_n\}$. The potential energy surface, or force field, used in a simulation, then, has the following functional form,

$$U(\vec{R}) = \sum_{i=1}^{k} U_1(\vec{R}_i) + \sum_{i<j}^{k} U_2(\vec{R}_i,\vec{R}_j) + \sum_{i<j<l}^{k} U_3(\vec{R}_i,\vec{R}_j,\vec{R}_l) + \ldots\ldots \tag{1.120}$$

Interactions in a classical MD simulation, can be divided on intramolecular, or bonded interactions, involving atoms belonging to a same molecule, and intermolecular interactions, or non bonded interactions, between unlike atoms belonging to different molecules. Although for intramolecular interactions there can exist three- and four-body terms, the main part of intra and inter molecular interactions are modelled as two-body potential functions depending on the distance between atoms. As said in the beginning of this section, the parameters describing each kind of interaction are obtained either from quantum mechanics calculations, or from fits to experimental results. With these considerations the computational cost needed to compute forces acting on atoms is reduced considerably. In the following subsections we describe used functional forms for intramolecular and intermolecular interactions along this thesis.

1.3.4.2 Intramolecular interactions

Typically, intramolecular potentials contain different terms accounting for:

- **Stretching**

  The distance between two atoms covalently bonded, generally, varies. Although there exist an optimal distance, in terms of energy, called equilibrium bond length r_0, the interaction of the atoms with other atoms, makes the distance to vary and if the energy is high enough, the bond can break. The most used classical potential to model this stretch between sites i and j belonging to the same molecule is a harmonic potential,

  $$U_{\mathrm{stretch}}(r_{ij}) = \frac{1}{2}K_{ij}(r_{ij} - r_0)^2 \tag{1.121}$$

  where K_{ij} is the force constant for the bond between atoms i and j. See that this potential does not account for bond breaking. Other potentials as the Morse potentials account for this fact.[41] However, if the displacements occur only around r_0, then, the harmonic potential is a good choice.

- **Bending**

  If we have a chain-like molecule consisting on three atoms i, j, and k, then, the molecule can be characterized by the so-called valence angle θ_{ijk}. This angle varies around the equilibrium angle θ_0 for which the energy is minimal. Bending is modelled also with a harmonic potential,

  $$U(\theta_{ijk}) = \frac{1}{2}K_b(\theta_{ijk} - \theta_0)^2 \tag{1.122}$$

  where K_b is the bending force constant for the angle θ_{ijk}.

- **Torsion**

  For molecules with four atoms i, j, k, and l, the dihedral angle ϕ_{ijkl} between the plane formed by $i - j - k$ and the plane defined by $j - k - l$ can not

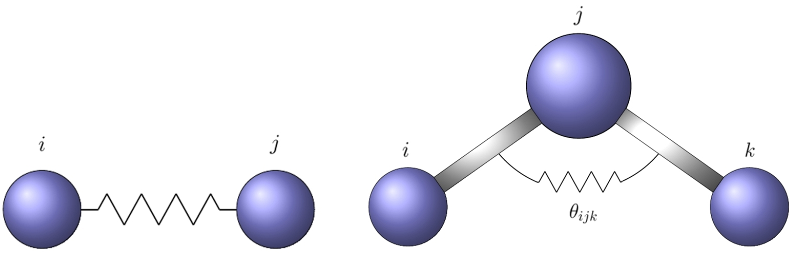

Figure 1.3: Modeling of stretching (left) and bending (right) through harmonic potentials.

coincide (see Figure 1.4a). In fact, torsion is more likely to occur in a molecule than stretching or bending due to the high amount of energy associated to these last structural changes. Torsion can be modelled with a harmonic potential, however, a more adopted form for the contribution to the energy due to torsion is a cosine potential,

$$U_{\mathrm{tors}}(\phi_{ijkl}) = A[1 + \cos(m\phi_{ijkl} - \delta)] \tag{1.123}$$

where A is a torsional force constant, m deals for the periodicity of the cosine function, and δ is an angle. An example of molecule where this functional form U_{tors} works is the ethane molecule.

- **Improper torsion**

  When having a particular geometry in a molecule of three atoms i, j, and k around a third atom l, the dihedral angle ϕ_{ijkl} between the plane formed by $i - l - j$ and the vector $\vec{r}_{lk}$ can change (see Figure 1.4b). This improper torsion occurs in simulations when dealing with stretching, bending and torsion intramolecular potentials. However, we may be interested in maintaining planarity for a given set of atoms or to choose a given chirality for a molecule to match its experimentally observed structure. The force restraining the atoms to a particular geometry is derived from the improper torsion potential U_{tors} given by

$$U_{\mathrm{impr}}(\phi_{ijkl}) = \frac{K}{2}(\phi_{ijkl} - \phi_0)^2 \tag{1.124}$$

  where K_{impr} is the associated force constant, and ϕ_0 is the angle where the potential passes through its minimum.

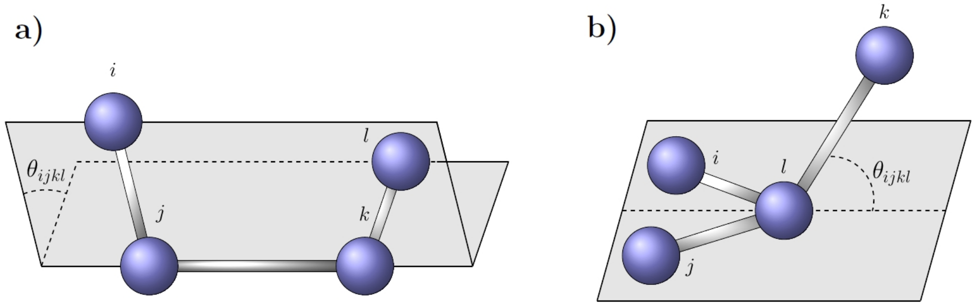

Figure 1.4: Scheme of a torsion around a molecular axis (a) and improper torsion (b).

Other terms can be added to the intramolecular force field as for example coupling between the different degrees of freedom, for example, stretching-bending, torsion-bending, ...

1.3.4.3 Intermolecular interactions

The most important contribution to forces between molecules can be explained from electrostatic interactions between its consituents. Intermolecular forces are divided into short-ranged or long-ranged. As these forces are usually modelled as a power law, $u(r) \propto r^{-\alpha}$, their range is strictly related to the exponent α. Then, an interaction is considered short-ranged if $\alpha > 3$, and long-ranged if $\alpha \leq 3$. Long-ranged interactions involve ionic interactions (Coulombic) which decay as $u(r) \propto r^{-1}$, ion-dipole interactions with $u(r) \propto r^{-2}$, and even fixed dipole/dipole interactions which lead to $u(r) \propto r^{-3}$. Short-ranged interactions involve, for example, dipole/ induced dipole interactions which decay as $u(r) \propto r^{-6}$.

As short and long ranged interactions are not treated, computationally, in the same manner, we may introduce the adopted potential functions and methodologies to compute them by separate.

1.3.4.3.1 Short-ranged forces

For a pair of atoms or molecules, even if their both net charges sum zero, there exist attractive forces so-called Van der Waals forces or dispersion forces, and also repulsive forces. On the one hand, for intermediate distances between such atoms, the redistribution of their charge densities, involves the creation of fluctuating instantaneous dipoles which make the interaction attractive. In that case, the interaction energy between two dipoles which can orient freely is $u(r) \propto r^{-6}$, which is short-ranged.[6] On the other hand, for small distances, the overlap between the wavefunctions provokes a repulsion proportional to $\exp(-r)$ as known from Pauli's exclusion principle. Nevertheless, if the repulsion part of the potential is chosen proportional to r^{-12}, then, the computational demand to calculate such an interaction is reduced as it can be computed from the square of r^{-6}. These attractive and repulsive interactions can be modelled in the form of a short-ranged potential. Although there exist several formulations for such a potential, the most used model is the Lennard Jones (LJ) potential defined as,

$$U_{\mathrm{LJ}}(r_{ij}) = 4\epsilon_{ij}\left(\frac{\sigma_{ij}^{12}}{r_{ij}^{12}} - \frac{\sigma_{ij}^{6}}{r_{ij}^{6}}\right) \tag{1.125}$$

where r_{ij} is the distance between atoms i and j, ϵ is the depth of the well, and σ corresponds to the distance at which the interatomic potential is zero. The position of the minimum r_m is related to σ by $r_m = 2^{1/6}\sigma$. These parameters can be obtained experimentally from fits to pure substances, and, then, be used as a reference for simulations.[42] See that LJ potential differs from square well potentials as particles which high energies can penetrate the hard core of other atoms. For mixtures containing different kind of molecules, crossed LJ terms, σ_{ab} and ϵ_{ab}, between unlike atoms a, and b, belonging to different molecules, or to distant sites of a same molecule, are calculated from Lorentz-Berthelot (LB) combining rules. Lorentz rule assumes an arithmetic mean for σ_{ab}, while Berthelot rule assumes a geometric mean for ϵ_{ab},

$$\sigma_{ab} = \frac{\sigma_{aa} + \sigma_{bb}}{2} \tag{1.126}$$

$$\epsilon_{ab} = \sqrt{\epsilon_{aa}\epsilon_{bb}} \tag{1.127}$$

Other more sophisticated combining rules have also been derived to compute unlike-pair interactions. This is the case of the Kong[43] or the Waldman and Hagler rules[44] which, for example, give better results than the LB rules for simulations of binary mixtures of rare gases.[45] However, for simulations of the kind of systems studied along this thesis, and also for similar ones where the progress made is restricted to the last decade, the LB rules have been widely used in the literature. Then, their adoptance, is preferable, in front of other combining rules where no simulation results are available to infer whether a combining rule is better than the other. Hence, in the present study, we have used the LB combining rules.

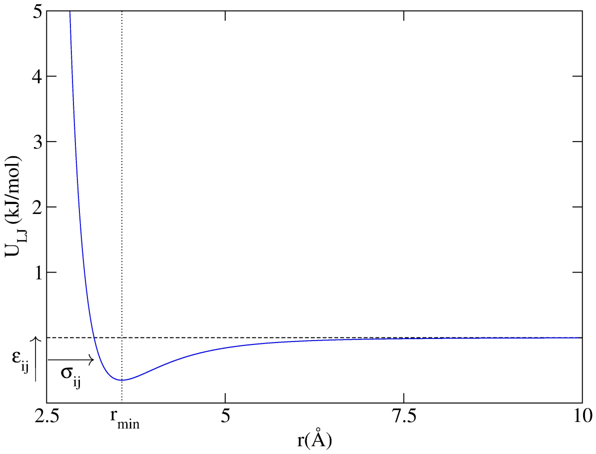

Figure 1.5: Lennard-Jones potential, $U_{\rm LJ}(r)$ with $\epsilon_{ij} = 0.65$ kJ/mol, and $\sigma_{ij} = 3.166$ Å.

In MD simulations, the LJ potential is truncated at $r = r_c$, and then, we need to correct the total potential energy to account for the contribution of those pairs of atoms separated by a distance larger than r_c. If we consider two kind of atoms a and b, the contribution to the total potential energy due to the tail of the LJ potential, $U_{\rm LJ}^{\rm tail}$, is calculated through the following equation,

$$U_{\rm LJ}^{\rm tail} = \frac{N_a N_b}{2V} \int_{r_c}^{\infty} 4\pi r^2 g_{ab}(r) U_{LJ}(r) dr \tag{1.128}$$

where N_a and N_b are the number of atoms of type a and b respectively. For $r > r_c$ we assume that $g_{ab}(r) = 1$. Solving the integral, we obtain the numerical expression for eq 1.128,

$$U_{\mathrm{LJ}}^{\mathrm{tail}} = \frac{8\pi N_a N_b}{V} \sum_{i=1}^{N_a} \sum_{j=1}^{N_b} \frac{\epsilon_{ij}\sigma_{ij}^6}{3} \left(\frac{\sigma_{ij}^6}{3r_c^6 - 1} \right) \tag{1.129}$$

The pressure also depends on the potential energy through the second term in eq 1.34. Then, it also needs to be corrected for the same reason than the total potential energy. In this case, the LJ tail contribution to the pressure, P^{tail}, is given by,

$$P^{\mathrm{tail}} = -\frac{1}{2}\frac{N_a N_b}{3V} \int_{r_c}^{\infty} 4\pi r^3 \frac{\partial U_{\mathrm{LJ}}(r)}{\partial r} dr \tag{1.130}$$

which results in the following numerical equation once the integral is solved

$$P^{\mathrm{tail}} = \frac{16\pi N_a N_b}{V} \sum_{i=1}^{N_a} \sum_{j=1}^{N_b} \frac{\epsilon_{ij}\sigma_{ij}^6}{3r_c^3} \left(1 - \frac{2}{3}\frac{\sigma_{ij}^6}{r_c^6} \right) \tag{1.131}$$

1.3.4.3.2 Long-ranged forces

Let's have a system consisting on a set of N ions with charges $q_1, q_2, \ldots, q_N$ at positions $\vec{r}_1, \vec{r}_2, \ldots, \vec{r}_N$, in a volume $V = L^3$. As we are interested in performing an MD simulation, periodic boundary conditions are applied. Then, the electrostatic contribution, U_{el}, to the total energy of the system, is given by the interaction of the particles inside the simulation box with the others, as well as, with its images in replica cells,

$$U_{\mathrm{el}} = \frac{1}{2} \sum_{i=1}^{N} q_i \phi(r_i) \tag{1.132}$$

where $\phi(r_i)$ is the electrostatic potential at position r_i:

$$\phi(r_i) = \sum_{\vec{n}}{}' \sum_{j=1}^{N} \frac{q_j}{|\vec{r}_{ij} + \vec{n}L|} \tag{1.133}$$

The prime means that when $\vec{n} = (0,0,0)$, the sum over j does not include the $i = j$ case, otherwise, the ion would interact with itself. This sum is only conditionally convergent, which means that it depends on the order in which the sum is performed. Then, eq 1.132 is not useful to compute the electrostatic energy for a system with periodic boundary conditions. A widely used method to overcome this problem is the Ewald method, also known as Ewald summation method.[46]

In the Ewald method, we assume that every ion at position $\vec{r}_i$ is surrounded by a gaussian charge distribution with a total charge $-q_i$ cancelling the charge q_i of the ion. This set of charge distributions are called *screening* charges, as for sufficiently long distances, they screen the electrostatic potential due to point charge i. To compensate the effect of the included screening charges, a set of compensating gaussian charge distributions, with a total charge equal to that of each ion i, are placed at $\vec{r}_i$ (see Figure 1.6). The parameter $1/(\sqrt{2}\alpha)$ controls the width of the gaussian distributions whose expression is given by,

$$\rho_{\text{Gauss}} = \pm q_i \left(\frac{\alpha^2}{\pi}\right)^{\frac{3}{2}} \exp(-\alpha^2 r^2) \tag{1.134}$$

The idea of Ewald method is, then, to split eq 1.132 into two different contributions; first, a real space sum accounting for the electrostatic energy due to the point charges, and to its screening charge distributions, and secondly, a Fourier space sum accounting for the effect of the compensating charge distributions. Obviously self interactions are excluded in the calculations. The power of Ewald method is that it replaces the infinite sum given by eqs 1.132 and 1.133 by converging real space, and Fourier space sums. In this section, we are not interested in deriving the final expressions step by step as the procedure is available in the literature,[2] however, we give below the main ideas to compute the respective contributions.

First of all, we begin with the calculation of the contribution to the electrostatic potential at a position r arising from the set of compensating charge distributions. As these distributions are located at the ion positions and at its replica images, the resulting gaussian distribution is given by

$$\rho_c(r) = \sum_{j=1}^{N} \sum_{\vec{n}} q_j \left(\frac{\alpha^2}{\pi}\right)^{\frac{3}{2}} \exp[-\alpha^2 |\vec{r} - (\vec{r}_j + \vec{n}L)|^2] \tag{1.135}$$

The electrostatic potential at a point r due to this charge distribution is computed by solving Poisson equation, which in SI units is given by:

$$-\nabla^2 \phi_c(r) = \frac{\rho_c(r)}{\epsilon_0} \tag{1.136}$$

This equation can be rewritten in the Fourier space (reciprocal space) giving,

$$k^2\phi_c(k) = \frac{\phi_c(k)}{\epsilon_0} \tag{1.137}$$

where k is the modulus of the reciprocal lattice vector $\vec{k}$, which, for a cubic cell has the components $\vec{k} = (2\pi/L)(l_1, l_2, l_3)$, with l_1, l_2, and l_3 integers.

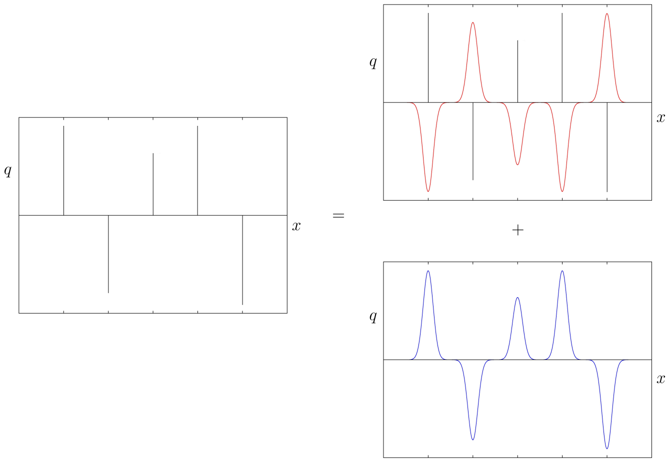

Figure 1.6: The sum for point charges (left) in eq 1.133 is splitted into two sums; a real space sum including the effect of the point and the screening charges (right top), and a second sum in the Fourier space accounting for the compensating charges (right bottom).

Solving the Poisson equation, the obtained electrostatic potential $\phi_c(r)$ is

$$\phi_c(r) = \frac{1}{\epsilon_0 V}\sum_{\vec{k}\neq 0}\sum_{j=1}^{N}\frac{q_j}{k^2}\exp[-i\vec{k}(\vec{r}-\vec{r}_j)]\exp(-k^2/4\alpha^2) \tag{1.138}$$

The contribution to the electrostatic energy, U_c, at r_i is,

$$U_c = \frac{1}{2}\sum_{i}^{N} q_i\phi_c(r_i) = \frac{1}{2\epsilon_0 V}\sum_{\vec{k}\neq 0}\sum_{i,j=1}^{N}\frac{q_i q_j}{k^2}\exp[-i\vec{k}(\vec{r}_i-\vec{r}_j)]\exp(-k^2/4\alpha^2) \tag{1.139}$$

However, as we have included the effect of the compensating charge at r_i with the point charge i, we must correct for this self-interaction, and subtract it from eq 1.139. If we compute the electrostatic potential $\phi_s(r)$ due to a distribution charge of the form given in eq 1.134, it yields

$$\phi_s(r) = \frac{1}{4\pi\epsilon_0}\frac{q_i}{r}\mathrm{erf}(\alpha r) \tag{1.140}$$

where $\mathrm{erf}(r)$ is the error function. Hence, at $r = 0$, which accounts for the center of the gaussian compensating charge, the contribution to the electrostatic energy due to ϕ_s is

$$U_s = \frac{1}{2}\sum_{i=1}^{N} q_i\phi_s(0) = \frac{1}{4\pi\epsilon_0}\frac{\alpha}{\sqrt{\pi}}\sum_{i=1}^{N} q_i^2 \tag{1.141}$$

Finally, we must account for the electrostatic energy due to the point charges, and the screening gaussian distributions. It can be demonstrated that the, for an ion i, the electrostatic potential, $\phi_p(r)$, due to its point charge q_i and the screening distribution is

$$\phi_p(r) = \frac{1}{4\pi\epsilon_0}\frac{q_i}{r}\mathrm{erfc}(\alpha r) \tag{1.142}$$

where $\mathrm{erfc}(x) = 1 - \mathrm{erf}(x)$. The corresponding contribution, U_p to the electrostatic energy due to ϕ_p is

$$U_p = \frac{1}{8\pi\epsilon_0}\sum_{i\neq j}^{N} q_i q_j \frac{\mathrm{erfc}(\alpha r_{ij})}{r_{ij}} \tag{1.143}$$

Note that this expression should have included a summation over all periodic images of the point charges and their screening charge distributions. However, we assume the minimum image convention, which restricts the sum to the simulation box and nearest neighbors. With all the contributions calculated, the total electrostatic energy of our system, U_{elec}, is the sum of U_c, and U_p subtracting the self interaction term, U_s,

$$\begin{aligned} U_{\mathrm{elec}} &= U_c + U_p - U_s = \\ &= \frac{1}{2\epsilon_0 V}\sum_{\vec{k}\neq 0}\sum_{i,j=1}^{N}\frac{q_i q_j}{k^2}\exp[-i\vec{k}(\vec{r}_i - \vec{r}_j)]\exp(-k^2/4\alpha^2) \\ &+ \frac{1}{8\pi\epsilon_0}\sum_{i\neq j}^{N} q_i q_j\frac{\mathrm{erfc}(\alpha r_{ij})}{r_{ij}} - \frac{1}{4\pi\epsilon_0}\frac{\alpha}{\sqrt{\pi}}\sum_{i=1}^{N} q_i^2 \end{aligned} \tag{1.144}$$

Equation 1.144 has been obtained for a system of N ions, however, in a MD simulation, we deal not only with point charges but with molecules. In this case, we have also to exclude non desired intramolecular interactions which, if using eq 1.144 directly, we would take into account. In that case, firstly, the term U_p has to be corrected, and the sum in eq 1.143 has to be restricted to $N - M$ interactions, where M is the number of non-desired intramolecular interactions. Secondly, the term U_c, as written in eq 1.139, considers the interaction of compensating charges of atoms in a given molecule with the other atoms of the same molecule. The self interaction of an atom with its compensating charge in the main cell was corrected with U_s, however, we have to correct for the interaction of compensating charges of the atoms different that a given one, but that are in the same molecule. As we know the electrostatic potential due to a compensating charge at a given distance r (see eq 1.140), we can include this effect in equation 1.144. With these considerations, the final expression for the total electrostatic energy, U_{elec} of our system yields

$$\begin{aligned} U_{\text{elec}} &= \frac{1}{2\epsilon_0 V} \sum_{\vec{k}\neq 0} \sum_{i,j=1}^{N} \frac{q_i q_j}{k^2} \exp[-i\vec{k}(\vec{r_i} - \vec{r_j})] \exp(-k^2/4\alpha^2) \\ &+ \frac{1}{8\pi\epsilon_0} \sum_{m\neq j}^{N-M} q_m q_j \frac{\text{erfc}(\alpha r_{mj})}{r_{mj}} \\ &- \frac{1}{4\pi\epsilon_0} \frac{\alpha}{\sqrt{\pi}} \sum_{i=1}^{N} q_i^2 - \frac{1}{4\pi\epsilon_0} \sum_{\text{molecules}} \sum_{l<m}^{N^*} \frac{q_l q_m}{r_{lm}} \text{erf}(\alpha r_{lm}) \end{aligned} \quad (1.145)$$

where N^* is the number of excluded interactions in a molecule. See that for the first term in eq 1.145, we have to restrict the sum to a set of lattice vectors $\vec{k}$, such that $\vec{k}_x \in [-k_x^{\max}, k_x^{\max}]$, $\vec{k}_y \in [-k_y^{\max}, k_y^{\max}]$, and $\vec{k}_z \in [-k_z^{\max}, k_z^{\max}]$. In an MD simulation, the parameters controlling the convergence of the Ewald sum, are: the parameter α giving the width of the the screening and compensating charge distributions, the lower and upper bounds for the components of the lattice vector $\vec{k}$, and the cut-off r_{cut} selected for our simulation. The choice of these parameters depend on the size of the system. Even for large systems, a choice of $|\pm k_{x,y,z}^{\max}| = 5$ is sufficient for a good convergence of the sum Fourier space sum in eq 1.145. For the α parameter, on the one hand, an small value makes the sum in the second term of eq 1.145 to converge rapidly, on the other hand, a large value for α makes the Fourier space sum to converge fast. Then, the optimal choice for α is that which minimizes the time needed to compute the real space and Fourier space sums in the equation for U_{elec}.[47] For our simulations, for example, a typical value for α is 0.210 Å^{-1}.

1.3.4.4 All atom vs united-atom

When we want to simulate a system with polyatomic molecules, different approaches can be adopted to represent the LJ force centers. On the one hand, a force center can be assigned to all atoms. The corresponding models are called *All Atom* (AA) models.[48] These potentials give a good account of molecular geometry and structure. However, for large systems, they involve long computer times due to the large number of force centers considered. On the other hand, different atoms of a given molecule can be treated as a unique force center. This approach results in the so-called *United Atom* (UA) models, widely used for the modeling of hydrocarbons. Here, the influence of hydrogen atoms is considered through the parametrization of the potential parameters, being the force center placed in the carbon atom or the corresponding major atom.[49–51] In this study, all the performed simulations involve a number of water molecules which ranges from a few hundreds to thousands of molecules. As we will see in Sec. 1.6.1.3, water models properly reproducing their structural and dynamical properties treat all atoms individually. As several water structural and dynamical properties are computed along this study, we have adopted, then, AA models for water. For the rest of species, the number of molecules in the simulation box is orders of magnitude lower than that of water molecules. Then treating all atoms individually does not have an important effect in the computational resources needed to perform the simulations. As a consequence, for the results shown along this thesis, we have adopted only AA models.

1.4 Measurable properties

1.4.1 Radial distribution function

The arrangement of atoms around one another in a particular direction, $\vec{r}$, can be studied by means of the radial distribution function, $g(\vec{r})$, defined as,[42,52]

$$\rho g(\vec{r}) = \left\langle \frac{1}{N} \sum_{i}^{N} \sum_{j \neq i}^{N} \delta[\vec{r} - \vec{r}_{ij}] \right\rangle \tag{1.146}$$

for a translationally invariant system. Here, N is the number of atoms in the system, $\rho = N/V$ is the number density, and δ accounts for the Dirac delta. For homogeneous and isotropic systems, however, we can replace $\vec{r}$ by simply the distance r between atoms, as there is not a privileged orientation. In that case, $\rho g(r)$ gives directly the average local density $\rho(r)$ at a distance r around an atom, and, hence, $g(r)$ indicates how the local density $\rho(r)$ around an atom deviates from $\rho = N/V$. The behavior of $g(r)$ presents different features depending on the phase of the system. For crystalline solids, where atoms occupy well-defined positions in a lattice, $g(r)$ has narrow peaks at those positions corresponding to the neighbors of each atom. For liquids, however, short range order prevails over long range order and oscillations are only observed some molecular diameters far from an atom. In this case, no deep valleys are observed between oscillations as happens in crystals, due to the larger mobility of the atoms in liquid phase. It is interesting to look at the value of $g(r)$ for small and long distances. For the first situation, if the interatomic distance approaches zero, the probability of finding an atom around one another is also zero, for long distances, as structural ordering is lost, the local density $\rho(r)$ approaches its average value ρ, and $g(r)$ tends to the unity. Finally, in a low density system, where atoms rarely see each other, $g(r)$ also vanishes for short distances, and only presents a maximum at a distance equal to the minimum of LJ potential. For $r > \sigma$, $g(r)$ tends to the unity very fast. Then, for dilute gases, $g(r)$ can be modelled as,

$$g(r) = \exp(-\beta U(r)) \tag{1.147}$$

where $U(r)$ is the pair potential between atoms.

The systems studied along this thesis, however, include molecules containing different kind of atoms. As we have seen in Sec. 1.3.4.3, non bonded interactions between molecules are described by pairwise potentials, hence, the use of site-site distribution functions is also adequate to study the structure of the system. The average local density of an atom β around an atom α, belonging to molecules j and i respectively, is obtained from the site-site pair correlation function $g_{\alpha\beta}(r)$ defined as,

$$\rho_\beta g_{\alpha\beta}(\vec{r}) = \left\langle \frac{1}{N} \sum_{i=1}^{N} \sum_{j\neq 1}^{N} \delta(\vec{r} - (\vec{r}_{i\alpha} - \vec{r}_{j\beta})) \right\rangle \tag{1.148}$$

where $\rho_\beta = N_\beta/V$. Unless we are interested in the study of the arrangement of a given atom in a particular direction around another kind of atom, the most adopted solution is to replace $\vec{r}$ by r in eq 1.148. To compute $g_{\alpha\beta}(r)$ numerically, we count the number of atoms β which lie in a spherical shell of radius r and width Δr around atom α, $N_\beta(r,k)$, at time step k. The result is then divided by the volume of the shell, $V(r,\Delta r) = 4\pi r^2 \Delta r$, and ρ_b to give $g_{\alpha\beta}(r)$:

$$g_{\alpha\beta}(r) = \frac{\sum_{k=1}^{M} N_\beta(r,k)}{M N_\alpha \rho_\beta V(r,\Delta r)} \tag{1.149}$$

where M is the number of samples taken to perform the equilibrium average.

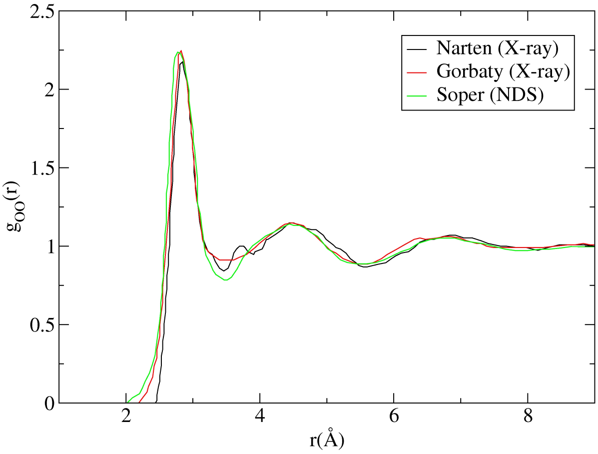

Figure 1.7: Comparison of reported experimental $g_{OO}(r)$ from X-ray scattering,[53,54] and from neutron diffraction scattering (NDS).[56]

Site-site pair correlation functions can be computed not also numerically, but also in a wide variety of experimental studies which involve techniques such as X-ray scattering,[53–55] or neutron diffraction techniques.[56]. In Figure 1.7 we show the oxygen-oxygen radial distribution function, $g_{OO}(r)$, calculated with different techniques. This property, hence, is of special interest in the study of liquids in front of others which do not have an experimentally studied counterpart.

1.4.2 Time correlation functions

A good way to characterize the dynamics for a given quantity is to follow its state with time. However, we may also be interested in see how different is the dynamics for a system compared to others, or to see how the value of a quantity influences others with time. A solution is to use time correlation functions.

Given two time-dependent quantities, $A(t)$ and $B(t)$, time correlation function, $C_{AB}(t)$, measures how the value of A at a given time is related to the value of B after a time t. Time correlation functions are defined as,[42]

$$C_{AB}(t) = \langle A(t_0)B(t_0+t)\rangle \tag{1.150}$$

where angular brackets stand for equilibrium average, and t_0 is the time origin. As $C_{AB}(t)$ is an equilibrium property, it is invariant under translations of the time origin, and hence, independent on it. Making use of the ergodic hypothesis, eq 1.150 can be rewritten as,

$$C_{AB}(t) = \lim_{T\to\infty} \frac{1}{T} \int_0^T A(t_0)B(t_0+t)dt_0 \tag{1.151}$$

where T is, in our case, the length of the simulation run or time period to perform the average. When A, and B are the same quantity, $C(t)$ is called *autocorrelation function*, otherwise, it is called *cross-correlation* function.

It is of interest to see the limiting values of $C_{AB}(t)$ at $t = 0$, and $t = \infty$. In the first case, there is no temporal separation between the value of the two dynamic quantities, and $C_{AB}(0)$ becomes a static correlation function,

$$C_{AB}(0) = \langle A(t_0)B(t_0)\rangle = \langle AB\rangle \tag{1.152}$$

For the autocorrelation function case, $C_{AA}(0) = \langle A^2\rangle \geq 0$. For long time separations, A, and B become uncorrelated, and $C_{AB}(t)$ reduces to,

$$\lim_{t\to\infty} C_{AB}(t) = \langle A\rangle\langle B\rangle \tag{1.153}$$

However, having time correlation functions, $C_{AB}(t)$, which do not decay to zero when A and B become uncorrelated is not very useful if we are interested in comparing them for different conditions. A solution is to shift the value for the quantities under study by their mean average, that is subtracting $\langle A\rangle$ and $\langle B\rangle$ from A and B. If we call δA, and δB these fluctuations, then, $C_{\delta A\delta B}(t)$ is written as,

$$C_{\delta A\delta B}(t) = \langle [A(t) - \langle A\rangle][B(t) - \langle B\rangle]\rangle = C_{AB}(t) - \langle A\rangle\langle B\rangle \tag{1.154}$$

When $t \to \infty$, $C_{\delta A\delta B}$ becomes zero. See that when A and B are the same quantity, $C_{\delta A\delta A}(0) = \sigma_A^2$.

This shift of the correlation function should only be done when correlations do not decay to zero at long times or if we are specially interested in studying the decay of the fluctuations for a given quantity. Some definitions of time correlation functions, however, are such that their long time limit is zero (see Section 2.2.2). In this thesis, we have computed several time correlation functions which in some cases can be compared directly to experimental data. In all cases, an explanation of how they are calculated is given in the corresponding section in the results chapter.

As we have seen, for long time separations, the influence of the initial value of a quantity on itself or on another quantity is negligible. This loss of memory means that a characteristic decay time for that correlation can be defined. This time is called correlation time τ_c and gives a measure of the time scale for $C(t)$ to decay to zero. As autocorrelation functions are highly used in the study of the dynamics of several properties, we constraint the definition of τ_c to those cases. Hence, τ_c is given by

$$\tau_c = \frac{1}{\delta A^2} \int_0^\infty \langle \delta A(0) \delta A(t) \rangle dt \tag{1.155}$$

The use of fluctuations inside the integral is mandatory if we want it to converge. When time correlation functions are defined such that they decay to zero for long times, then, correlation times are not necessarily calculated from fluctuations but from the correlation function directly. If a quantity is correlated even for long times, τ_c can be larger than the simulation time. In this case, there is no sense in calculating any correlation time.

Correlation functions can be used to compute the decay of the correlations for several quantities. A distinction can be established for correlation functions depending on the individual or collective behavior of the quantities involved. Examples of collective correlation functions are those related to the calculation of thermal transport coefficients such as shear viscosity, η, thermal conductivity, λ_T, or diffusion coefficients and also electrical properties such as electrical conductivity σ_e, all of them often calculated in MD simulations. Such quantities are calculated with the so-called Green-Kubo (GK) relations, which relate transport coefficients with integrals over time-correlation functions.[2,42] Diffusion involves a main chapter in this thesis, and the main fundamentals to its study in multicomponent mixtures are given in chapter 4 where examples of GK relations are given for the calculation of diffusion coefficients and electrical conductivities.

1.5 Data analysis: Principal Component Analysis (PCA)

High-dimensional data sets consisting of a large number of variables involve lots of calculations in order to infer the degree of correlation between them. For a system with m variables, one would have to compute $\frac{m(m-1)}{2}$ correlations. Then, if m is not small there is a need of taking into account another approach. One solution to this problem is to transform the original variables into a lower dimensional new set providing that the new ones account for most of the variation present in the original set and that they are uncorrelated between each other. This is the main idea behind principal component analysis (PCA).[57]

Let $\vec{x}$ be a vector of m random variables. If we have N observations for each variable, taken at discrete times t_i $(i = 1, \ldots N)$ then, the jth component of $\vec{x}$ corresponding to the ith observation is denoted by $x_j(t_i)$, where $j = 1 \ldots m$. The objective of PCA is to obtain a number p of linear functions of the m random variables called principal components (PCs) denoted as y_j $(j = 1, \ldots, p)$ where $p \leq m$. Each PC is uncorrelated with the others, representing the first PC, the direction of maximum variance of the m variables, and so on until the last PC which accounts for the direction of less variance in the system. Then, one can define a vector $\vec{y}$ where each component or PC is,

$$y_j = \vec{a_j}'\vec{x} = a_{j1}x_1 + a_{j2}x_2 + \cdots + a_{jm}x_m = \sum_{k=1}^{m} a_{jk}x_k \tag{1.156}$$

where $\vec{a_j}'$ denotes transpose of vector $\vec{a}_j$. The power of such a method is that if the first m^* PCs account for most of the variance present in the data given by $\vec{x}$, then the dimension of the vector to study is reduced from m to m^*.

The next step is how to obtain the different PCs from a data set given by $\vec{x}$ and how to measure the degree of variance of the original data represented by each PC. A measure of the degree of correlation between two variables x_j and x_k is given by the covariance S_{jk}, defined as,

$$S_{jk} = \frac{1}{N-1}\sum_{i=1}^{N}(x_j(t_i) - \bar{x}_j)(x_k(t_i) - \bar{x}_k) \tag{1.157}$$

where $\bar{x}_j = \sum_{i=1}^{N} x_j(t_i)$. One can consider all the covariances between all the m random variables of the vector $\vec{x}$ and define the so-called $(m \times m)$ covariance matrix S whose (j,k)th element is that given in eq 1.157. See that the diagonal terms $(j = k)$ are directly the variances of the m random variables, $S_{jj} = var(x_j) = \frac{1}{N-1}\sum_{i=1}^{N}(x_j(t_i) - \bar{x}_j)^2$. It can be shown that the m eigenvectors of S are directly the PCs.[57] Given an eigenvector $\vec{a_j}$ $(j = 1, \ldots m)$, if $\vec{a_j}'\vec{a_j} = 1$, the corresponding eigenvalue λ_j of $\vec{a_j}$ gives the variance of the jth PC, $var(y_j) = \lambda_j$. Then, the idea is to order the eigenvectors by the magnitude of its eigenvalue and take the first ones as they retain most of the variation present in the data. The fraction of the total variance represented by $\vec{a_j}$, named as f_j is

$$f_i = \frac{\lambda_j}{\sum_{k=1}^{m}\lambda_k} \tag{1.158}$$

A common criteria is to consider only the first m^* eigenvectors providing that $\frac{\sum_{j=1}^{m^*}\lambda_j}{\sum_{k=1}^{m}\lambda_k} \geq 0.9$, which corresponds to the set of PCs that gather the 90% of the variance present in the data set given by $\vec{x}$.

As only a vector $\vec{x}$ of m random variables is needed to perform PCA, this technique has been widely used in different areas of knowledge for its simplicity and the power of its results.

1.6 Molecules

1.6.1 Water

Water is the most abundant liquid on Earth with seventy percent of the surface of the planet covered by oceans. Water also plays a key role in the most part of biological processes and without it, life would not exist as we know it. In fact, most of the living species contain a large percentage of water. Its peculiar properties make water an excellent solvent for many biomolecules. Many biological processes such as protein folding and synthesis, catalysis of biochemical reactions, or molecular transport, are driven by water and take place either in water or in aqueous environments. Hence, water has a fundamental utility not only in pure or medical sciences, but also in technological and industrial processes such as oil recovery, mining or corrosion inhibition. But what does make water so special?

1.6.1.1 Structure and hydrogen bonding

A water molecule is composed of one oxygen atom and two hydrogen atoms.[5] The electronic configuration of an oxygen atom is $1s^22s^22p^4$ while for each hydrogen atom it is 1s. Then, to form a water molecule, four of the 6 electrons of oxygen corresponding to 2s and 2p shells arrange in two sp^3 hybridized orbitals also called electron lone pairs. The other two electrons combine with the two hydrogen electrons forming two other sp^3 orbitals. Hence, oxygen shares a pair of electrons with each of the two hydrogens resulting in two covalent bonds. The lone pairs tend to minimize the electronic repulsion between each other, and also with the covalent bonds. As a result, the two hydrogen atoms and the lone pairs of electrons are arranged in near-tetrahedral symmetry around the oxygen atom with an HOH angle approximately equal to 104.5°. Although a water molecule has no net charge, electrons spend more time orbiting the oxygen than the hydrogens. This results in an asymmetrical distribution of charge with the oxygen more negatively charged and the hydrogens more positively charged. Water has, then, a permanent dipole moment described as a partial negative charge on the oxygen and a partial positive charge near the hydrogens. For a water molecule in the vacuum it is equal to 1.855 Debyes. Due to this asymmetry of charge, hydrogens attract other atoms negatively charged. In such scenario, the hydrogen atom lies between the oxygen belonging to the same water molecule and the other atom acting then as a bridge between them. This kind of interaction is known as hydrogen bond interaction.[59] In a water molecule, hydrogens *donate* hydrogen bonds while each lone pair of electrons on the oxygen

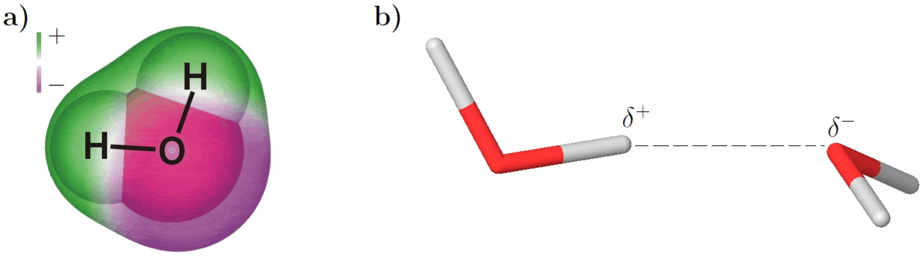

Figure 1.8: Structure of a water molecule in ball representation showing the charge distribution around its atoms (a),[58] and hydrogen bonded water dimer (b).

atom accepts hydrogen bonds from other water molecules. Hence, hydrogen bonding introduces an important orientation dependence into the intermolecular interactions of water molecules. Tetrahedral hydrogen bonding arrangement is common in ice, however liquid water also has tetrahedral symmetry as seen, for instance, from the oxygen-oxygen pair correlation functions. In this case, the first peak has a width lower than for other liquids indicating a more ordered structure for the first neighbor shell. An explanation of this degree of structure even in the liquid phase is the so-called hydrogen bond cooperativity.[6,60] This means, that the strength of an HB depends on the neighboring HBs. When a water molecule named A accepts an HB via its oxygen, the electron density shifts towards the molecule which is donating the HB, named B. Hence, the two hydrogens of molecule A become more positively charged and can donate easily an HB to other water molecules. This cooperativity explains the existence of clusters of several water molecules in bulk water or the polygonal cages which water molecules form when solvating solutes.[61–64] In fact, due to its polar behavior, water can solvate a wide range of polar, hydrogen bonding molecules and ions. In this case, the structure of water around charged molecules is driven by the electrostatic interaction between them. If ion-water interactions are dominant in front of water-water and ion-ion interactions, then there is a high solubility of ions in water (see Figure 1.9).

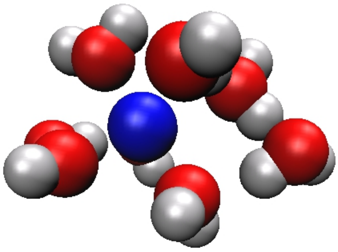

Figure 1.9: Solvation of a Na^+ cation in water in ball representation. Water oxygen atoms orient towards the positive charged sodium due to their partial negative charge.

When non polar solutes as oils are mixed with water, the process of solvation becomes quite different. We can write the change of molar free energy ΔG of transferring a nonpolar solute from its liquid phase into water, in terms of molar enthalpic and entropic components $\Delta G = \Delta h - T\Delta S$, where Δh is the molar enthaply and ΔS the molar entropy. In cold water, for a wide range of temperatures and nonpolar solutes, the change in free energy is positive, indicating an aversion of oil for water. In fact, when a nonpolar solute is mixed with water, water molecules orient around the solute to avoid wasting hydrogen bonds. This results in a very ordered first-shell of water molecules which have better HB, on average, that in tetrahedral pure water. As the entropy is a measure of the order in the system, it is reduced when the nonpolar solute is mixed with water and, then, $\Delta S < 0$. On the other hand, the interaction of the solute with water has a more favorable enthalpy $\Delta h \approx 0$, which gives a positive change in free energy. This aversion is also known as *hydrophobic* solvation and shows that the structures of water around nonpolar solutes in cold water is driven by the maximization of water-water hydrogen bonds.[65] When more than one nonpolar solute are mixed with water, they associate to reduce their net surface area of contact with water. That is, if the solutes are solvent separated, more water molecules are ordered around them, but when they get in contact, the solute-solvent surface area is reduced and the change in entropy becomes more positive. This entropy-driven attraction is called *hydrophobic interaction.*[65,66] However, beyond the critical point, water becomes supercritical, and it exists as small but liquid-like HB clusters dispersed with a gas-like phase, the dielectric constant of water is extremely reduced due to the reduced hydrogen bonding network and then it becomes an excellent solvent for nonpolar solutes but a poor solvent for electrolytes. In this study all the MD simulations have been performed around room temperature or at temperatures lower than the range in which water becomes supercritical, then, the structure of water around solutes has to be driven by the explained processes.

1.6.1.2 Anomalous properties

As compared to other liquids, water presents many unusual properties mainly derived from its ability to form HBs with other water molecules. This cohesive nature of water results, for example, in high boiling, melting and critical temperatures.[66] As a given energy is required to remove a molecule from the HB network, water has a relatively large heat capacity for its size. Water also has a high dielectric constant and surface tension. Another subtle property of water is that pH changes through the liquid faster than predicted by the self-diffusion coefficient for hydrogen atoms. This process can be also explained in terms of the HB network as it is suggested that H^+ ions are transported rapidly from one water that donates the hydrogen to a next one and like this successively.[6,67]

Similar peculiarities in water are observed in wide range of temperatures and pressures. However, is at low temperatures where the behavior of several structural and dynamical properties present the so-called *anomalies* of water. For high temperatures, heating water results in a volume increase and a less dense liquid, due to the greater thermal motions as observed in most substances. However, upon melting, the volume of water decreases when increasing the temperature giving a dense liquid. The explanation also comes from the arrangement of water molecules in HBs. That is, in ice the kinetic energy is lower, and the HB tetrahedral network of water molecules is open. When heating, the resulting distorted tetrahedra are denser than for ice giving a decrease in volume. This anomaly affecting volume and density is manifested in the fact that ice floats in water. The most interesting aspect is that the decrease in density when cooling occurs below 3.984 °C (see Figure 1.10a). Below this temperature, cooling water results in a lighter liquid. This temperature is called the temperature of maximum density (TMD). This anomaly is manifested in some response functions as the thermal expansion coefficient, $\alpha_T = (1/V)(\partial V/\partial T)|_P$, which is positive for $T >$TMD and negative for $T <$ TMD, as opposed for typical liquids where it is always positive.[68]

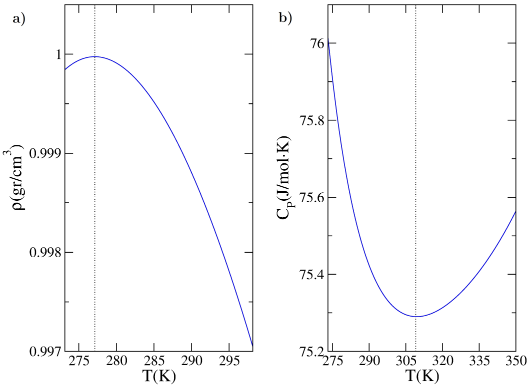

Figure 1.10: (a) Density of water, ρ, versus temperature T, at $P = 1$ atm. Maximum density is observed at $T =$TMD. (b) Heat capacity of water, C_p, versus temperature T also at $P = 1$ atm. This function has a minimum at $T = 308$ K. Source: NIST data base.[69]

The slope of the $P(T)$ liquid-solid coexistence line also reflects the volume anomaly of water, giving a negative slope compared to the positive value for simple liquids. Then, applying pressure to ice melts it, resulting in a denser phase. Other response functions as the isothermal compressibility, $\kappa_T = (1/V)(\partial V/\partial p)_T$, show an anomalous behavior.[68] Above 319 K increasing the temperature involves looser systems and hence more compressible. This is observed in most liquid systems. For cold water, the process of heating involves having a denser, less compressible system and a lower κ_T, which at 319 K (not at TMD) has a minimum. The heat capacity also has a similar form as a function of T but with the minimum located at $T = 308$ K (see Figure 1.10b).[66]

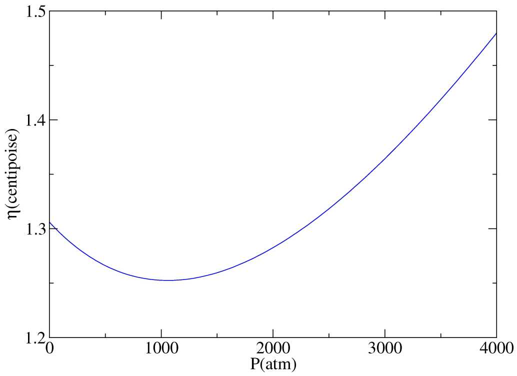

Figure 1.11: Viscosity of water versus pressure P at $T = 283.15$ K. Source: NIST data base.[69]

Not only structural properties present anomalies for water, several dynamic properties have a peculiar behavior as a function of thermodynamic variables. An example is the self-diffusion coefficient which for most liquids decreases upon pressuring. For water, instead, diffusivity increases with pressure for a large region in the (P, T) plane which includes the region of density anomaly.[70–72] In this case, when pressure is increased more HBs are broken, and then more water molecules diffuse from their neighbors. In the low pressure regime, viscosity also has an anomalous behavior as it decreases with an increase of temperature (see Figure 1.11).

However, the anomalous properties of water do not only appear in the vicinity of the freezing point. Water, for example, can be supercooled to 233.65 K at 1 atm remaining liquid if ice nucleation is prevented. Glassy water, also known as *amorphous ice*, can exist for temperatures below the glass transition temperature $T_g \approx 136$ K. Two main kinds of amorphous ice called low-density ice (LDA) and high-density amorphous ice (HDA) are known for water,[73–75] this phenomenon is called *polyamorphism.*[76] In this supercooled region, the anomalies of water get more enhanced. For instance, the response functions cited above, that is α_T, κ_T, and C_p diverge as the temperature approaches 228 K. Such divergence often indicates a phase transition. The microscopic origins of this behavior, are not easy to infer from experiments since below the homogeneous nucleation temperature, $T_H \approx 235$ K, bulk water crystallizes. In fact, the region of the phase diagram located between T_H and the so-called crystallization temperature $T_X \approx 120$ K is a kind of *no-man's land*, where experiments on the liquid phase cannot be performed. Hence, many theoretical and numerical analyses have tried to explain water's anomalous behavior in the supercooled region.[77–81] In this case, different interpretations, consistent with experiments, have been given to such behavior. In the *singularity free* (SF) scenario, response functions do not diverge at low temperature.[82] The large increase is due to the local density fluctuations consequence of the low T-anticorrelation between volume and entropy. The existence of a second critical point in the supercooled region, has, instead, been suggested to exist around a pressure $P_c \approx 100$ MPa and temperature $T_c \approx 220$ K.[83] This second critical point is then the end point of a first-order phase transition line separating two kinds of liquid phases: a low-density liquid (LDL), with local tetrahedral order, and a high density liquid (HDL), with a disordered structure. The two amorphous forms of ice cited above, would correspond to two forms of ice corresponding to the HDL and LDL liquids. Other scenarios, as the stability limit (SL)[84] or the critical-point free (CPF)[85], have been proposed in the literature in order to explain the behavior of water in the supercooled region.[86]

1.6.1.3 Water in MD simulations

Several water models aiming at reproducing structural and experimental properties of water, through molecular simulation techniques, have been used since 40 years ago. Water models can be classified into three groups: rigid models, where the water geometry is kept fixed; flexible molecules, which permit vibration of intramolecular bond distances and angles; and polarizable models, which explicitly include polarization effects. Despite the existence of O-H bond, and H-O-H angle vibration in real water, including vibrational degrees of freedom in an MD simulation involves considerably reducing the integration timestep with the associated computational cost. At the same time, mixing classical MD simulations with molecular flexibility can lead to the introduction of undesired artifacts and do not necessarily improve the obtained results. The most adopted solution is to use rigid models. Rigid water models involve a particular geometry of the molecule, a set of point charges associated to the atoms or to specific sites in the molecule and a set of LJ parameters (σ, ϵ) for such sites. These parameters are usually optimized to reproduce the experimental density and heat of vaporization at room temperature. Despite the fact that rigid models omit flexibility, polarization and quantum mechanical effects, they reproduce structural, thermodynamic and dynamical properties of bulk water very well with the advantage of computational economy. The first simulation of liquid water used the Ben Naim-Stillinger (BNS) rigid model.[87,88] This was a five interaction site model accounting for the hydrogens, the oxygen, and the lone electron pairs with four point charges. Several models appeared then as the ST2 model,[89] the SPC (simple point charge) model family, or the TIPnP (transferable intermolecular potential with n sites) model family.

The SPC water model consists on a tetrahedral model with an OH distance of 1Å, an HOH angle of 109.47°, and point charges, $q_{\mathrm{H}} = +0.41$, and $q_{\mathrm{O}} = -2q_{\mathrm{H}} = -0.82$, located at the hydrogens and oxygens respectively. A single LJ interaction site is located at the oxygen. Although SPC model behaves quite well for several purposes, it does not reproduce correctly many dynamical properties such as diffusivity or viscosity of bulk water, where values of $4.2 \cdot 10^{-9}$ m^2/s, and 0.49 cP are obtained for the self-diffusion constant and viscosity compared to the values of $2.3 \cdot 10^{-9}$, and 0.85 cP from experiments at $T = 300\mathrm{K}$.[90–92] At room temperature, for instance, it underestimates the static dielectric, $\epsilon(0)$, constant and the system density. The radial distribution function can also be improved. In water, there is a considerable average polarization, which leads to a cooperativity in the formation of HBs between molecules, Such effect is neglected in the SPC model. A solution, is to include a positive self-energy E_{pol} accounting for the energy cost of distorting a molecule to its polarized state. As polarizability can not be explicitly accounted when using rigid water models, an average value has to be taken for E_{pol}. The extended simple point charge model (SPC/E) corrects for this fact by adding a self-polarization correction to the electrostatic energy of 5.22 kJ/mol.[26] In this case, the scheme of the model is similar to the SPC, but the values of the point charges are slightly changed to $q_{\mathrm{H}} = +0.4238$, and $q_{\mathrm{O}} = -0.8476$. The value for the system density gets now close to the experimental value for bulk water. An important improvement of the SPC/E model is that the values for the diffusion constant and viscosity gets close to the values from experiments. Also the static dielectric constant approaches the experimental value. There is quantitative agreement in the obtained values for the site site radial distribution functions. However, the height of the first peak in the oxygen-oxygen radial distribution function, $g_{\mathrm{O-O}}(r)$ is higher than observed in NDS experiments. The position of the second peak is slightly shifted to the left with respect to the experimental value. Nevertheless, this last point is improved with respect to the SPC model and many other models, and it must be said that all rigid water models underestimate the position of the second peak in the $g_{\mathrm{O-O}}(r)$. Several extensions of the SPC model have been developed in the last decade. Rigid extensions are the SPC/A, SPC/L models which despite improving the value for some quantities such as the heat capacity C_p fail at reproducing correctly diffusivity and viscosity values.[90] Flexible versions of the SPC model are the SPC-F1, SPC-F2, UB1-SPC, SPC/F and the SPC/G models.[93–96] As in the present study we are interested not only in computing structural properties, but also dynamical properties of systems containing water, such as diffusion coefficients, we have chosen the SPC/E model as it has been widely used in the literature for that purpose. Although SPC/E shows a good performance when describing liquid water, it does not provide an accurate description of the low-T region of the phase diagram of water.[97] A model which is remarkably good at qualitatively describing water's phase diagram is the TIP4P model.[98] The main difference between TIP4P and the described SPC water models, is that although the positive point charges are still located in the hydrogens, a negative point charge is located 0.15 Å away from the oxygen along the H-O-H bisector. The values for the rest of parameters are given in Table 1.1. Despite the fact that TIP4P is a nontetrahedral model, it exhibits all the tetrahedral arrangements of the ice phases of water. For instance, ices I, II, III, V, VI, VII, and VIII are found to be stable phases when using TIP4P model, while ice IV and ice IX are

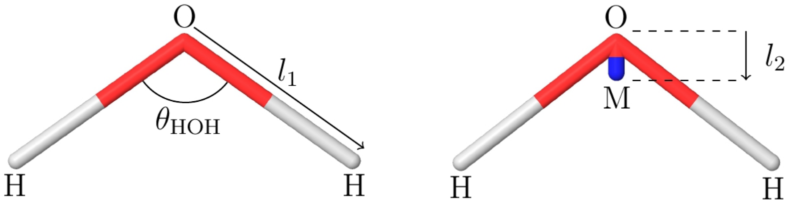

Figure 1.12: Geometry of the SPC/E (left) and the TIP4P (right) water models. In both cases, only one LJ interaction site is located on the oxygen. In the SPC/E model, the negative partial charge is located on the oxygen, while in the TIP4P model it is located on the dummy atom M.

clearly metastable phases (as in real water). For SCP/E, instead, only ices II, VI, VII, VIII are stable solid phases, while ices IV and IX are metastable. A major defect of the SPC/E water model is that it predicts that ices III and V are metastable.

Table 1.1: Parameters for the SPC/E and TIP4P water models.

model	σ_{O} (Å)	ϵ_{O} ($\frac{\mathrm{kJ}}{\mathrm{mol}}$)	q_{O} (e)	q_{H} (e)	q_{M} (e)	l_1 (Å)	l_2 (Å)	θ_{HOH} (°)
SPC/E	3.16600	0.6502	-0.8476	+0.4238	-	1.0000	-	109.47
TIP4P	3.15365	0.6480	0	+0.5200	-1.04	0.9572	0.15	104.52

The thermodynamic conditions chosen in all MD simulations performed along this study, are not proper of the region where water becomes solid-like, hence, the SPC/E water model is still recommended. However, as in a part of the thesis we deal with confined systems containing water we have also performed some MD simulations using the TIP4P water model in order to see whether the choice of the potential can lead to different water structure.

1.6.2 Polyoxometalates

1.6.2.1 Basic principles

Polyoxometalates (POMs) are inorganic metal oxygen cluster anions. In 1826, Berzelius was the first to describe a POM, and since then marked attention has been shown to them. POMs are formed by the arrangement of MO_n units where M stands for the metallic center, also known as *addenda* atom, and n is the coordination number. An important number of early transition elements such as molybdenum, vanadium or tungsten have the ability to form a large variety of POMs.[18] For instance, Mo(VI), W(VI) or V(V) are POM formers par excellence. The formation of MO_n units depends both on the appropriate relationship of coulombic factors such as ionic radius and charge, and the accessibility of empty d orbitals for metal-oxygen bonding. When only MO_n units are present in the POM structure, the cluster anions are called *isopolyoxoanions*, ($[\mathrm{M}_m\mathrm{O}_y]^{q-}$), where $q-$ is the charge of the POM. An example of such structure is the Lindqvist anion. Other elements called heteroatoms (X) can be incorporated to the POM giving place to *heteropolyoxoanions* ($[\mathrm{X}_x\mathrm{M}_m\mathrm{O}_y]^{q-}$). A large number of elements from all parts of the periodic table, except the noble gas elements, are known to be heteroatoms. The presence of different heteroatoms gives place to clusters displaying varying stochiometries and diverse structural cores. Examples of heteropolyoxoanions are the Keggin anion or the Wells-Dawson anion.

POMs can be formed by different types of MO_n polyhedra arranged between them. The most common is the octahedral MO_6 unit and the square pyramid MO_5.[99–101] Other basic units are the MO_4 tetrahedra,[102] and the MoO_7 pentagonal bipyramid (see Figure 1.13). In such units, the metal atoms are displaced, as a result of MO π-bonding, towards one of the polyhedral vertices. A wide number of POMs are viewed as arrangements of edge-and vertex sharing MO_6 octahedra, each with one or two unshared vertices also called terminal oxygens. Polyanion structures containing three or more terminal oxo groups are not observed.[99]

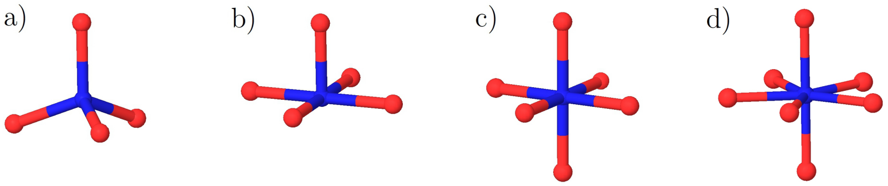

Figure 1.13: Examples of MO_n POM building blocks in ball-and-stick representation. (a) MO_4 tetrahedra, (b) MO_5 square pyramid, (c) MO_6 octahedra and (d) MO_7 pentagonal bipyramid (M blue, O red).

1.6.2.2 Giant polyoxometalates

Building blocks containing molybdenum atoms are responsible of giant POMs with sizes on the order of the nanometer. An example is the giant wheel $[M_{154}(NO)_{14}O_{434}(OH)_{14}(H_2O)_{70}]^{28-}$, $\{Mo_{154}\}$, structurally generated by linking 140 MoO_6 octahedra and 14 $MoO_6(NO)$ pentagonal bipyramids, with a radius of about 3.7 nm (Figure 1.14).[103] More interesting are spherical POMs. In this case, a central MoO_7 pentagonal bipyramid shares edges with five MoO_6 octahedra forming a pentagonal $\{(Mo)Mo_5\}\equiv[(Mo)Mo_5O_{21}]^{6-}$ group. Each of these building groups are linked between each other with MoO_6 octahedra sharing corners with atoms of the pentagon. Extended structures $(\text{pentagon})_{12}(\text{linker})_{30}$, also called keplerate-type structures, with icosahedral rotational symmetry, I_h, define

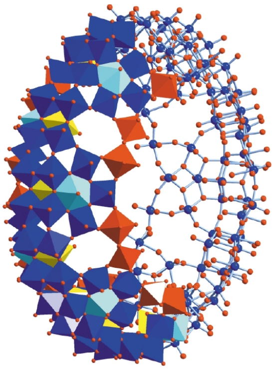

Figure 1.14: The structure of the Mo_{154} wheel, half in polyhedral representation with different building units (Mo_8 blue, Mo_2 red, Mo_1 yellow), and half in ball-and-stick representation (Mo blue, O red).

a wide range of spherical shaped POMs. In 1998, the first spherical nanostructured keplerate cluster $\{Mo_{132}\}\equiv[\{Mo_2^V O_4(CH_3COO)\}_{30}\{(Mo)Mo_5O_{21}(H_2O)_6\}_{12}]^{42-}$ was synthesized.[104] In this case, the $\{(Mo)Mo_5O_{21}\}$ groups define the vertices of an icosahedron which are connected by 30 $[Mo_2O_4]^{2+}$ linkers. Experimentally, it is possible to synthesize POMs with 12 $\{(Mo)MO_5\}$ groups but with a different type of linkers as $[Mo_2O_4]^{2+}$ or Fe^{3+}, and ligands as CH_3COO^-, SO_4^{2-}, or HCO_2^-. In particular, spherical POMs with $[Mo_2O_4]^{2+}$ linkers and tuneable ligands, L, $[\{(Mo)Mo_5O_{21}(H_2O)_6\}_{12}\{Mo_2O_4(L)\}_{30}]^{72-}$ have attracted much attention in recent times due to the large available space in its interior which can host molecular species confined inside (Figure 1.15). Such POM nanocapsules have 20 $[Mo_9O_9]$ pores (Figure 1.15 c). Changing the size and charge of the internal ligands, and/or adding specific ions capable of closing the pores, modifies the total charge of the POM internal surface and also the available space for guest molecules. Then, the effect of the confinement on host molecules can be studied, not only from experiments (X-ray), but from molecular simulations. The analysis of POMs in aqueous solution, also permits to study the transport of the confined molecules through the pores.[105]

POMs have remarkable catalytic, magnetic, redox, and photophysical properties, being, then, important as reagents in analytical procedures, as industrial catalysts, and also for potential clinical applications. Hence, POM synthesis has become increasingly interesting due to the possibility of tuning the cluster

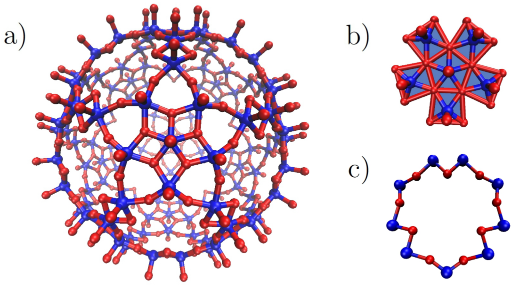

Figure 1.15: Structure of the Mo_{132} spherical POM nanocapsule without internal ligands (a). Representation of a $\{(Mo)Mo_5\}$ building group (b), and structure of a Mo_9O_9 pore of the POM surface (c).

properties and high progress is expected in next years.

Chapter 2

Dynamics of Encapsulated Water inside $Mo_{132}(SO_4)$ Cavities

2.1 Introduction

Encapsulation of molecules at the nanometric scale offers the possibility of exploring the behavior of liquids and solutions under special conditions that are not encountered in bulk systems. The enormous physicochemical and biological impact of water and water solutions under confinement is of special interest.[106–110] The anomalous behavior of water has been the subject of extensive studies since long ago, often relating its peculiar behavior to the existence of two forms of structural order in bulk water[111,112]. That would lead to a liquid-liquid phase transition between a high density water (HDW) and a low density water (LDW) if its hypothetical critical point were not buried under the liquid-solid phase transition line[113–115]. In the same spirit but with a different perspective, a structural order parameter has been conjectured for liquid water to describe the anomalous behavior of transport coefficients near the freezing point for liquid water at 1 bar[116–118]. However, a clear description of these order parameters in terms of microscopic variables is still lacking.

Studies of water confined in different structures range from graphite channels[7], carbon nanotubes[8–10], silica pores[119,120], and mica surfaces[121], among others. In recent times, water confined in reverse micelles, RMs,[11–13] has attracted intense investigations both theoretically[14–17] as well as experimentally.[122–125] Metal oxide based nanocapsules[20] have been shown to constitute a suitable alternative to study the behavior of confinement systems, particularly water and cations of different complexity. These studies show that water under confinement displays some general trends that differ from bulk water. For example, water-confining surface interaction and the geometry of the container are the key factors inducing modifications in both short- and long-range order of water that affects both the structure and the dynamics of the processes taking place. Computational studies of water inside nanopores show that water molecules organize in layers depending on the geometry of the confinement. The properties of water molecules in contact with the confining surface (outer layers) are different from those at a further distance from the surface (inner layers). For hydrophilic surfaces, water molecules in the outermost layer have slower dynamics and the structures displayed are strongly influenced by the surface, as a consequence of the strong hydrogen bonds (HB) established between the water and the hydrophilic sites of the latter. This effect forces particular orientations for water molecules near the surface that induce distortions with respect to the natural structure in bulk water. The most remarkable of these effects is that confinement destroys the three-dimensional hydrogen bond network of bulk water to produce an arrangement of the particles forming layered structures, which can be connected between them in an irregular way, through hydrogen bonds. Some authors[119,126,127] separate water molecules in confined systems into *bound water*, which refers to those in contact with the surface, and *free water*, for the rest. The same has been conjectured from results obtained in RMs.[14,124,128,129] The mean number of hydrogen bonds per water molecule also reflects that distinction.[119,120,130] Reorientational dynamics, diffusivity, and dielectric properties of water under confinement have also been studied. Molecular dynamics (MD) simulations of water inside graphite channels[7] show an increase of 4 ps in the mean time of reorientation of bound water, as compared to that of bulk water ($\tau_{\mathrm{bulk}} = 4.9$ ps), when the separation between graphite plates is 3.1 nm. When the plate separation is 1.2 nm, the increase rises up to 11 ps. Martí and co-workers,[7] have also shown that the self-diffusion coefficient decreases, as well as the dielectric constant increases, by a factor between 1.5 and 3 when comparing the behavior of bound and free water for the channel widths studied.

In this chapter, we present MD simulations of water confined in a polyoxomolybdate $Mo_{132}(SO_4)$ metal oxide nanocapsule, as far as structural and dynamic properties are concerned. Due to the fact that AOT RMs of comparable size have been extensively studied, our analysis permits one to analyze the effects the characteristics of the container have on the observed properties.

AOT RMs are ternary systems formed by sodium bis(2-ethylhexyl) sulfosuccinate (AOT surfactant), a nonpolar solvent, and water in appropriate ratios. The size of the micelle is given by the parameter w_0, defined as the ratio between the total water to the total surfactant concentrations.[131] This system gives nearly spherical micelles with a rather soft container, negatively charged, and the corresponding number of cations (Na^+, K^+) dissolved in the aqueous phase. RMs with $w_o = 4$ and 5 contain, respectively, 140 and 300 water molecules. The giant molybdenum polyoxometalate $Mo_{132}(SO_4)$ studied in this chapter is a structure constructed from building blocks consisting of assemblies of one pentagonal MoO_7 unit with five MoO_6 (referred to as $(Mo)Mo_6$ moieties) connected by MoO_6 linkers.[18] This rather rigid structure has 20 gates that can be blocked by functionalizing the inner cavity with the appropriate number of SO_4^{2-} anions. The total charge of the system is -72 which is compensated by the appropriate number of counterions outside. This system can host up to 172 water molecules, which makes it equivalent to $w_0 = 4$ RM. Giant polyoxometalates (POMs)[18,19] of different sizes have attracted some attention in recent years. By tuning the overall charge and the geometry of the internal POM's surface, the structure of the ensemble of encapsulated molecules varies. In a recent paper,[20] we have

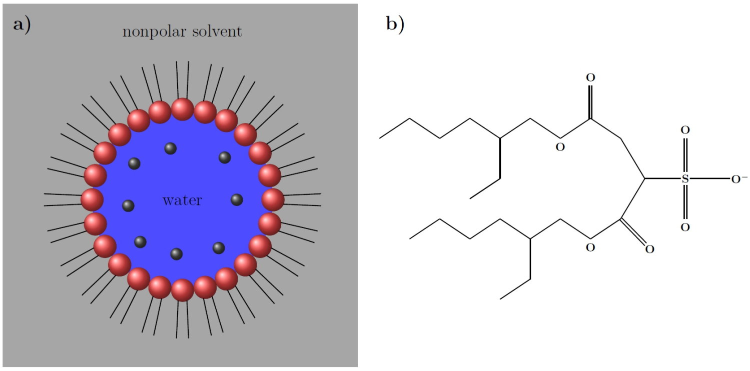

Figure 2.1: (a) Coarse-grained representation of an AOT reverse micelle. The anionic surfactants are represented by a sulfonate headgroup (in red) and a hydrophobic tail. Sodium Na^+ cations are also shown (in black). (b) Chemical structure of the AOT molecule.

studied the $[\{(Mo)Mo_5\}_{12}\{Mo_{2-}(L)\}_{30}]^{n-}$ ($L{=}SO_4^{2-}$ and HCO_2^-; $n = 72$ and 42) porous nanocapsules, which are referred to as $Mo_{132}(SO_4)$ and $Mo_{132}(HCO_2)$, respectively. X-ray data for $Mo_{132}(SO_4)$ at $T = 188$ K show that the confined water can be described as forming three clearly defined concentric layers (100 molecules) plus an additional water layer bound to some Mo atoms of the cavity. When, instead, formate functionalizes the system ($Mo_{132}(HCO_2)$), the same number of water molecules is trapped in the cavity, but surprisingly, they organize in four plus one distinct loose layers.[20] The layered structure has also been observed by us using molecular dynamics simulations in both cases which, in addition, show that structural changes occur as the temperature increases.

Centering our attention on the $Mo_{132}(SO_4)$ capsule, X-ray measurements indicate that the outer water layer is very rigid due to the strong interaction of water with the metal atoms of the 12 $(Mo)Mo_5$ moieties. These wall structures form 12 $\{(H_2O)(H_2O)_5\}$ pentagons that force a certain geometrical organization of the neighboring water layer. As in other confining systems, due to the HB interactions, the structure of the inner layers of water still retains part of this superimposed geometry, although it is progressively lost as the geometrical center of the capsule is approached. The ability of water molecules to form hydrogen bonds suggests that the observed layered structures must be the result of the competition between the energy of formation of the HB network and the constraints due to the confinement. Hence, the physically HB connected structures appear as layered structures that are related to those of buckminsterfullerene (buckyball water clusters).[132,133]

Our simulations, therefore, address a detailed analysis of the dynamics of water molecules in such a strongly structured system which has no counterpart in the RMs neither in the $Mo_{132}(HCO_2)$ where only the distinction between bound and unbound water can clearly be made. Our interest is centered on the evaluation of the dynamics of the water layers, the time scales related to a water molecule in a given layer, as well as the permeability of the layers to the transfer of water molecules across them, as a function of the position of the layer. We find that different spectra of these correlation functions behave as power laws $\nu^{-\alpha}$ at low frequency. Simulations of bulk water also show an analogous power law behavior, when the power spectrum of the fluctuations in the electrostatic energy is calculated. Such a *flickering noise* has been conjectured as being originated by the relaxation of the HB network, following processes similar to self-organized criticality (SOC).[134] However, we relate this behavior to the combined effect of the HB network and the hindrance of diffusion due to the confinement. This effect would make it so that two water molecules, initially hydrogen bonded, remain long time correlated due to their relative spatial location, thus allowing the occurrence of many breaking and reforming HBs. However, it must play a relevant role, specially at long time, the occurrence of occasional HB between different layers and the related processes of exchange of molecules between these layers.

Aiming at a possible comparison with experimental data obtained for this system, we have evaluated correlation functions relevant for infrared spectroscopy that has been widely used for similar analyses in RM systems.

The chapter is organized as follows: In section II, the methods used to compute the different properties of our system are presented. Section III is devoted to the technical details of the simulations and the routines used to compute the properties. Subsequently, in section IV we present the main results and finally, address the conclusions in section V.

2.2 Fundamentals

In this section, we describe the tools that we employ in the analysis of the structural and dynamical properties of confined water into $Mo_{132}(SO_4)$. In the first part, we describe the layering of water in the cavity and introduce a new interpretation of the structure presented in ref [20] as well as the appropriate notation for the subsequent discussion. We have emphasized the analysis of the collective properties of the layers. Furthermore, we introduce other quantities of interest that have been reported in the literature for confined water, particularly in reverse micelles. Therefore, in the first place, we define the hydrogen bond and the appropriate correlation function that describes its dynamics. Second, we introduce the infrared absorption spectrum, aiming at analyzing the expected behavior of the system if experimentally studied with this technique. Furthermore, we also focus our attention on the orientation of water molecules in the cavity and its corresponding dynamic behavior, which can also be experimentally accessible. Finally, we also describe the tetrahedral order parameter to be used later.

2.2.1 Water Layer Analysis

The experimental X-ray measurements of ref [135] indicate that at T=188 K water forms well-defined polyhedra inside the $Mo_{132}(SO_4)$ cavity. From these data, a first layer formed by 12 isolated pentagons, with six water molecules each, corresponds to the water molecules coordinated to the $(Mo)Mo_5$ moieties. Next, a $\{H_2O\}_{60}$ rhombicosidodecahedron (see Figure 2.2a) which is followed by a third layer of 20 molecules whose structure is dodecahedral $\{H_2O\}_{20}$. Finally, another dodecahedron $\{H_2O\}_{20}$ forms the more internal layer. These structures have been constructed only on the basis of the distance to the center of the cavity, and this construction only reflects their geometrical shapes. However, the physically relevant structures should be made out of molecules connected by HB among themselves. According to this hypothesis, we suggest that the observed physical structures should have the following properties: (a) each water molecule is related by hydrogen bonds to three neighboring molecules belonging to the same layer, (b) for the former to be true, the distances between the molecules should be short enough for the HB bond to exist, and (c) the pentagons are oriented such that they lie under the pentagonal structures originated in the outermost layer. This last condition implies that the 12 pentagons belonging to the different structures cannot be formed at any position but at fixed locations imposed by the rather immobile 12 pentagons bound to the inner wall of the POM. Therefore, the second and third layers of ref [20] can be reinterpreted as being a unique structure similar to a distorted $\{H_2O\}_{80}$ buckyball. According to Euler's theorem,[136] if n_w is the number of water molecules in the structure and h is the number of hexagons, it must be satisfied that $n_w = (12 \times 5 + h \times 6)/3$, if the number of vertices per molecule is three. Then, the $\{H_2O\}_{80}$ layer contains 30 hexagons, in addition to the 12 pentagons, to give the observed 80 water molecules (see Figure 2.2b). From this point of view, the third $\{H_2O\}_{20}$ layer also corresponds to a buckyball structure with $h = 0$ and, hence, only 12 pentagons. Therefore, except for the layer directly in contact with the wall, all physical structures can be described as forms of such buckyball geometry, with different numbers of water molecules, interconnected through HB.

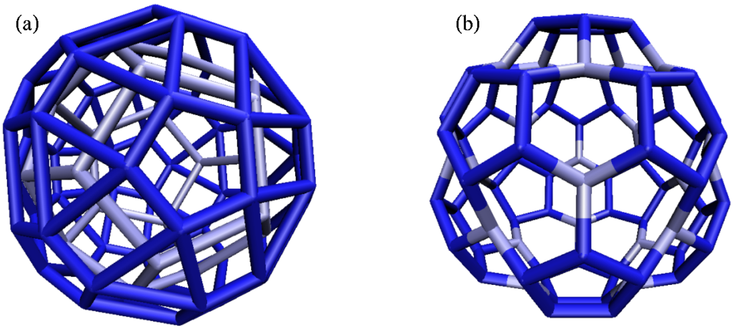

Figure 2.2: Comparison between the geometric structures suggested in ref [135] (a) and the physical buckyball-like structure $\{H_2O\}_{80}$ (b) connected through HB.

At higher temperatures ($T = 298$ K), however, the stability of these physical layers will depend on the free energy of the system. It is then expected that simulations performed at higher temperature would display a different water distribution with imprint of a higher randomness due to the increase of the thermal energy per particle. Indeed, in the previous study,[20] we observed from MD simulations analogous buckyball structures from the spatial distribution function (SDF). In Figure 2.3, we plot the radial distribution function $g(r)$ (see ref [42]), giving the local normalized density of water molecules with respect to bulk water for the $Mo_{132}(SO_4)$, both under ambient conditions.[137] In this figure, four peaks are observed. Peak ϵ corresponds to the outermost layer, where water molecules are strongly bound to the metal atoms of the POM's wall. Peaks δ_A and δ_B are the structure corresponding to the layer $\{H_2O\}_{80}$ that we have described above. Here, however, the average number of molecules is estimated to be around 72. The splitting of the δ peak into two is due to different position of the vertices forming the pentagons, δ_B, and two of the vertices forming the hexagons, δ_A, according to Figure 2.2b. The water molecules detected in peak γ correspond to the $\{H_2O\}_{20}$. Finally, at 298 K, an additional peak β is observed very close to the center of the cavity with an average number of about four molecules.

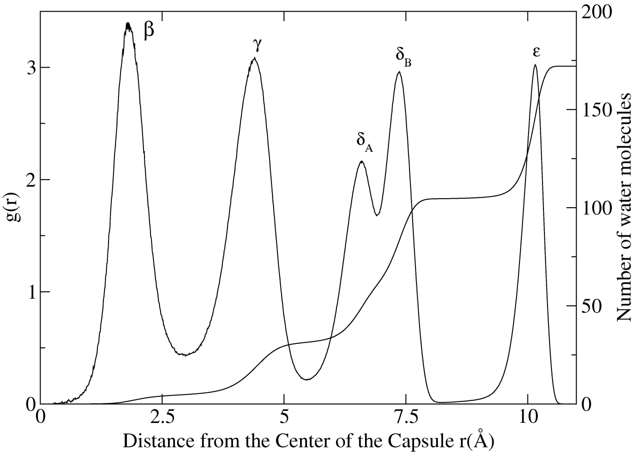

Figure 2.3: Radial distribution function $g(r)$. Confinement involves the formation of four layers as observed from the four peaks. Notice that this $g(r)$ does not tend to 1 in the range of distances of the figure due to the presence of the capsule's wall.

In ref [20], we also plotted the SDF, giving the regions with a larger probability of presence of the oxygen of a water molecule, showing the structure of about 72 molecules in which the original $\{H_2O\}_{80}$ has transformed into. Effectively, the increase of the temperature has made it so that some water molecules have migrated from the external water layers into the center of the cavity. Then, the δ layer would, in principle, tend to form a buckyball structure with the 12 pentagons and 26 hexagons. However, the strong constraint imposed by the positions of the pentagons of the layer ϵ in contact with the confining surface onto the layer δ make the corresponding buckyball structure impossible with 72 molecules. Therefore, the δ layer has a frustrated geometry that would induce frequent transitions between the different frustrated structures that are possible under the mentioned conditions. However, the $\{H_2O\}_{20}$ in γ seems to be much more stable, since the position and number of molecules are not significantly changed with the increase of the temperature.

After the analysis of the structure, we center our attention on the overall dynamics of the water layers found in this POM at $T = 298$ K. To that purpose, we divide the cavity into 10 concentric shells that roughly correspond to the peaks and the almost empty regions between these peaks. By practical purposes, the shells do not have a uniform width and are defined by a set of distances R_i corresponding to the external radius of the ith layer. If d is the distance between the center of the POM and the oxygen of a given water molecule, then it belongs to shell i if $R_{i-1} < d < R_i$ for $i = 1, \ldots, 10$ with $R_0 = 0$. The radii R_i defining the shell structure are given in Table 2.1. According to this division of the POM's cavity into shells, the water layers are inside shells $i = 2, 4, 6, 7$,and 9 which correspond to the peaks β, γ, δ_A, δ_B, and ϵ, respectively. Notice that we have considered peaks δ_A and δ_B in shells 6 and 7 due to the fact that the analysis of the dynamics between these two shells gives some information about the motion of the water molecules inside the same layer. In turn, shells $i = 1, 3, 5, 8$, and 10 correspond to the valleys between the peaks, i.e., to the empty space between the layers.

Table 2.1: Radii R_i of Concentrical Shells Dividing the Interior of the POM.

layer	1	2	3	4	5	6	7	8	9	10
R_i (Å)	1.40	2.60	3.73	5.01	6.07	6.91	7.80	9.56	10.54	12.1

Let $n_i(t)$ be the number of water molecules in the shell i at time t and $\bar{n}_i$, the equilibrium average of this quantity. Then,

$$\Delta n_i(t) = n_i(t) - \bar{n}_i \tag{2.1}$$

corresponds to the fluctuation in the occupation number of molecules within the shell with respect to its average.

Our first analysis corresponds to the evaluation of the equal-time correlation between the fluctuations in the number of molecules between pairs of layers, that is,

$$S_{ij} \equiv \langle \Delta n_i(t) \cdot \Delta n_j(t) \rangle \qquad (i, j = 1, \ldots, 10) \tag{2.2}$$

where S_{ij} is the ij element of the covariance matrix S and angular brackets stand for an equilibrium average. The principal component analysis[57] of S indicates the preferred modes of variation of the occupation number of the shells. From the 10×10 S matrix, one obtains 10 eigenvectors $\vec{a}_i$ and the corresponding eigenvalues λ_i. The main idea is to order the eigenvectors by the magnitude of its eigenvalue and take the first ones, as they retain most of the variation present in system. In this study, we consider the first n^* eigenvectors provided that $(\sum_{i=1}^{n^*} \lambda_i)/(\sum_{j=1}^{10} \lambda_j) \geq 0.9$, which corresponds to the set of normal modes that gather the 90% of the fluctuation in the occupation number in this shell structure. With this analysis, we can identify the dominant modes of the dynamics of the system.

The time evolution of the fluctuations in the occupation number is studied by means of the time correlation function $C_{ij}(t)$, defined as

$$C_{ij}(t) = \langle \Delta n_i(0) \cdot \Delta n_j(t) \rangle \qquad (i, j = 1, \ldots, 10) \tag{2.3}$$

where angular brackets stand for equilibrium average. The Fourier transform of $C_{ij}(t)$ is of particular interest, namely, $C_{ij}(\nu)$, defined as

$$C_{ij}(\nu) \equiv \int_{-\infty}^{\infty} dt\, C_{ij}(t) e^{-2\pi i \nu t} \tag{2.4}$$

The power spectrum of $C_{ij}(\nu)$ is by definition

$$P_{ij}(\nu) = |C_{ij}(\nu)|^2 \tag{2.5}$$

The behavior of the power spectrum, $P_{ij}(\nu)$, permits to analyze the nature of the events that cause the relaxation in the distortions of a given layer. The behavior of $P_{ij}(\nu)$ at low frequency reflects the complex dynamics of the hydrogen bonding network in this confined system.

2.2.2 Hydrogen Bonds

Hydrogen bonding between water molecules is analyzed to see how the confinement affects the HB network compared to bulk water. However, the definition of a hydrogen bond depends on the criterion used to discriminate a bonded from a nonbonded state, while the electrostatic potential responsible for that strong and very directional attraction is continuous. Therefore, the analysis of hydrogen bonding is always qualitative due to the fact that different criteria can lead to different results. In this work, we have used the geometrical criterion widely present in the literature.[138] In this case, two water molecules are hydrogen bonded when the following conditions are satisfied at the same time:

(a) The distance r_{OO} between the oxygens of both molecules is lower than R^c_{OO}.

(b) The distance r_{OH} between the oxygen which accepts the HB and the hydrogen which donates the HB is lower than R^c_{OH}.

(c) The bond angle ϕ between the intramolecular O-H direction of the donor and the O-O direction is less than ϕ_c.

The distances $R^c_{\mathrm{OO}} = 3.6$ Å and $R^c_{\mathrm{OH}} = 2.4$ Å are taken as the first minimum positions of the radial distribution functions $g_{\mathrm{OO}}(r)$ and $g_{\mathrm{OH}}(r)$ of bulk water at ambient conditions. The adopted angular cutoff is $\phi_c = 30^{\mathrm{o}}$.

The dynamics of the HB network is studied from the relaxation of the HB correlation function $C_{\mathrm{HB}}(t)$, defined as[139]

$$C_{\mathrm{HB}}(t) = \langle \eta_{ij}(0)\eta_{ij}(t)\rangle \tag{2.6}$$

where $\eta_{ij}(t) = 1$ if oxygens i and j form a HB at time t and $\eta_{ij}(t) = 0$ otherwise. Only ij pairs hydrogen bonded at $t = 0$ are included in the statistics. We can furthermore analyze the inter- and intralayer hydrogen bonding by restricting the average to ij pairs initially belonging to different layers or to the same layer, respectively.

2.2.3 Infrared Spectroscopy

Aiming at comparing the behavior of our system to the analogous reverse micelles and to the experimental data reported for the latter,[124] we introduce here the predicted infrared absorption spectrum of a virtual OD stretch of HOD, where D stands for deuterium, that in the experiment would replace a water hydrogen. As in ref [16], it is expected that the changing mass of the deuterium does not significantly affect the dynamics that we have calculated for H_2O molecules. From MD simulations, using the linear response formalism in conjunction with the mixed quantum/classical approximation, the absorption line shape $I(\omega)$ is given by[140]

$$I(\omega) \sim \mathrm{Re} \int_0^\infty dt e^{i\omega t} \langle \vec{\mu}_{10}(0) \cdot \vec{\mu}_{10}(t) \mathrm{e}^{-i\int_0^t d\tau \omega_{10}(\tau)} \rangle \mathrm{e}^{-t/2T_{10}} \tag{2.7}$$

where $\vec{\mu}_{10}(t)$ is the transition dipole moment for the OD stretch fundamental at time t, $\omega_{10}(t)$ is the fluctuating transition frequency, and T_{10} is the vibrational lifetime. We use the values given in ref [16] which are $T_{10} = 1.8$ ps,[141] and the transition dipole moment $\vec{\mu}_{10}$ is given by

$$\vec{\mu}_{10} = \vec{\mu}' x_{10} \hat{u} \tag{2.8}$$

Table 2.2: Empirical Relationship between the Local Electrostatic Field and the Parameters of eq 2.7. ω_{10} is given in (cm^{-1}), $\mu^{'}$ is normalized by its gas-phase value $\mu^{'}_{g}$, and x_{10} is given in Å. In these expressions, E stands for the local electric field on the position of the hydrogen (virtual D) atom, and is given in au.[142]

$$\begin{aligned}
&\omega_{10} = 2762.6 - 3640.8E - 56641E^2 \\
&x_{10} = 0.0880 - 1.105 \times 10^{-5}\omega_{10} \\
&\mu^{'}/\mu^{'}_{g} = 0.71116 + 75.591E
\end{aligned}$$

where $\vec{\mu}^{'}$ is the dipole derivative, x_{10} is the matrix element of the OD stretch coordinate between the ground and first excited vibrational states, and $\hat{u}$ stands for the unit vector along the OD bond. The values of the parameters in eq 2.7 depend on the local electric field on the position of the hydrogen atom and are described in Table 2.2.

2.2.4 Local Orientation of Water Molecules

To study the orientation of water molecules at each layer, we compute the probability distribution function of the relative angle θ_n^{α} of a given vector $\vec{\alpha}$, defined on the molecule, with respect to a normal vector $\vec{n}$ pointing outward from the center of the cavity, i.e.,

$$P_i(\cos\theta_n^{\alpha}) = \langle \delta(\cos\theta_n^{\alpha} - \cos\theta_n^{\alpha}(k)) \rangle \tag{2.9}$$

where $\theta_n^{\alpha}(k)$ is that angle for a given molecule k in the ith layer. In this work, we have considered α as being each of the three vectors, namely, $\vec{r}_{\mu}$, defined as the vector pointing along the water dipole moment, but in the opposite sense, $\vec{r}_{\mathrm{OH}}$, and $\vec{r}_{\mathrm{HH}}$, as the vectors along the O-H and H-H directions, respectively (see Figure 2.4). Numerically, the probability distribution is calculated via a histogram as follows

$$P_i(\cos\theta_n^{\alpha})\,\Delta \simeq \frac{1}{M}\sum_{M}\left(\frac{1}{N_i}n_i(\cos\theta_n^{\alpha})\right) \tag{2.10}$$

where M is the number of samples taken to perform the equilibrium average from the simulation, $n_i(\cos\theta_n^{\alpha})$ is the number of molecules in the ith layer satisfying

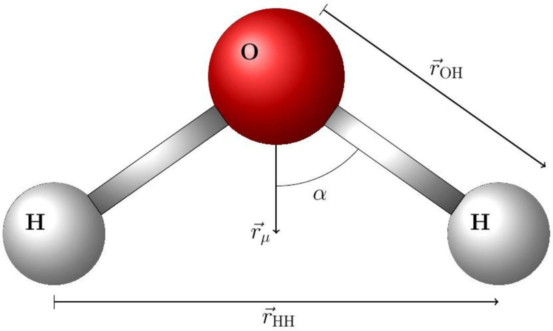

Figure 2.4: Vectors defined along selected molecular directions. $2\alpha = 109.47^{\mathrm{o}}$ for the SPC/E water molecule.

that $\cos\theta_n^\alpha - \Delta/2 \leq \cos\theta_n^\alpha(k) \leq \cos\theta_n^\alpha + \Delta/2$, where Δ is the bin size to construct the histogram and N_i is the total number of molecules in the layer. The cosines of the angle $\theta_n^\alpha(k)$ are calculated from $\cos\theta_n^\alpha(k) = \frac{\vec{n}(k)\cdot\vec{r}_\alpha(k)}{|\vec{n}(k)||\vec{r}_\alpha(k)|}$.

2.2.5 Rotational Dynamics

The orientational dynamics of water inside $\mathrm{Mo}_{132}(\mathrm{SO}_4)$ has been studied by means of reorientational correlation functions $C_{l,\alpha}(t)$ defined as

$$C_{l,\alpha}(t) = \langle P_l(\vec{u}_\alpha(t)\cdot\vec{u}_\alpha(0))\rangle \tag{2.11}$$

where P_l is the lth Legendre polynomial and $\vec{u}_\alpha$ is a unit vector along the molecular direction given by $\vec{\alpha}$.[42] Here, only $C_{2,\mathrm{OH}}(t)$ is considered, as its value can be compared to rotational anisotropy decay measured by polarization-resolved pump-probe experiments.[16,124]

2.2.6 Tetrahedral parameter

To analyze the degree of tetrahedral order around a given molecule it is customary to introduce the so-called orientational parameter q, defined as,[144]

$$q = 1 - \frac{3}{8} \sum_{j=1}^{3} \sum_{k=j+1}^{4} \left(\cos \psi_{jk} + \frac{1}{3} \right)^2 \tag{2.12}$$

where ψ_{jk} is the angle formed by the directions joining the oxygen of the central molecule to two of the oxygens, j and k say, out of the four nearest neighbors. Then, the mean value of q, $\langle q \rangle$, equals 1 for a perfect tetrahedral arrangement and 0 for a random distribution of molecules (ideal gas). Notice that this structural order parameter is defined independently of any particular reference system attached to the molecule due to the fact that it was conceived to also give a measure for the existence of this kind of tetrahedral structures in isotropic molecules[144] like those described by Lennard-Jones potentials. The measure of q in the water layers inside the POM gives us an excellent measure of the distortion of the hydrogen bonding network inside the cavity as compared to that of bulk water under the same thermodynamic conditions.

2.3 Computational Details

MD simulations of water inside the $\mathrm{Mo}_{132}(\mathrm{SO}_4)$ capsule, at a temperature of 298 K and a pressure of 1 atm, have been carried out. Simulations have been performed using the DLPOLY v2.19 code, developed at Daresbury Laboratory.[31] Both water and POM have been modeled as rigid molecules. Lennard-Jones potentials are used to describe the dispersion forces in addition to Coulombic contributions due to partial charges at specific locations. For water molecules, we have considered the SPC/E model.[26] The main properties that we are aiming at calculating depend on the collective properties of the system, and therefore, it is not expected that fine details of the potential, like vibrational motion, flexibility, and polarizability, strongly influence our results. Then, the use of rigid models for water permits an enormous computational economy. However, to check the independence of the results with regard to the model used, we have performed a series of simulations with the TIP4P model[98] to verify that, effectively, the results that we present do not depend on the details of the model used. As far as the POM is concerned, the LJ parameters are those given in ref [20] which are based on the criteria given in ref [145] and have been used by us and other authors to model rather complex polyoxometalate systems as well.[146–149] For the crossed LJ interactions, we have used the Lorentz-Berthelot mixing rules: $\sigma_{ij} = \frac{1}{2}(\sigma_{ii} + \sigma_{jj})$, $\epsilon_{ij} = \sqrt{\epsilon_{ii}\epsilon_{jj}}$. Partial charges of the POM used in this paper have been determined by using the Qeq method[150] and are reported in ref [20]. In the simulation, the capacities of DLPOLY have been exploited by considering that electrostatic interactions are accounted for by using the Ewald summation technique,[2] with a convergence parameter of 0.210 and considering a maximum of 6 wave vectors in each direction. The Verlet leapfrog algorithm[3] was used to integrate the equations of motion with a time step of 1 fs and a cutoff of 18.5 Å. In order to optimize the CPU usage, we have used a Verlet neighbor list[2] with cutoff radius of 19.5 Å. The rigid body rotational motion is handled under the leapfrog scheme with Fincham's implicit quaternion algorithm,[35] with a tolerance of 10^{-4}. All simulations have been performed with cubic periodic boundary conditions. The volume of the box is equal to 70 × 70 × 70 Å^3. The number of water molecules inside the POM is 172. No external solvent has been considered. Both equilibration and production runs have been performed in the NVT ensemble, using Nosé-Hoover thermostat[39] to keep the temperature fixed with a relaxation time τ_T equal to 1 fs. The run lengths are 250 ps for equilibration runs and 5 ns for production runs. Positions and velocities are stored each 10 time steps.

DLPOLY output files are analyzed with a post-treatment constructed to determine the correlation functions and averages required for our analysis. To compute the $g(r)$, the cavity of the POM is divided into concentrical shells of width 0.011 Å. For the diagonalization of the covariance matrix $\langle \Delta n_i(t) \Delta n_j(t) \rangle$, we use the GNU Octave 3.0.0 program. For the HB analysis, we have also performed a MD simulation of bulk water at $T = 298$ K to compare the obtained results with those calculated for water inside the POM. Probability distributions $P(\cos\theta_n^\alpha)$ are computed by dividing the interval of possible values of $\cos\theta_n^\alpha$, $[-1, 1]$, into 200 shells of width 0.01.

2.4 Results

2.4.1 Local Water Structure

We have calculated the statistics of the hydrogen bonding in each shell, to compare the structure of confined water to that of bulk water. In 2.5a, we show the average number of hydrogen bonds per molecule, $\langle N_{\mathrm{HB}} \rangle$, for each shell. Furthermore, in Figure 2.5b-d, we indicate the histograms of the number of HB per molecule in the different shells, also in comparison with the corresponding histogram of bulk water at the same thermodynamic conditions.

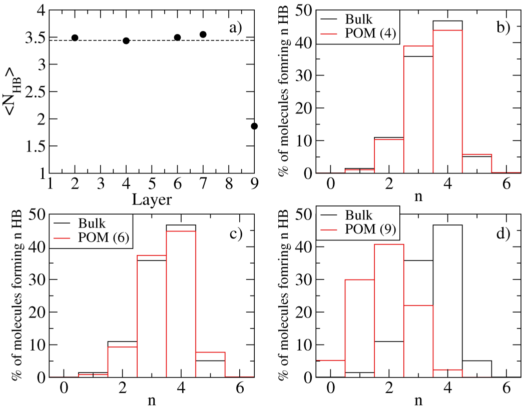

Figure 2.5: (a) Mean number of HB per water molecule $\langle N_{\mathrm{HB}} \rangle$ in the different layers. The dotted line corresponds to the value for bulk water at the same thermodynamic conditions. (b-d) Histograms of the number of molecules forming n HB in layer 4 (b), 6 (c), and 9 (d) as compared to bulk water.

We observe that the histogram as well as $\langle N_{\mathrm{HB}} \rangle$ in the inner shells does not significantly differ from what we observe in bulk water, despite the layered structure displayed by the system. In particular, for shell 4, the more significant trend is a slight reduction of the average number of particles with four HB in favor of particles with three HB. The less frequent cases of particles with two and five HB remain statistically the same as in bulk water. For shell 6, the main trend seems to be an increase of the number of HB by displacing particles with 4 HB into 5 as well as from 2 into 3. For shell 7 (not shown), we see, however, an opposite tendency. In any case, as far as the number of HB is concerned, no strong significant variation with respect to bulk water is observed in the cavity. This fact, moreover, also indicates that the layers are significantly connected through HB bridges. Finally, in Figure 2.5d, we observe a strong reduction of $\langle N_{\mathrm{HB}} \rangle$, even shifting the histogram one position to the left to account for the bonding formed by the water molecule and the metal moieties of the POM wall. Therefore, we can conclude that the geometry of the inner surface of the POM hinders for that layer the formation of structures that would maximize $\langle N_{\mathrm{HB}}\rangle$. This kind of behavior has been observed in other systems. [119,130]

An analogous analysis is done through the tetrahedral order parameter q. For this variable, the effect of the confinement is more noticeable (see 2.6). For shells 2, 4, and 6, its value is significantly lower than that observed in bulk water, while $\langle N_{\mathrm{HB}}\rangle$ did not reflect a significant difference. This result together with the previous analysis suggests that the layered structure of this confined water is reached by deforming the HB network more than breaking a significant number of HB. The increase of the value of q in shell 7 is difficult to explain; in addition, it also agrees with a larger $\langle N_{\mathrm{HB}}\rangle$ which we think is attributed to the combination of the stronger binding of the outer water layer with the appropriate geometric conditions to form stable tetrahedral structures. For the ninth shell, an explanation for the decrease of the tetrahedral order goes along the same lines as we have sketched for $\langle N_{\mathrm{HB}}\rangle$.

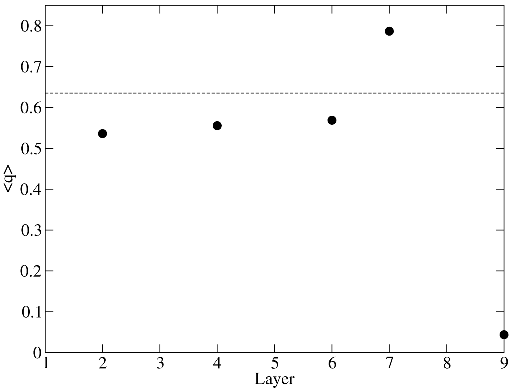

Figure 2.6: Mean tetrahedral parameter $\langle q\rangle$ for the different layers. The dotted line corresponds to that calculated for bulk water under the same thermodynamic conditions.

The dynamics of the hydrogen bonds also reveals interesting features. In Figure 2.7a, the results for $C_{\mathrm{HB}}(t)$ (cf. eq 2.6) restricted to HB between water molecules of the same layer are reported in comparison with the results for bulk water. Unlike the static properties analyzed above, the correlation functions significantly deviate from the bulk values. In particular, we observe, at long time, the general trend that the more internal the layer, the closer to the bulk value is found. Furthermore, inside the POM, the correlations are maintained for significantly longer times than in the bulk. This can be understood by recalling that the definition of the correlation function accounts for the breaking and reforming of HBs between a given pair of water molecules. Therefore, since confinement forces the particles to keep their relative positions much longer than in bulk systems, due to the hindrances of the particle diffusion, it is then expected that the correlation lasts longer due to the later fact. This explains why for the outer, more immobile, layer 9, the correlation at 50 ps is larger than that of layer 6-7, and that the value for layer 4 is closer to the bulk. At short times, less than 5 ps, the sharp decay of the correlation of layers 9 and 4 can be associated with the more frequent breakage and reforming of HBs than in the bulk, due to the geometrical constraint of the water molecules to form the layer. In agreement with the tetrahedral order parameter given in Figure 2.6, the less constrained layer is the 7th, which corresponds to the slowest decay of $C_{\mathrm{HB}}(t)$ at short times.

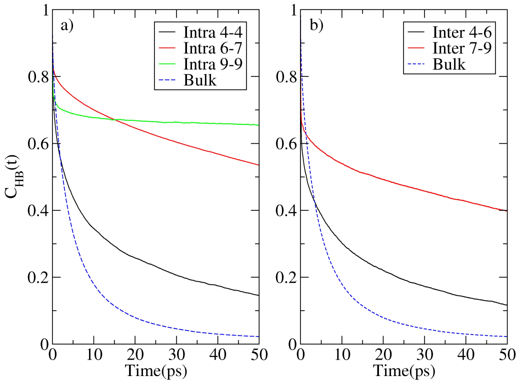

Figure 2.7: HB correlation functions $C_{\mathrm{HB}}(t)$ for intralayer HB (a) and interlayer HB (b).

The decay of the correlation of the HBs connecting different neighboring layers is displayed in Figure 2.7b. The general trend of these correlation functions is the same as that for the intralayer case, for both long and short times as well. However, the more important conclusion to be drawn is that the HB bridges between layers are less correlated than the HBs keeping the structure of the layer together. Therefore, we can conclude that (i) the layers in this system are rather stable structures kept by a bidimensional HB network involving three HBs and

(ii) the remaining HB donor/acceptor for every water molecule establishes bridges between layers, whose correlation dies out slightly faster than the former. Finally, these correlations, in essence, measure the persistence of the water network in the system. With the time window analyzed, we can not define a correlation time which would require simulations long enough for the correlation functions to die out. In our case, these times are longer than the overall simulation length.

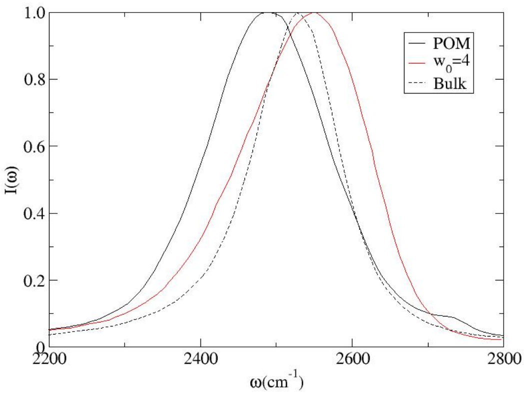

Figure 2.8: Line shapes of the OD stretch for water encapsulated in $Mo_{132}(SO_4)$ (black), $w_0 = 4$ RM (red), and bulk water (dashed) as obtained from simulation data and eq 2.7.

Finally, for completeness, we have computed the predicted line shape for the OD stretch as described in eq 2.7. In Figure 2.8, we compare our predicted spectrum to the bulk value and the simulated result for $w_0 = 4$ RM, the latter given in ref [16]. On one hand, our predicted curve for bulk water perfectly agrees with the same curve given in ref [16] and the experiments,[124] indicating the consistency of our results. On the other hand, our results for the confined water in the $Mo_{132}(SO_4)$ are surprisingly shifted to the red instead of the shift to the blue seen in RMs of similar size. This fact is due, in our case, to the unbalanced 72 negative charges that displace the position of the peak to the red, since the local electric field is larger than in a neutral system. Therefore, our result cannot be compared to the analogous $w_0 = 4$ RM results. Instead, it will be interesting comparing the shift of the $I(\omega)$ line shape peak when different polyoxometalates are used, and then to compare whether the effect of the confinement shifts the peak in an analogous way as in RMs. Much work has to be done before sensible predictions of the line shape, taking into account the experimental setup of a system with water encapsulated in a POM, can be done.

2.4.2 Covariance Matrix

The analysis of the covariance matrix S is done for the 10 shells defined in Table 2.1. The results of the diagonalization of the matrix give the principal modes of fluctuation of the occupation number in each shell. In Table 2.3, we present the four eigenvectors $\vec{a}_i$ selected by the criterion that together they describe more than 90% of the fluctuation observed. The associated eigenvalues, λ_i, and the fractions of the total variance of Δn in the direction of the eigenvector $\vec{a}_i$, namely f_i, are also presented in Table 2.4.

Table 2.3: eigenvectors $\vec{a}_i$ resulting from the diagonalization of S. Main components of each vector are shown in boldface.

Eigenvector Component j	a_{1j}	a_{2j}	a_{3j}	a_{4j}
1	0.000	0.021	0.017	-0.036
2	0.003	-0.091	-0.079	0.195
3	-0.033	0.273	0.164	**-0.558**
4	0.062	**-0.543**	-0.287	**0.415**
5	-0.188	**0.646**	0.098	**0.450**
6	**0.663**	-0.181	0.295	**-0.242**
7	**-0.650**	-0.285	-0.164	**-0.390**
8	0.277	0.283	**-0.621**	-0.065
9	-0.144	-0.142	**0.611**	0.244
10	0.010	0.009	-0.033	-0.016

According to Table 2.3, the first eigenvector $\vec{a}_1$ shows that the main fluctuation mode occurs by the transfer of water molecules between the peak δ_A and the peak δ_B lying in shells 6 and 7, respectively. This fact is seen by the opposite sign but similar value of the two largest components of $\vec{a}_1$, that is a_{16} and a_{17}, which means that an increase of Δn_7 is mainly due to a decrease of Δn_6 and vice versa. In this particular case, we recall that layer 6 and 7 are part of the same structure that is organized in two different levels, and which show a certain degree of

Table 2.4: Eigenvalues λ associated to eigenvectors $\vec{a}_i$, and fraction of the total variance of Δn in the direction of $\vec{a}_i$; f_i.

eigenvector	λ	f
$\vec{a}_1$	13.81	0.40
$\vec{a}_2$	9.81	0.286
$\vec{a}_3$	5.28	0.154
$\vec{a}_4$	2.46	0.072

frustration, due to the fact that its natural conformation contains 80 molecules, instead of 72, according to section 2.2.1. Therefore, the fact that this layer is frustrated indicates that frequent transitions between equivalent structures may often occur. The analysis of the components of the second eigenvector suggests that this mode of fluctuation is dominated by deformation of the structure of layer 4 that partially enters the region defined as shell 5. As we will see in section 2.4.3, such a mode of motion corresponds to fast deformation of the structure more than to the creation of long-lived HB or metastable states between neighboring layers. The analysis of the components of the third eigenvector reveals similar conclusions involving valley layer 8 and peak layer 9. Finally, the last eigenvector, $\vec{a}_4$ has a much smaller f_4, indicating that this mode of motion is much less important than the previously analyzed one. It is interesting, however, to observe that it describes a somehow more collective motion involving correlated simultaneous fluctuations increasing the number of molecules in shells 4 and 5 from shells 3, 6, and 7.

Switches of water molecules as well as bridges between layers seem to be rare events as compared to the frequency of the overall deformation of the structure forming the layer. To discern the validity of this statement, we computed the distance $d(t)$ of a tagged molecule to the center of the cavity. In Figure 2.9a, we record the position of a water molecule, initially located in layer 9, next to the inner side of the cavity. As we know, this is a rather stable layer due to the strong interaction of water molecules with the surface moieties of the POM. However, we see short-lived excursions of the molecule into the eighth valley shell and even to the seventh peak layer. In all cases, these fluctuations are very short-lived in the time window that we have explored. Figure 2.9b is much more illustrative, since, together with the same kind of short-lived fluctuations, we observe events in which a water molecule of the seventh layer occupies the sixth layer for a significant period of time to later return into the original layer. For the pair 6-7, we recall that they form a single HB-connected structure. Nevertheless, in this figure, we also observe excursions in which a water of the sixth layer penetrates shell 4 for a period of about hundreds of picoseconds, to return back to the original layer. This fact, together with the previous analysis, indicates that the exchange of water molecules between layers is difficult due to the stable structure that they form but HB bridges between layers can occur and last quite a long time. We believe that these kinds of rare but long-lived events are those described by $\vec{a}_4$, implying that the transient HB bridges formed shall deform adjacent layers 4, 6, and 7 in the way described by this eigenvector. Therefore, we can infer (see also section 2.4.4) that the layers deform at a given point due to the formation of a HB bond between the layers without a significant distortion of the local structure as to accommodate a new molecule, giving the eventual return of the molecule to the original layer. We have observed, however, that, for a molecule to exchange its layer, a switch has to simultaneously occur; otherwise, the molecule is rejected back to its original layer.

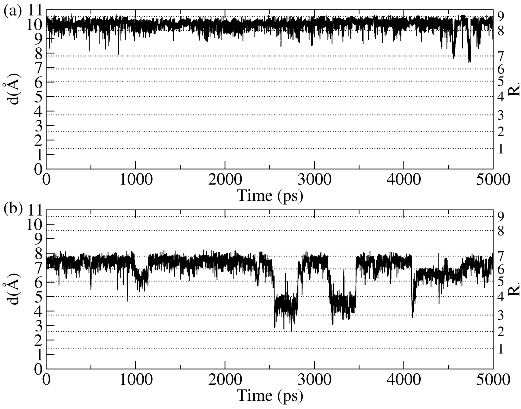

Figure 2.9: Distance $d(t)$ from the center of the POM of two water molecules (a and b). Radii R_i for each layer are also shown (dashed line).

2.4.3 Dynamic Correlation Functions

The dynamic correlation functions $C_{ij}(t)$, defined in eq 2.3, have been calculated for $i = j$, namely, the autocorrelation function of the ith layer, as well as for $j = i + 1$, or the cross-correlation function between a peak layer and the neighboring valley layer. In Figure 2.10, we plot the autocorrelation functions

$C_{ii}(t)$ for shells $i = 4, 6, 7$, and 9, where we observe that, after a fast decrease of the correlation for short times, all curves present an oscillation around 0.5 ps. This behavior is indicative of a natural mode of vibration of the overall layers. In the second place, the value of $C_{ii}(0)$ corresponds to our interpretation of the eigenmode of the covariance matrix S, indicating that, for example, the more relevant motion is the fluctuation between layers 6 and 7; then, between layers 4 and 5, and so on. In the third place, after the oscillation, the behavior of $C_{ii}(t)$ looks like a power law decay that we will discuss later on when analyzing the power spectrum.

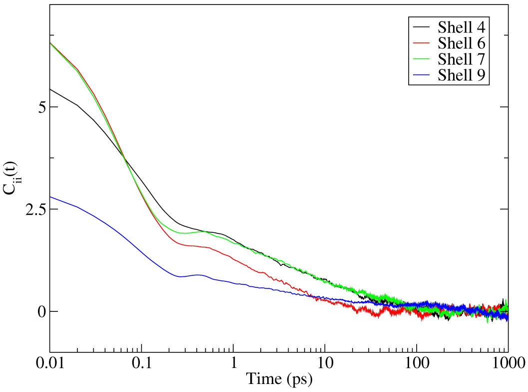

Figure 2.10: Autocorrelation function $C_{ii}(t)$ for shells $i = 4, 6, 7$, and 9.

The cross-correlation functions $C_{ij}(t)$ shown in Figure 2.11a reflect the same physical behavior that we have just discussed. The negative value of the correlation is in support of the statement that the measured dynamic behavior of the system is related to excursions of water molecules between peak and valley shells, that is between layers and the interstitial space between them. The cross-correlation function between shells 4 and 6, namely, $C_{46}(t)$, corresponding to cross-correlations between different structures, is shown in Figure 2.11b. The magnitude of this correlation is smaller than the autocorrelation functions, although it is still significant. First of all, it is positive at short times, due to the fact that the fluctuations of the structures affect each other. Nevertheless, it is very significant the negative value of the correlation occurring at a time of about 30 ps, that again can be related to the mode of motion described by $\vec{a}_4$, that is, that HB bridges are established between the structures deforming them in a correlated way, for a significantly long time. Finally, another aspect that reinforces the interpretation that we make of the long-time behavior of the system is given by the presence of a long-time tail of the correlation functions, that lasts up to about 100 ps before they practically vanish.

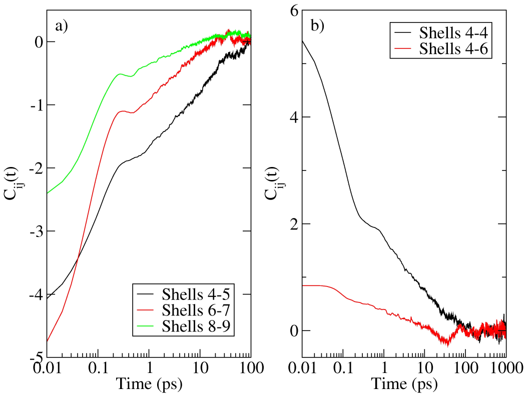

Figure 2.11: (a) Cross-correlation functions $C_{ij}(t)$. (b) Cross-correlation function $C_{46}(t)$ compared to autocorrelation function $C_{44}(t)$.

Power spectra, $P_{ij} = |C_{ij}(\nu)|^2$, defined in (eq 2.5), have also been calculated. The obtained spectra are presented in Figure 2.12 in log-log plot. All figures display a similar tendency, which can be summarized as follows. The curves present two distinct regions separated by a small bump at a frequency of about $\nu \approx 2$ ps^{-1}, which corresponds to a period of 0.5 ps. This is the time corresponding to the position of the observed oscillation at short times in $C_{ij}(t)$. With regard to our previous discussion, the more interesting region is that at frequencies smaller than 1 ps^{-1}, corresponding to the long-time behavior of the power spectra. In that region, we see that the power spectrum of $C_{ii}(\nu)$ approaches a power law of the form $P_{ii}(\nu) \sim \nu^{-\alpha_i}$. The obtained exponents α_i, for each shell i are given in 2.5. With these exponents being smaller than 2, this behavior corresponds to the so-called flickering noise or pink noise. The exponent α_i is approximately 0.75, for all layers, except for layer 2, taking into account the fact that the error bars strongly increase toward the inner, less populated, layers. The value of the exponent is very close to that reported in ref [134], obtained for the power spectrum of the potential energy fluctuations observed in bulk water under ambient conditions. Notice that a pure Brownian relaxation (e.g., diffusion at long times, $\langle\rho(\nu)\rho(0)\rangle = \langle\rho^2(0)\rangle/(-i\nu + Dk^2)$ where k is the wave vector and D, the diffusion coefficient of a Brownian particle) shows a plateau for the density-density correlation function for $\nu \ll Dk^2$. Hence, pink noise is usually regarded as the collective effect of processes with a cascade of different characteristic relaxation times. Although several explanations of the presence of pink noise in the dynamic properties of water have been conjectured,[134] the fact is that no clear explanation, neither prediction of the value of the exponent, has been given to date. Nevertheless, with regard to the characteristic time range where this phenomenon occurs, everything seems to indicate that it must be related to the processes regarding HB bridging between layers but also inside frustrated layers and, therefore, to the overall rearrangement of the HB network forming structures with similar free energies. The region $\nu > 2$ ps^{-1} reflects the short-time dynamics of the water molecules that has already been described.

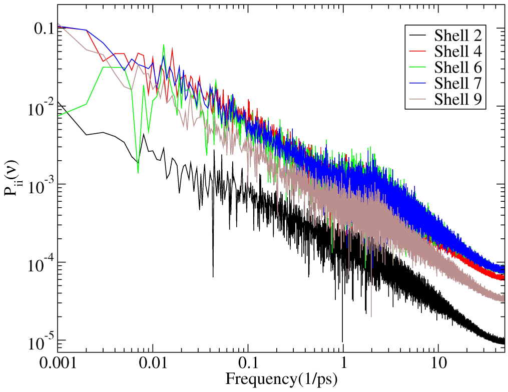

Figure 2.12: Power spectrum $P_{ii}(\nu)$. The local maximum is observed at $\nu = 2$ ps^{-1}.

Table 2.5: Obtained Fitted Exponents α_i for $\nu < 1$ ps^{-1}.

shell	2	4	6	7	9
α	0.60	0.76	0.72	0.80	0.77

To end this section, we have included the results for the correlation function of the total dipole moment of the layer

$$\vec{M}_i(t) = \sum_{k \in i} \vec{\mu}_k(t) \tag{2.13}$$

where $\vec{\mu}_k(t)$ stands for the actual dipole moment of particle k in layer i. The correlation function $C_{ii}^M(t) \equiv \langle \vec{M}_i(0) \cdot \vec{M}_i(t) \rangle$ can be related to infrared spectroscopy measurements.[15] This magnitude is vectorial, as compared to the scalar Δn, and therefore, its behavior reveals different aspects of the dynamics of the system. In 2.13 we show the power spectrum, $P_{ii}^M(\nu)$, for the four layers. As compared to Figure 2.12, the correlation function for the total dipole moment shows an analogous behavior, although the dispersion of the values is significantly lower than in the case of $P_{ii}(\nu)$. In Table 2.6, we indicate the exponent, α_i^M, of the curves, fitted in the range [0.02,2] ps^{-1}, where the long time collective behavior is expected. With respect to $P_{ii}(t)$, the exponents of $P_{ii}^M(t)$ are significantly larger and very closer to -1. However, the ordering of the exponents for every layer exactly coincides with that of $P_{ii}(t)$ (see Table 2.6). It is therefore clear that each layer has its characteristic way of relaxation that leaves its footprint on the observables.

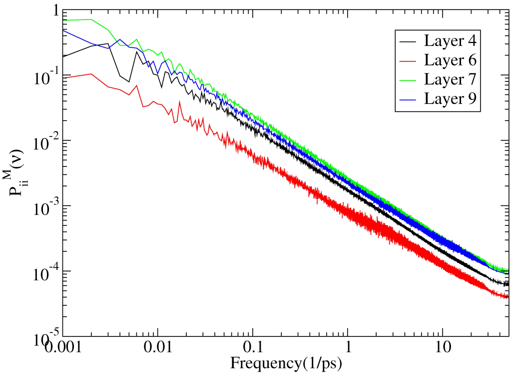

Figure 2.13: Power spectrum $P_{ii}^M(\nu)$.

Table 2.6: Obtained Fitted Exponents α_i^M for $\nu < 2$ ps^{-1}.

shell	4	6	7	9
α^M	0.94	0.87	0.97	0.95

2.4.4 Orientational Distributions

To obtain further insight into the possible causes of the long-time behavior of the correlation functions calculated so far, we have studied the distributions of angles θ_n^{OH}, θ_n^{HH}, and θ_n^{μ} for the layers 4, 6, 7, and 9. The distributions of $\mathrm{P}(\cos\theta_n^{\alpha})$ are shown in 2.14. We recall that α stands for OH, HH, and μ, the angles θ_n^{α} being defined in section 2.2.4. At the end of this section, we analyze the dynamics of the orientation of the water molecules through $C_{2,\mathrm{OH}}(t)$, which in addition can be compared to experimental data.

In the first place, we analyze the orientations of the water molecules in layer 7. In Figure 2.14a we see two peaks at $\cos\theta_n^{\mathrm{OH}} = 1$ ($\theta_n^{\mathrm{OH}} = 0$) and at $\cos\theta_n^{\mathrm{OH}} \approx -0.31$ ($\theta_n^{\mathrm{OH}} \approx 108.1^{\circ}$) which agree with having one OH bond parallel to the radial vector from the center of the POM, $\vec{n}$ ($\theta_n^{\mathrm{OH}} = 0$), and the other forming the corresponding angle imposed by the water geometry ($\theta_n^{\mathrm{OH}} = 109.47^{\circ}$). This result indicates that layer 7 is bound through HB to layer 9 which in turn is strongly bound to the inner surface of the POM (see Figure 2.15). This configuration can also be identified in Figure 2.14b, where two symmetric peaks are located at approximately $\cos\theta_n^{\mathrm{HH}} = \pm 0.815$, and also by the peak at $\cos\theta_n^{\mu} = 0.584$, in Figure 2.14c. Moreover, Figure 2.14b reveals the presence of a peak around 0, indicating a significant population of molecules that lie rather flat on the plane perpendicular to the radial vector. However, Figure 2.14c suggests through the peak at -0.54 that these molecules are slightly tilted approaching their hydrogens toward the sixth layer. We recall that layers 7 and 6 are part of the same structure; therefore, the latter water molecules make the connection between the pentagonal structure of layer 7 and the structure forming layer 6 (see Figures 2.2 and Figure 2.15).

Repeating the same analysis for layer 6, we see in Figure 2.14a two peaks at $\cos\theta_n^{\mathrm{OH}} = -1$ and at $\cos\theta_n^{\mathrm{OH}} \approx 0.31$. This result agrees with one of the OH bonds antiparallel to $\vec{n}$ and the other forming the angles imposed by the geometry of the water molecule. Again, we observe the phenomenon of layers connected through bridges of HB, as in this case, where layer 6 is bridged with layer 4. The absence of a peak in $\cos\theta_n^{\mathrm{OH}} = 1$ also indicates that no bridges are formed between layer 6 and layer 9. This interpretation agrees with the peaks at $\cos_n^{\mathrm{HH}} = \pm 0.815$ in Figure 2.14b and the weak increase of $\mathrm{P}(\cos\theta_n^{\mu})$ around $\cos\theta_n^{\mu} \approx 0.5$ at Figure 2.14c. Similarly, as in the case of layer 7, the central peak at $\cos_n^{\mathrm{HH}} = 0$ in 2.14b suggests that for many particles this vector lies perpendicular to the normal. The plateau region between $\cos_n^{\mu} \approx -0.5$ and $\cos_n^{\mu} \approx 0.5$ in Figure 2.14c suggests that the connection between layers 7 and 6 is mostly due to the tilt of water molecules from layer 7 toward those of layer 6, since the later molecules are wandering between $\cos_n^{\mu} \approx -0.5$ and $\cos_n^{\mu} \approx 0.5$, which does not significantly correspond to similar tilt in molecules of layer 6. In general, layer 6 is less structured than layer 7 due to the lower height of peaks and depth of valleys in the figures analyzed.

With regard to layer 4, we see that the larger mobility of those molecules is reflected in the absence of significant peaks, as seen from Figure 2.14. However, Figure 2.14a reveals a certain tendency to form HB bridges between this layer and layer 6 according to the peaks analogous to those of layer 7. Finally, the orientation of layer 9 is strongly influenced by the presence of the surface moieties. The more interesting feature of these rather immobile water molecules is a certain tendency to form bridges with layer 7, which is the reason why layer 7 is so much structured.

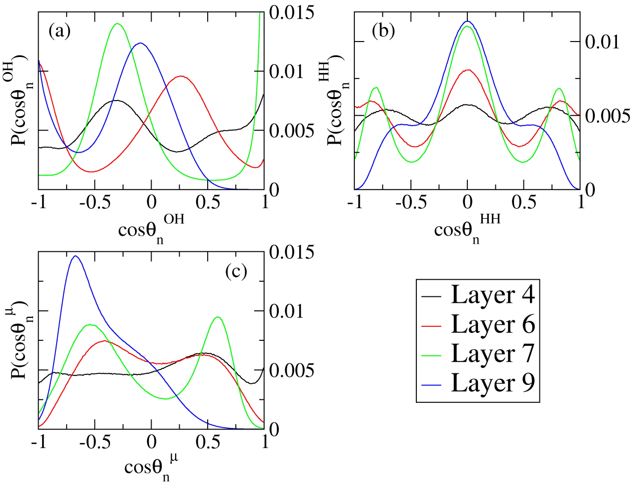

Figure 2.14: Orientational distributions $P(\cos\theta_n^{\mathrm{OH}})$ (a), $P(\cos\theta_n^{\mathrm{HH}})$ (b), and $P(\cos\theta_n^{\mu})$ (c) for different occupied layers.

The analysis of the orientational distributions indicates that the layers are not independent structures but that they are strongly connected through HB (see Figure 2.15). This fact explains why shells that we have identified as valleys are rather populated by hydrogen atoms that connect the layers. At the same time, the internal structure of the layer makes it very unlikely that the number of water molecules in the structure is changed. This contrasts with the relative facility with which HB rearrange inside the layer as well as among different layers. These two combined effects make it so that the transfer of water molecules between layers is a process that involves an almost simultaneous switch of two molecules from two neighboring layers after the bridging HB have prepared the scenario for this switch to occur. One of these events has been captured in 2.16 in which we see how the two tagged molecules exchange their positions in a transition that takes very short times.

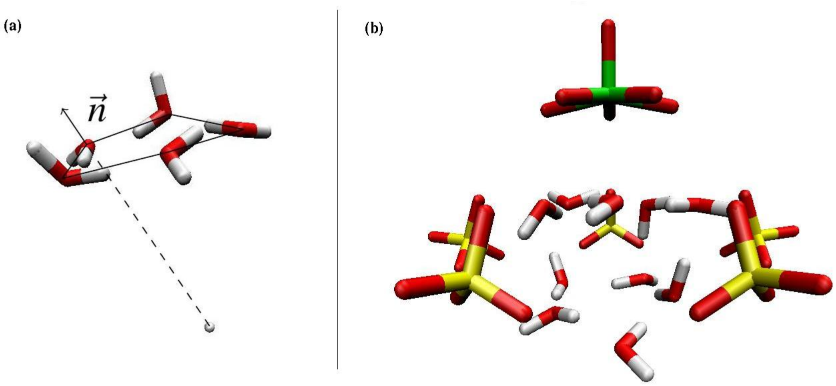

Figure 2.15: Example of an instantaneous conformation of the water molecules forming a pentagon in the layers close to the inner wall. (a) Water molecules in a pentagon in layer 7 (red oxygens, white hydrogens). Notice the tilt of the molecules that connect layers 6 and 7 as well as the hydrogen atoms bridging to layer 9. (b) The same pentagon of layer 7 is represented together with the solvation waters of layer 9. We have also plotted the sulfate molecules (yellow for sulfur) and the group MoO_6 (green for molybdenum). The structure of MoO_6 is responsible for the preferred pentagonal distribution of the sulfate groups, and strongly conditions the position and orientation of the water forming layer 9 as described in the text.

Our simulations with the TIP4P model are quantitatively the same for these orientational distribution functions as for the results obtained with the SPC/E model, used along the paper. The difference in the height of the peaks for the two water models in the radial distribution function, for example, is less than 5%, indicating that the results are fairly independent of the subtle details of the water models.

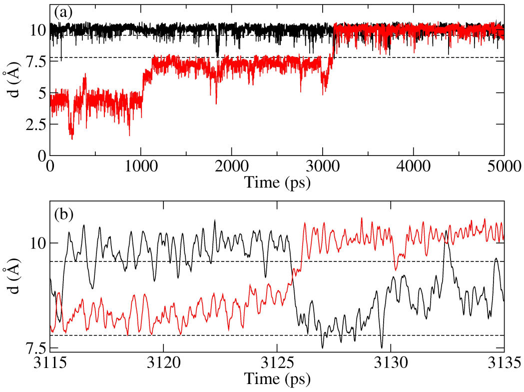

Figure 2.16: Distance $d(t)$ for two tagged water molecules (a). The red track shows at least three switches between layers. The zoomed figure (b) captures the switch between the red and black tagged molecules.

As far as the relaxation of the dynamics of the orientation is concerned, $C_{2,\mathrm{OH}}(t)$ measures the decay of the correlation of one OH vector for a molecule with respect to its orientation at $t = 0$. In Figure 2.17, we compare this decay in our system, with 172 water molecules, to the simulated results for a reverse micelle, $w_o = 4$, with 140 water molecules,[16] and the experimental data for a reverse micelle $w_o = 5$, with about 300 molecules.[124] We observe a slightly faster decay in the simulations of the $w_o = 4$ RM than our results with a similar number of water molecules enclosed. The difference between these two decays might be due to the fact that the POM capsule is rigid in our simulation while some degree of motion is allowed for the AOT surfactants in the simulations of ref [16]. It remains open the question why this correlation function for a larger RM has a slower decay, although the trends are quite similar.

In Figure 2.18, we compare our simulation results specific of individual layers with corresponding analyses for the $w_o = 4$ RM.[16] Our curves follow an analogous pattern as in Figure 2.7, which indicates that the hindered diffusion of the molecules permits the breaking and reformation of HBs that keep the orientation of the molecule strongly correlated to its initial value. Even we observe here that layer 6-7 with larger tetrahedral order keeps the orientational correlation above the more bound layer 9, although the trend at 5 ps suggests that, as for the HBs, they will cross over at longer times. It is interesting to notice that the results for the solvation layer of the $w_o = 4$ RM are analogous to

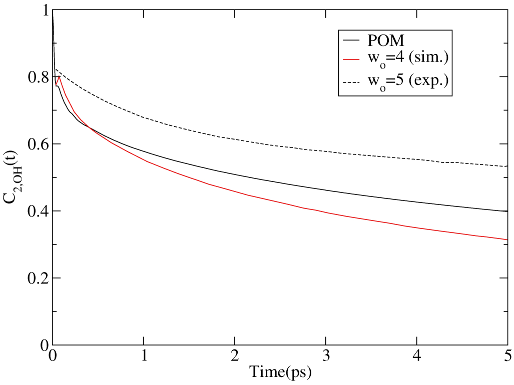

Figure 2.17: Comparison of calculated reorientational correlation function $C_{2,\mathrm{OH}}(t)$, for the $\mathrm{Mo}_{132}(\mathrm{SO}_4)$ capsule, with simulated results for a RM, $w_o = 4$, and experimental data for a RM, $w_o = 5$.

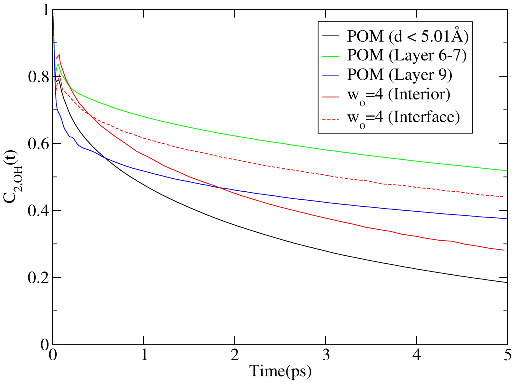

Figure 2.18: Reorientational correlation functions, $C_{2,\mathrm{OH}}(t)$, for water inside the $\mathrm{Mo}_{132}(\mathrm{SO}_4)$ capsule at different layers compared to simulated results for inner and interfacial water in RM, $w_o = 4$.

that of layer 9 while the data for the inner molecules of the former RM follow a similar trend as that for the core water molecules of our POM.

2.5 Conclusions

In this chapter we have analyzed the structure and dynamics of water molecules confined inside a $Mo_{132}(SO_4)$ cavity and compared to water confined in RMs.[16,124] We have stressed the fact that the three-dimensional HB network existing in bulk water is organized in layers to fulfill the constraint created by the inner side of the cavity. We have argued that these layered structures are created by the ability of the water molecules of creating three HB inside the layer. Therefore, each molecule inside one of these structures can still create a HB that will necessarily be with molecules of neighboring layers. We have thus suggested that these layered structures should belong to the buckyball family. Nevertheless, the position of the pentagons influenced by the metal moieties of the inner wall of the POM forces that the stable structures cannot have an arbitrary even number of hexagons. Furthermore, the difference between the experimentally observed structure and the simulation results at room temperature has been interpreted as caused by the increase of the free energy of the layer with the temperature which turns into the formation of a small drop in the center of the cavity and a decrease of the population of the more external layers. The analysis of HB statistics, the tetrahedral order parameter, as well as the orientational distribution functions all agree with that view. Our results are analogous to the observations made in the $w_0 = 4$ RMs.

The analysis of the dynamics of this peculiar system indicates that the main modes of motion are correlated fluctuations of the overall structures at short times. We have observed that the transfer of molecules among layers is rare and involves the switch of two water molecules. No metastable states involving the transient presence of one water molecule in the layer have been observed. Thus, only switches seem to be the mechanism by which water molecules diffuse inside the cavity. Correlation functions have permitted one also to observe the effects of the reorganization of the HB network, especially HB bridges between the structures. The long time tail in the correlations as well as the power law decay at low frequency of the power spectrum suggests, although it is not demonstrated, that the system evolves through an energy landscape with many minima with a certain energy distribution that would make the decay a process crossing multiple waiting times.

POMs as compared to RMs are more rigid structures that offer the possibility of enlarging the scope of the investigations done in water in confined environments. The particular system studied here has the peculiarity of forming several distinct layers of water that has no counterpart neither in RMs[14] nor in POMs where the SO_4 ligand is replaced by HCO_2.[20] It is important to mention the particular structure formed by layers 6 and 7, which has different features as compared to layers 4 and 9 corresponding to bound layer and more bulky water, respectively. Notice, for example, the slower decay of the occupation number as well as the total dipole moment and the higher tetrahedral parameter, which is larger than the bulk. Therefore, we believe that the *commensurability* of the natural structures of water with the geometry of the cavity has to play a relevant role that we have not explored yet.

The analysis of water inside small cavities may help in elucidating the exact mechanisms that produce the values of the exponents of this long time behavior.

Chapter 3

The effect of the ligand on the structure and the dynamics of encapsulated water inside Mo_{132} cavities

3.1 Introduction

The particular HB structures that water forms in a confining environment, such as in polyoxomolybdates, strongly depend on the details of the confining surface. As commented in section 2.1, the replacement of SO_4^{2-} ligands by HCO_2^- ligands on Mo_{132}(ligand) nanocapsules leads to different polyhedral-shaped water structures inside, as observed from X-ray data at $T = 188$ K.[20] Water molecules confined inside the $Mo_{132}(HCO_2)$ capsule are arranged in four concentric layers with radii of 4.02-4.08 Å, 6.62-6.72 Å, 7.66-7.78 Å, and 8.52-8.79 Å , which have primarily been interpreted as a $\{H_2O\}_{20}$ dodecahedron, a $\{H_2O\}_{20/2}$ dodecahedron, a $\{H_2O\}_{60}$ distorted rhombicosidodecahedron, and a $\{H_2O\}_{20/2}$ dodecahedron (see Figure 3.1) in ref [20]. An external water layer is also bound to the atoms of the POM internal surface. Although the three inner layers are located at similar positions as those of the water oxygens in the $Mo_{132}(SO_4)$ nanocapsule, for the $\{H_2O\}_{20}$ and $\{H_2O\}_{80}$ layers, the new layer at 8.52-8.79 Å suggests a quite different scenario.

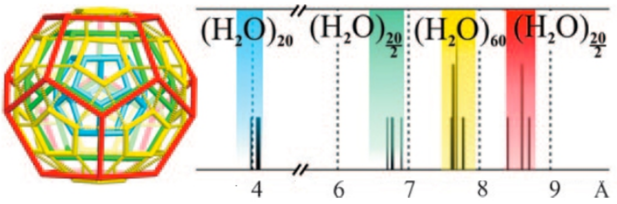

Figure 3.1: Structure of the water layers (water oxygens are at the vertices of the different polyhedra) inside $Mo_{132}(HCO_2)$ cavity (left figure), and distributions of water oxygens from the center of this capsule (right figure) as suggested in ref. [20] from experimental X-ray measurements at $T = 188$ K. From these data, a first $\{H_2O_{20}\}$ (blue) central dodecahedron is shown, then a $\{H_2O_{20/2}\}$ dodecahedron (green) which is followed by a distorted rhomicosidodecahedron $\{H_2O_{60}\}$ (yellow), and finally another $\{H_2O_{20/2}\}$ dodecahedron (red), not observed inside the $Mo_{132}(SO_4)$ capsule is formed between 8.52 Å, and 8.79 Å.

Molecular dynamics simulations of water inside $Mo_{132}(HCO_2)$ capsule, aiming at reproducing the experimental shells through the radial distribution function $g(r)$, show that only at low temperature ($T = 198$ K) the four inner peaks are reproduced.[20] However, when the temperature is increased to $T = 298$ K, the second and the third peaks at about 6.9 Å and 7.9 Å merge into a single peak. This effect has not been observed for the $Mo_{132}(SO_4)$ capsule where, even at ambient conditions, the structure of the water layers reflects the experimental X-ray peaks. The main differences between both nanocapsules are, on the one hand, the larger available volume inside the $Mo_{132}(HCO_2)$ for water molecules due to the smaller size of the formate ligands, compared to the sulfate ligands, and, on the other hand, the positive charge of the terminal hydrogen of the HCO_2 ligands and its lower vdw repulsion, as compared to the negatively charged oxygens of the SO_4 ligands. These differences suggest that, although the $Mo_{132}(HCO_2)$ capsule is more rigid than an AOT RM of similar size, the dynamic behavior of water in its interior will be closer to that of a RM than when the $Mo_{132}(SO_4)$ is considered.

In this chapter we study the effect of the HCO_2 ligand on the structure and dynamics of water encapsulated inside a Mo_{132} capsule at ambient conditions. The results for some of the properties are compared to our simulated results for water inside $Mo_{132}(SO_4)$ and to simulated results for bulk water. We are interested in understanding the causes of the difference in water structure observed in the X-ray measurements between both capsules, and how they affect the dynamics of water molecules at different regions inside the $Mo_{132}(HCO_2)$ capsule. Our results are also compared to experimental data and simulated results for water inside AOT RMs of similar size for orientational relaxation of the OH vector. The last comparison permits us to know whether the dynamics of water inside the $Mo_{132}(HCO_2)$ is close to that observed inside RMs and to provide measurable data to be experimentally tested.

3.2 Fundamentals

In the present study, we have calculated several of the properties already defined in the previous chapter. In the first part of the results section, which accounts for structural properties, we calculate the radial distribution function as done in Section 2.2.1. To give a measure of the spatial distribution of water oxygens inside both the $Mo_{132}(SO_4)$, and the $Mo_{132}(HCO_2)$ plots, we have also calculated the spatial distribution function, SDF. In this case, the simulation box is divided into cubes of equal volume called *voxels*, and the number of water oxygens in each cube is counted and, then, divided by the total number of water oxygens and timesteps used for the calculation. The same measure for the $Mo_{132}(SO_4)$

capsule system was already calculated in ref [20]. However, we recalculate it with from simulated data to compare the results with those calculated for the $Mo_{132}(HCO_2)$ capsule. We have also calculated the statistics of the hydrogen bonding at different distances from the center of the $Mo_{132}(HCO_2)$ capsule using the geometrical criterion given in Section 2.2.2. For the dynamics of water, we have studied the reorientation of the OH vector through the correlation function $C_{2,\mathrm{OH}}(t)$ as defined in Section 2.2.5.

Translational diffusion has been studied by means of the mean-squared displacement, MSD, defined as,

$$\mathrm{MSD}(t) = \langle |\vec{r}_{\mathrm{CM}}(t) - \vec{r}_{\mathrm{CM}}(0)|^2 \rangle \tag{3.1}$$

where $\vec{r}_{\mathrm{CM}}$ is the position of the center of mass of a water molecule. The MSD is directly related to the self-diffusion coefficient D_{self}, giving the diffusion of a labelled species among identical solvent molecules, by the following equation[2]

$$D_{\mathrm{self}} = \frac{1}{6} \lim_{t \to \infty} \frac{\partial \langle |\vec{r}_{\mathrm{CM}}(t) - \vec{r}_{\mathrm{CM}}(0)|^2 \rangle}{\partial t} \tag{3.2}$$

As water molecules are confined inside the Mo_{132} cavities, they can not travel distances larger than the diameter of the accessible sphere inside the POM. Then, strictly speaking, a diffusion coefficient can not be obtained from eq 3.2 at $t \to \infty$, and we use directly the MSD for finite times, to obtain an estimate of the diffusivity inside the POMs.

3.3 Computational details

MD simulations of water inside the $Mo_{132}(HCO_2)$ capsule, at a temperature of 298 K, and a pressure of 1 atm, have been carried out. To prevent water molecules to diffuse outside the POM, guanidinium counterions have been placed in the pores in order to close them. Simulations have been performed using the DLPOLY v2.19 code, developed at Daresbury Laboratory.[31] Both, water and POM, have been modeled as rigid molecules. Lennard-Jones potentials are used to describe the dispersion forces in addition to Coulombic contributions due to partial charges at specific locations. For water molecules we have considered the SPC/E model,[26] as done in the previous chapter where good agreement was found between structural simulated results and X-ray experiments. As far as the POM is concerned, we have used the LJ parameters given in ref [20], which are based on the criteria given in ref [145], and that have been used by ourselves and other authors to model rather complex polyoxometalates systems as well.[146–149] For the LJ interactions between unlike atoms i and j, we have used the Lorentz-Berthelot mixing rules: $\sigma_{ij} = \frac{1}{2}(\sigma_{ii} + \sigma_{jj})$, $\epsilon_{ij} = \sqrt{\epsilon_{ii}\epsilon_{jj}}$. Partial charges of the POM used in this paper have been determined by using the Qeq method[150] and are reported in ref [20]. Long range interactions have been treated using the Ewald summation technique,[2] with a convergence parameter of 0.210 and considering a maximum of 6 wave vectors in each direction. The Verlet leap-frog algorithm[3] was used to integrate the equations of motion with a time step of 1 fs and a cut-off of 18.5 Å. In order to optimize the CPU usage, we have used a Verlet neighbor list[2] with cut-off radius of 19.5 Å. The rigid body rotational motion is handled under the leapfrog scheme with Fincham's implicit quaternion algorithm,[35] with a tolerance of 10^{-4}. All simulations have been performed with cubic periodic boundary conditions. The volume of the box is equal to $70 \times 70 \times 70$ Å^3. The number of water molecules inside the POM is 172 as for the previous study with the $Mo_{132}(SO_4)$ POM. No external solvent has been considered. Both, equilibration and production runs, have been performed in the NVT ensemble, using Nosé-Hoover thermostat[39] to keep the temperature fixed with a relaxation time τ_T equal to 1 fs. The run lengths are 250 ps for equilibration runs and 5 ns for production runs. Positions and velocities are stored each 10 time steps.

DLPOLY output files are analyzed with a post-treatment constructed to determine the correlation functions and averages required for our analysis. To compute the $g(r)$, the cavity of the POM is divided into concentrical shells of width 0.011 Å. The SDF has been calculated by dividing the simulation box into voxels with a volume equal to 0.26^3 Å^3. The results for water confined inside the $Mo_{132}(SO_4)$ capsule have been taken from the previous chapter. For the $g(r)$ analysis, we have also performed a MD simulation of water inside the $Mo_{132}(HCO_2)$ capsule at $T = 198$ K. For the HB analysis we have performed a MD simulation of bulk water at $T = 298$ K to compare the obtained results with those calculated for water inside the POM. Probability distributions $P(\cos\theta_n^\alpha)$ are computed by dividing the interval of possible values that $\cos\theta_n^\alpha$, $[-1, 1]$, into 200 shells of width 0.01 as in the previous chapter.

3.4 Results

3.4.1 Local water structure

We have calculated the radial distribution function, $g(r)$, to study the structure of the water molecules inside the $Mo_{132}(HCO_2)$ nanocapsule and to compare with our previous results for the $Mo_{132}(SO_4)$ POM under the same thermodynamic conditions. In Figure 3.2, we plot $g(r)$, for both systems, where different peaks are observed. For clarity, we use the subscripts S and F to label these peaks for the $Mo_{132}(SO_4)$ and the $Mo_{132}(HCO_2)$ capsules, respectively. The first peak for the $Mo_{132}(HCO_2)$ POM, named β_F, occupies approximately the same position as the analogous peak for the $Mo_{132}(SO_4)$ POM, γ_S, but with a lower number of water molecules. Peak γ_F, located at about 6.88 Å, matches the minimum between peaks δ_{AS} and δ_{BS}. Then, a third peak, δ_F, is observed at about 8.77 Å from the center of the POM. Finally, a last peak ϵ_F is located close to the POM's wall, where water molecules interact with the MoO_5 pentagons.

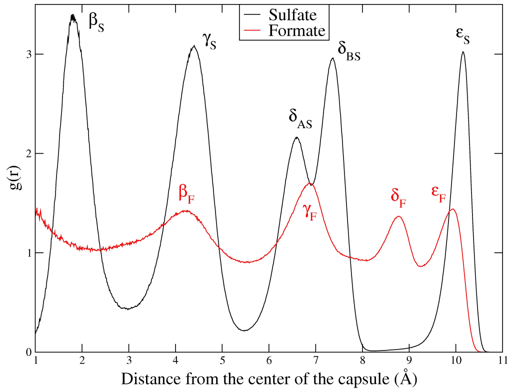

Figure 3.2: Radial distribution function $g(r)$ for the oxygen atoms of water molecules inside both $Mo_{132}(SO_4)$ and $Mo_{132}(HCO_2)$ POMs. Different subscripts are used to label the peaks for each POM.

The presence of peak δ_F in the $g(r)$ was not observed for the $Mo_{132}(SO_4)$ POM. The explanation mainly comes from the increase of the accessible volume that water molecules have when sulfate ligands are replaced by formate ligands. The tetrahedral symmetry of SO_4 ligands prevents water oxygens to approach those distances located between 8 and 9 Å from the center of the POM due to the vdw repulsion at short distances, and the electrostatic repulsion between oxygens. Hence, in $Mo_{132}(SO_4)$ capsule, water molecules are located either under molybdenum pentagons or in the pentagons of layer δ_{BS}. However, when formates are inside the POM, the presence of water oxygens at peak δ_F is favorable in terms of energy due to their interaction with the carbon and hydrogen atoms of the HCO_2 ligand, and to the lower vdw repulsion of the latter. At the same time, the charge of the POM surface is reduced from -72 to -42 and the water molecules in the outermost layer have a less rigid nature. It is interesting to notice that $g(r)$ takes a value close to the unity between peaks, when formates are inside the POM, suggesting more mobile water structures as compared to those inside the $Mo_{132}(SO_4)$ cavity. The comparison of the cumulative number of water molecules, $N(r)$, inside the POM for both ligands also shows this trend (see Figure 3.3). The quasi-buckyball structure described in $Mo_{132}(SO_4)$, makes $N(r)$ to increase in stair-like manner. However, for the $Mo_{132}(HCO_2)$ case, $N(r)$ smoothly increases suggesting that the peaks do not correspond to the same kind of structures as described in the previous chapter.

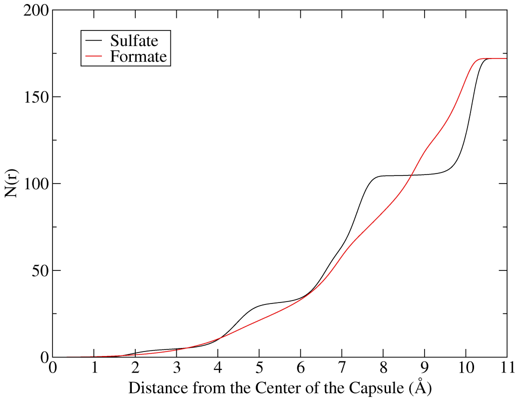

Figure 3.3: Cumulative number of oxygen atoms $N(r)$ in the $Mo_{132}(SO_4)$ and the $Mo_{132}(HCO_2)$ capsules.

To elucidate whether water molecules located at peaks γ_F and δ_F form a given linked structure, we plot the spatial distribution function, SDF for the water oxygen atoms. In Figure 3.4a we show the SDF for the $Mo_{132}(HCO_2)$ POM, as compared to the SDF calculated for the $Mo_{132}(SO_4)$ POM (Figure

3.4b), with different colors corresponding to different probability of presence for water oxygens. Although water is less structured inside $Mo_{132}(HCO_2)$ as observed from the $g(r)$, the SDF reveals well defined high probability regions, having the SDF a well defined structure with definite symmetry. The twelve centered-pentagons of the outermost layer observed in the SDF when having SO_4^{2-} as the ligand, are also present in this SDF, corresponding to the peak ϵ_F in the $g(r)$ plot. However, in this case, the twelve centered-pentagons are not isolated but connected to triangular located at the position of peak δ_F in the $g(r)$. Each triangular node is shared between three centered-pentagons, and it is also connected to peak γ_F located closer to the center of the POM. The position of the triangular nodes lies under the surface pores closed by guanidinium ions, while the SDF regions belonging to peak γ_F lie under the hydrogen atom of the formate ligand. The surface area of each triangular node is too small to contain more than one water molecule at the same time. The peak δ_F should correspond then to the $\{H_2O_{20/2}\}$ dodecahedron suggested in ref [20]. Notice, however, that the oxygens located at the triangular nodes are not hydrogen bonded between them, but with water molecules located at peaks ϵ_F and γ_F.

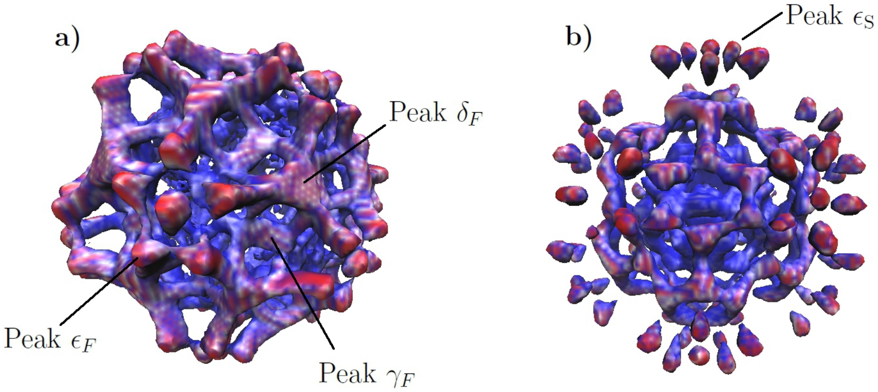

Figure 3.4: Isosurfaces of the spatial distribution function (SDF) for water oxygen atoms inside $Mo_{132}(HCO_2)$ capsule (a), and inside $Mo_{132}(SO_4)$ capsule (b). Red color indicates the regions with larger probability of finding a water oxygen, while blue color accounts for lower probability regions. For the $Mo_{132}(HCO_2)$ capsule we label the regions corresponding to the outer peaks for clarity.

Inner structures are not distinguishable from the SDF plot. Although peaks

γ_F, and δ_F can be described from the SDF plot, this global HB connected structure can not physically exist instantaneously as a structure connected by 3 HBs, since a total of 9 nodes connect peak δ_F with peaks ϵ_F, and γ_F, which is not compatible with the available number of HBs that a single water molecule can share with others. At the same time, as seen in Figure 3.3, the number of water molecules belonging to peak ϵ_F is about 48 instead of 72, which involves water migration from the outermost layer to inner regions. In fact, the SDF gives the regions where water molecules are located during the simulation with a given probability. Then, although the outermost water layer is the same as when sulfate ligands are located inside the POM, the well-defined paths connecting peaks δ_F and ϵ_F suggest a quite different situation in terms of the dynamics of the system.

Despite the fact that the SDF permits us to explain the nature of the peaks δ_F and γ_F, only peak δ_F is compatible with the $\{H_2O_{20/2}\}$ dodecahedron observed in Figure 3.1 (in red) at $T = 188$ K. The suggested $\{H_2O_{60}\}$ rhombicosidodecahedron is not observed neither in the $g(r)$ plot nor in the SDF plot at $T = 298$ K, indicating that this structure may only exist at lower temperatures. It is important to notice that the $\{H_2O_{60}\}$ rhombicosidodecahedron and the $\{H_2O_{20/2}\}$ dodecahedron do not satisfy the conditions for a hydrogen bonded physical structure of this kind to exist, as explained in section 2.2.1. Then, to close this section, we have performed an MD simulation at $T = 198$ K aiming at reproducing the $g(r)$ calculated in ref [20], and to infer the real physical structures formed by the water molecules. In Figure 3.5a, we plot the $g(r)$ for water inside the $Mo_{132}(HCO_2)$ at $T = 198$ K. As indicated in ref [20], a new bump is observed at about 7.8 Å, which matches that observed in X-ray measurements. The small distance between peak δ_F and the new bump should involve water molecules at these positions to be hydrogen bonded.

From simulations at $T = 298$ K, we have identified the 20 atoms corresponding to the nodes of the $\{H_2O_{20/2}\}$ to be located under the surface pores of the $Mo_{132}(HCO_2)$ capsule. At the same time, from X-ray data, we observe that the 12 pentagons corresponding to the nodes of the $\{H_2O_{60}\}$ rhombicosidodecahedron lie under the external twelve centered pentagons of the outermost water shell. Hence, as done for the water molecules inside the $Mo_{132}(SO_4)$ capsule, the most likely hydrogen bonded structure between the $\{H_2O_{60}\}$ structure and the most external $\{H_2O_{20/2}\}$ structure would be a $\{H_2O_{80}\}$ distorted buckyball as shown in Figure 3.5c. However, water molecules located at about 6.7 Å should also be hydrogen-bonded with those at 7.7 Å. In this case, if the positions for the water oxygen atoms at these distances from the center of the capsule, obtained from X-ray data, are connected, then, the most likely physical structure is another $\{H_2O_{80}\}$ buckyball (see Figure 3.5b). This structure, however, can not simultaneously exist with the most external suggested $\{H_2O_{80}\}$ buckyball shown in Figure 3.5c, since the total number of water molecules belonging to these structures would exceed the approximately 80 molecules located between 6.5 Å and 9 Å from the center of the POM, as seen in Figure 3.3. Then, the most likely hydrogen-bonded structure for water molecules at these positions should be a mixture of the $\{H_2O_{80}\}$ structures shown in Figure 3.5. That would lead to an under-occupation of the water layers as suggested in ref [20].

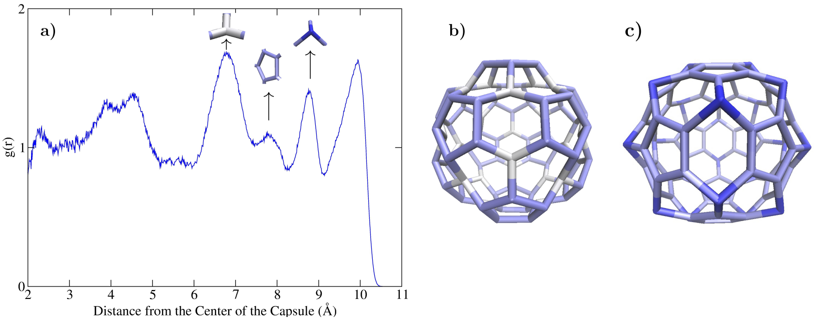

Figure 3.5: Radial distribution function $g(r)$ for water oxygen atoms inside the $Mo_{132}(HCO_2)$ capsule at $T = 198$ K (a), and suggested $\{H_2O_{80}\}$ hydrogen bonded physical structures (b-c). For clarity, in the $g(r)$ plot, we indicate which peaks contribute to the particular nodes in these structures.

The described hydrogen-bonded structure, however, is only possible at very low temperatures, where the potential interactions between molecules prevail over molecular agitation. When, the temperature is increased, the larger available volume under the surface pores for water molecules at peak δ_F makes this structure to break. At these conditions, the strong constraint imposed by the confining surface is reduced in the $Mo_{132}(HCO_2)$ capsule compared to that in the $Mo_{132}(SO_4)$, and then, the 12 hydrogen bonded pentagons of the $\{H_2O_{80}\}$ buckyballs shown in Figure 3.5 also break. Hence, the overall hydrogen bonded network transforms in that observed in the SDF in Figure 3.4.

3.4.2 Orientational distributions

To obtain further insight on the structure of the water molecules at different distance from the center of the $Mo_{132}(HCO_2)$ capsule at ambient conditions, we have calculated the distributions of angles $P(\cos\theta_n^{\alpha})$ for the water molecules located at different distances from the center of the POM. Here, α stands either for O-H, H-H, or μ directions, as defined in Section 2.4.4. Due to the absence of empty valleys between the peaks observed in Figure 3.2 for the $Mo_{132}(HCO_2)$, it has no much sense to divide the cavity into several layers, as done for the $Mo_{132}(SO_4)$ capsule in Section 2.2.1. However, as particular structures are seen in the SDF plot (Figure 3.4a), we define four shells accounting for the four peaks observed in the $g(r)$. The internal and external radius of the four shells are shown in Table 3.1.

Table 3.1: Internal and external radius of concentrical shells accounting for the peaks observed in the $g(r)$ of water inside the $Mo_{132}(HCO_2)$ POM.

Peak	Internal radius (Å)	External radius (Å)
β_F	3.73	5.00
γ_F	6.07	7.46
δ_F	8.13	9.21
ϵ_F	9.21	10.54

We begin with the analysis of the orientations of the water molecules belonging to peak δ_F. In Figure 3.6a, a high probability plateau region located between $\cos\theta_n^{\mathrm{OH}} \approx -0.74$ ($\theta_n^{\mathrm{OH}} \approx 137.7^{\mathrm{o}}$) and $\cos\theta_n^{\mathrm{OH}} \approx 0.65$ ($\theta_n^{\mathrm{OH}} \approx 49.5^{\mathrm{o}}$) is observed. This agrees with a wide range of possible orientations of the water molecules. However, two protuberances are observed at $\cos\theta_n^{\mathrm{OH}} \approx -0.74$ ($\theta_n^{\mathrm{OH}} \approx 137.7^{\mathrm{o}}$), and at $\cos\theta_n^{\mathrm{OH}} \approx 0.12$ ($\theta_n^{\mathrm{OH}} \approx 83.1^{\mathrm{o}}$). These two situations are not compatible with having one OH bond parallel or antiparallel to the radial vector from the center of the POM, as low probability is observed for either $\cos\theta_n^{\mathrm{OH}} = -1$ or $\cos\theta_n^{\mathrm{OH}} = 1$. They both agree with having one OH bond nearly parallel to the POM surface and the other slightly tilted towards peak ϵ_F ($\theta_n^{\mathrm{OH}} \approx 83.1^{\mathrm{o}}$) or towards peak γ_F ($\theta_n^{\mathrm{OH}} \approx 137.7^{\mathrm{o}}$). These two main orientations can also be observed from Figure 3.6b which shows a quite uniform orientational distribution for $\cos\theta_n^{\mathrm{HH}}$ but with two protuberances at $\cos\theta_n^{\mathrm{HH}} \approx -0.34$ ($\theta_n^{\mathrm{HH}} \approx 109.87^{\mathrm{o}}$), and at $\cos\theta_n^{\mathrm{HH}} \approx 0.34$ ($\theta_n^{\mathrm{HH}} \approx 70.12^{\mathrm{o}}$). Figure 3.6c for this layer, indicates that it is more likely to find the water molecules slightly tilted towards inner layers, as seen from the position of the peak at $\cos\theta_n^{\mu} \approx -0.19$ ($\theta_n^{\mu} \approx 101^{\mathrm{o}}$). The

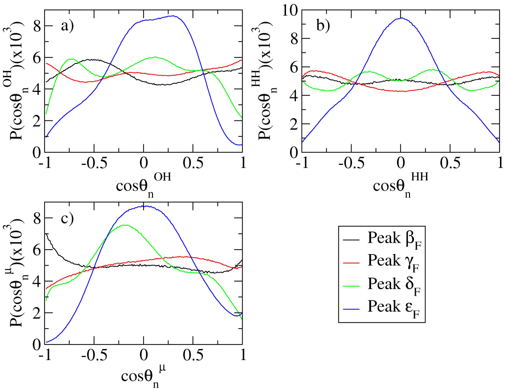

Figure 3.6: Orientational distributions $P(\cos\theta_n^{\mathrm{OH}})$ (a), $P(\cos\theta_n^{\mathrm{HH}})$ (b), and $P(\cos\theta_n^{\mu})$ (c) for the different peaks observed in the $g(r)$ plot for the $Mo_{132}(HCO_2)$ POM.

large width of this peak also agrees with the tilt towards peak ϵ_F observed in $P(\cos\theta_n^{\mathrm{OH}})$, and $P(\cos\theta_n^{\mathrm{HH}})$. With regard to peak ϵ_F, Figure 3.6a shows a plateau of high probability between $\cos\theta_n^{\mathrm{OH}} \approx -0.1$ ($\theta_n^{\mathrm{OH}} \approx 95.7^{\mathrm{o}}$) and $\cos\theta_n^{\mathrm{OH}} \approx 0.36$ ($\theta_n^{\mathrm{OH}} \approx 68.9^{\mathrm{o}}$). The first angle, $\theta_n^{\mathrm{OH}} \approx 95.7^{\mathrm{o}}$, agrees with the situation observed in the SDF, that is, the connection between water molecules at peak ϵ_F with those located at peak δ_F. In this case, the other OH bond remains perpendicular to the radial vector. The second angle, $\theta_n^{\mathrm{OH}} \approx 68.9^{\mathrm{o}}$ corresponds to water molecules with an OH bond tilted towards the POMs confining surface and the other perpendicular to the radial vector, $\vec{n}$. The intermediate angles of the plateau indicates a significant population of water molecules lying rather flat on the plane perpendicular to the radial vector as seen also from the values $\cos\theta_n^{\mathrm{HH}} \approx 0$, and $\cos\theta_n^{\mu} \approx 0$ in Figure 3.6b and Figure 3.6c. With regard to more internal layers, the angle distributions are rather flat suggesting that water molecules can take several orientations. The analysis of the orientational distributions, reveals quite different results from the case of water inside the $Mo_{132}(SO_4)$ capsule. In that case, very well-defined peaks were found for the probability distributions of water molecules located at the different rigid layers, and regions of very low probability were also found, suggesting that several orientations were not allowed. For the $Mo_{132}(HCO_2)$ POM, however, even if some orientations are more likely, at least, for the external shells, the large ensemble of possible orientations observed in Figure 3.6 suggests that the molecules have a larger freedom to change its orientation and then a faster dynamics of the system is expected, as compared to the $Mo_{132}(SO_4)$ capsule. The very low value that $P(\cos\theta_n^{\mathrm{OH}})$ takes at $\cos\theta_n^{\mathrm{OH}} = \pm 1$ indicates that water oxygens belonging to peak δ_F in $g(r)$ should be located under the pores closed by the guanidinium atoms. In fact, it is the only region which permits the water molecules of peaks ϵ_F and δ_F to be hydrogen bonded between them. If water molecules located at peak δ_F had large values for $P(\cos\theta_n^{\mathrm{OH}})$ at $\cos\theta_n^{\mathrm{OH}} = 1$, that would imply too small distances between water molecules and both electrostatic and vdw repulsion would make the molecules at peak δ_F to move away. Then, the presence of oxygen atoms at this distance from the center of the POM is driven by the available volume and by the interaction with the hydrogen and carbon atoms of the formate ligand. This situation is totally different than for the $Mo_{132}(SO_4)$ capsule where the water hydrogen atoms occupied the region located at a distances between 8 and 9 Å from the center of the POM. Water molecules located at inner regions inside the $Mo_{132}(HCO_2)$ capsule, do not have constraints neither due to the POMs surface nor to the positions of the ligands, and, then, their orientations with respect to the radial vector, $\vec{n}$ are nearly uniformly distributed.

3.4.3 Hydrogen bonding and tetrahedral order

We have calculated the mean number of hydrogen bonds $\langle N_{\mathrm{HB}}\rangle$ as a function of the distance, d, to the center of the POM (see Figure 3.7) at ambient conditions. A part from the value of $\langle N_{\mathrm{HB}}\rangle$ at the regions defined in Figure 3.1, we have also calculated its value at about 2 Å and 7.8 Å. Similarly to the case of water inside the $Mo_{132}(SO_4)$ capsule, the value for $\langle N_{\mathrm{HB}}\rangle$ is approximately the same as that of bulk water for $d < 8$Å. For water molecules located between 8 and 9 Å from the center of the $Mo_{132}(HCO_2)$ capsule, $\langle N_{\mathrm{HB}}\rangle$ is reduced due to the interaction of the water oxygens with the formate ligands. However, these water molecules are still able to form near 3 HBs with other water molecules. Water molecules in the outermost layer are bound to the atoms of the POMs internal wall, and hence their capability of sharing HBs with other water molecules is reduced with respect to water molecules at other locations. These situations are also observed in Figure 3.8 where we plot the histograms of the number of HB per molecule inside the $Mo_{132}(HCO_2)$ capsule for different peaks compared to the same quantity for bulk water. The histograms for water molecules located at peaks β_F and γ_F match that of bulk water. For peak δ_F, we observe a shift of the histogram to the left due to the fact that water molecules in this region

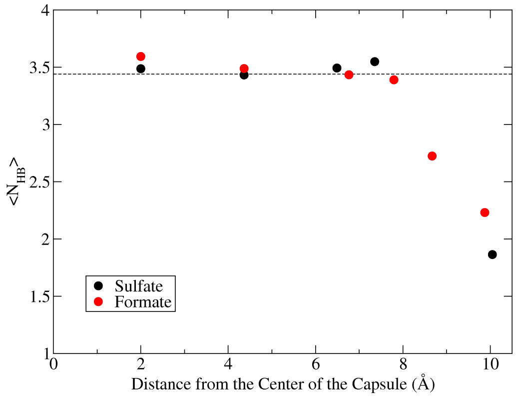

Figure 3.7: Mean number of HB per water molecule $\langle N_{\text{HB}} \rangle$ for water inside both $Mo_{132}(SO_4)$ and $Mo_{132}(HCO_2)$ POMs, at different distances from the center of the capsules.

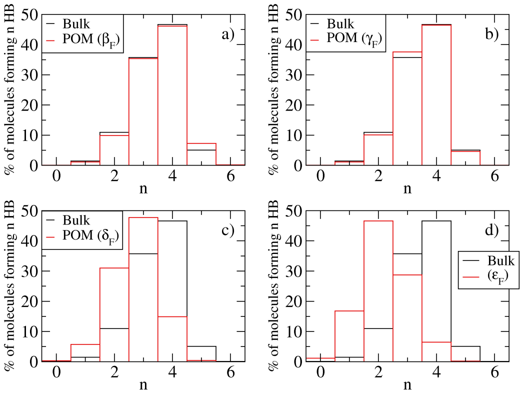

Figure 3.8: Histograms of the number of water molecules inside the $Mo_{132}(HCO_2)$ capsule forming n HB in peak β_F (a), γ_F (b), δ_F (c) and ϵ_F (d) as compared to bulk water.

share HBs with the HCO_2 ligands. Finally, Figure 3.8d shows a reduction of the number of water molecules forming 3 HBs. Although the qualitative behavior is the same as that observed in Figure 2.5d for the $Mo_{132}(SO_4)$, an increase of the number of water molecules forming 2, 3, and 4 HBs is observed. This increase is due to the new HBs that water molecules in contact to the POMs wall can form with the water molecules located at peak δ_F.

Finally, to better understand the structure of water molecules inside the $Mo_{132}(HCO_2)$, and to close this section, in Figure 3.9 we show the results for the tetrahedral parameter q, compared to those obtained for the $Mo_{132}(SO_4)$ POM as a function to the center of the POM. The results for distances $d < 8$Å

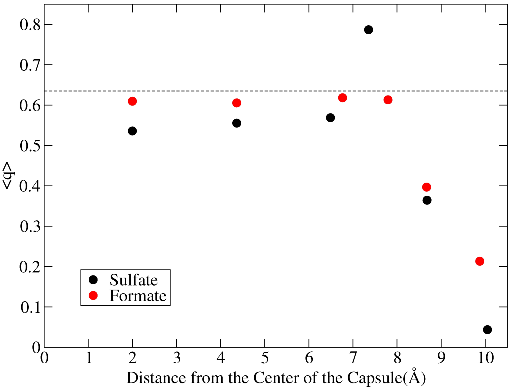

Figure 3.9: Mean tetrahedral parameter $\langle q \rangle$ for water inside both $Mo_{132}(SO_4)$ and $Mo_{132}(HCO_2)$ POMs, at different distances from the center of the capsules.

do not significantly differ from what we observe in bulk water. It is interesting to notice the different value for q between both POMs at a distance around 7.5 Å. Tetrahedral order of water molecules at distances larger than 8 Å is reduced due to the same causes than the reduction of $\langle N_{\rm HB} \rangle$ for the same distances. However, a slight increase of q for water molecules in contact to the POMs wall is seen when formate ligands are inside the capsule instead of sulfate ligands. This increase, also observed in $\langle N_{\rm HB} \rangle$, reflects the less rigid nature of water molecules in the outermost shell as compared to the situation in the $Mo_{132}(SO_4)$ POM. This is a result of the reduced volume of formate ligands as compared to sulfate ligands which permits the water molecules to change its orientation to maximize $\langle N_{\rm HB} \rangle$ and the tetrahedral parameter q.

3.4.4 Translational diffusion

To see if water diffuses differently in both the $Mo_{132}(HCO_2)$ and $Mo_{132}(SO_4)$ POMs at the same thermodynamic conditions, we have calculated the MSD as seen in Figure 3.10. As expected from the previous section results, the diffusion is much larger when formates are located inside the POM, being the MSD between 4-5 times larger than when sulfates are considered. This increase, which can be observed in the edges connecting the different water structures in the SDF, indicates that water is not structured inside the $Mo_{132}(HCO_2)$ POM in layers. In this case, although several high probability regions at distances closer to the POMs wall are observed, water molecules can diffuse between them through the edges connecting the structures. When sulfates are instead placed inside the Mo_{132} capsule, diffusion between external layers occurs only via a simultaneous switch of two water molecules. These switches occur in the nanosecond time scale and as a large percentage of water molecules occupy external layers, the MSD increases slower than for the $Mo_{132}(HCO_2)$ nanocapsule.

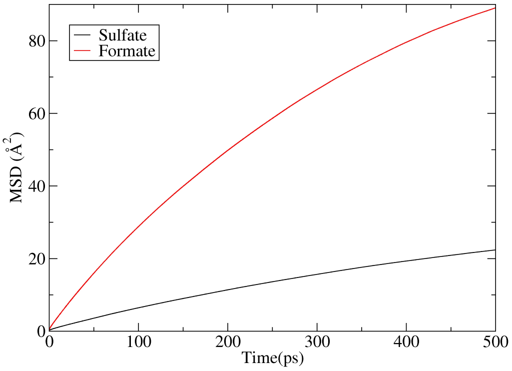

Figure 3.10: Mean-squared displacement of water molecules inside the $Mo_{132}(SO_4)$ and the $Mo_{132}(HCO_2)$ POMs.

The difference in water translational diffusion between both nanocapsules is also reflected in Figure 3.11 (a-b), where we plot the distance $d(t)$ of two tagged water molecules to the center of the $Mo_{132}(HCO_2)$ POM. In both cases, we observe several excursions of water molecules located at peaks β_F and γ_F, to peak ϵ_F. This situation is totally different from that observed for $Mo_{132}(SO_4)$

where few switches are observed in a nanosecond timescale between peak ϵ_S and peak δ_{BS} (see Section 2.4.4). Although we only plot the distance $d(t)$ for two tagged molecules, we shall say that the same behavior is observed for all the water molecules inside the $Mo_{132}(HCO_2)$ capsule whatever it is its initial position. However, due to the negative charge of the POM, water molecules spend more time in peak ϵ_F than in other regions. Water molecules also occupy peak δ_F for periods of about hundreds of picoseconds. This fact suggests that peak δ_F is not a transient position for water molecules and, hence, the observed triangular nodes are quite stable regions due to the interaction with the HCO_2 ligand and the available volume. The scenario observed in Figure 3.11 indicates that the particular water molecules occupying the peaks change rapidly with time due to the translational diffusion that occurs inside the $Mo_{132}(HCO_2)$ capsule. As water molecules diffuse very fast inside the $Mo_{132}(HCO_2)$ capsule compared to the $Mo_{132}(SO_4)$, we have not calculated dynamic quantities such as the HB correlation function intra and inter layer. The analysis of the covariance matrix and the associated correlation functions calculated in Sections 2.4.2 and 2.4.3 for water inside the $Mo_{132}(SO_4)$ POM have also not been calculated as they strongly depend on the criteria for the selection of the limits of each shell dividing the interior of the $Mo_{132}(HCO_2)$ capsule.

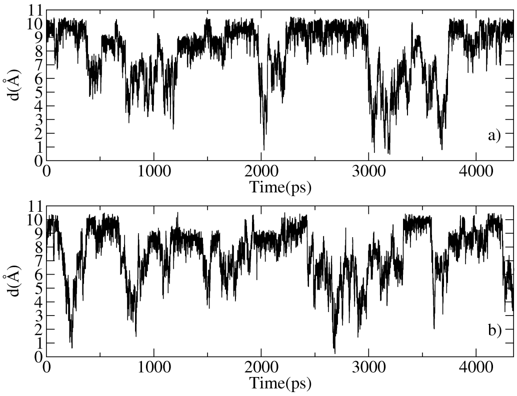

Figure 3.11: Distance $d(t)$ from the center of the $Mo_{132}(HCO_2)$ POM for two tagged water molecules (a), and (b).

3.4.5 Reorientational dynamics

We have also studied the relaxation of the dynamics of the orientation of the OH vector for a water molecule through the decay of the $C_{2,OH}(t)$ correlation function. As this function can be compared to rotational anisotropy decay measurements, we compare our simulation results for both Mo_{132} POMs and bulk water, to simulation results for a reverse micelle, $w_0 = 4$, with 140 water molecules, and to the experimental data for a reverse micelle $w_0 = 5$, with about 300 molecules, as shown in Figure 3.12. In the first place, we shall remark the faster decay of $C_{2,OH}(t)$ for water molecules inside the $Mo_{132}(HCO_2)$ POM as compared to that inside the $Mo_{132}(SO_4)$ POM. This result is compatible with the higher translational diffusion observed for water in Figure 3.10 for the $Mo_{132}(HCO_2)$ POM which indicates a less constrained environment for water molecules which have more freedom to rotate than in the $Mo_{132}(SO_4)$ POM. Although in our simulations the POM capsule is rigid, the larger mobility of water molecules when formate ligands are inside, leads to a orientational dynamics of water molecules similar to that observed in RMs of similar size, as shown in Figure 3.12 for the simulated results for the $w_0 = 4$ RM. Finally, as observed in ref [16], experimental anisotropy decay for RMs decays slower than simulated data, although it has the same qualitative behavior. For the kind of POM nanocapsules

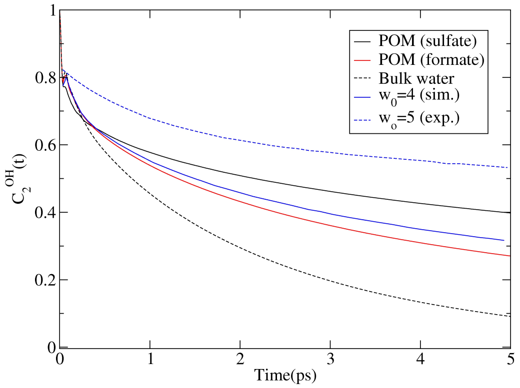

Figure 3.12: Comparison of calculated reorientational correlation function, $C_{2,OH}(t)$, for the $Mo_{132}(SO_4)$ and $Mo_{132}(HCO_2)$ POMs with simulated data for a RM, $w_0 = 4$, and experimental data for a RM, $w_0 = 5$. Bulk water results for the same property are also shown.

we study, which were firstly synthesized in the last decade, no experimental data is available, at least, to our knowledge, to compare to, for this property. In this sense, it would be important to perform such experiments in order to test if the chosen force field is good enough to reproduce the dynamics of confined water inside Mo_{132} POMs.

3.5 Conclusions

In this chapter, we have studied the effect of the ligand on the structure and dynamics of water inside Mo_{132} cavities at ambient conditions. For that purpose, we have considered sulfate (SO_4^{2-}) and formate (HCO_2^-) ligands.

The results for the radial and spatial distribution functions show that water molecules do not form the buckyball-like structures present inside the $Mo_{132}(SO_4)$ capsule. The presence of the HCO_2 ligand inside the POM leads water molecules to occupy a new region located under the POM surface pores at a distance from the center of the cavity about 8.5 Å. This behavior is not observed when sulfate ligands are considered. We attribute this fact to the lower volume and lower vdw repulsion of HCO_2 ligands compared to SO_4 ligands, and to the electrostatic attraction between water oxygens and the hydrogen and carbon atoms of the formate ligand. The analysis of the SDF and the orientational probability distributions reveal that water molecules at this region are hydrogen bonded to the water molecules at the 12 centered pentagons of the outermost water layer and are also hydrogen bonded to those molecules located under the formate ligands. The analysis of the HB statistics and the tetrahedral parameter also agree with that view. We have observed, however, that at low temperature ($T = 198$ K), water molecules inside the $Mo_{132}(HCO_2)$ tend to form buckyball structures with 12 pentagons and a variable number of hexagons, as observed inside the $Mo_{132}(SO_4)$ for low and high temperatures.

We have also studied the translational diffusion of water molecules inside both POMs. The analysis of the mean-squared displacement together with the variation of the position of water molecules with time shows that water diffuses much faster inside the $Mo_{132}(HCO_2)$ capsule. In this case, the presence of water molecules at about 8.5 Å from the center of the POM permits water molecules to diffuse from the outermost layer to inner regions. This behavior is observed for all water molecules suggesting that the HB network inside the $Mo_{132}HCO_2)$ reorganizes quite fast, contrarily to that observed in the $Mo_{132}(SO_4)$ capsule.

Finally, we have studied the dynamics of orientation of water molecules through the decay of the $C_{2,\mathrm{OH}}(t)$ correlation function. The result for this quantity in the $Mo_{132}(HCO_2)$ capsule is close to that simulated in the RMs of similar size in ref [16], suggesting a similar orientational dynamics between both systems. Water molecules inside the $Mo_{132}(SO_4)$ have less freedom to change their orientation due to the more constrained environment inside this capsule.

In the present chapter we have shown that minor changes in the structure of the ligand inside Mo_{132} cavities leads to rather different water structures with different dynamical behavior. We have suggested the main causes of such differences. The different structures have been yet experimentally studied in ref. [20] at low temperature, however, there does not exist a direct comparison in terms of the dynamics in both systems at ambient conditions. In this sense, this study provides simulated data for the reorientation dynamics in both systems which can be directly compared to pump-probe anisotropy decay experiments.

Chapter 4

Molecular modeling of diffusion coefficient and ionic conductivity of CO_2 in aqueous ionic solutions

4.1 Introduction

The emission of greenhouse gases to the atmosphere due to strong industrial human activity is in general recognized to be the main cause of the increase of the global mean temperature on Earth in the 20th century.[151] After water vapor, CO_2 is the gas which contributes more to the greenhouse effect. The burning of fossil fuels like coal, oil and natural gas as well as tropical lands deforestation have contributed to an accumulation of CO_2 in the atmosphere.[152] As a consequence, the atmospheric concentration of CO_2 has increased from 280 ppm in 1880 to 367 ppm in 1999.[151] One of the important aspects related to CO_2 is the capacity of the natural reservoirs (biosphere and oceans) to reabsorb an important percentage of the CO_2 emitted to the atmosphere (approx. 30%).[151] However, while the residence time for the CO_2 in the biosphere is on the order of a decade, the residence time for the CO_2 in the deep oceans is on the order of a millennium. Then, among the economically and technically feasible options to reduce CO_2 emissions, the sequestration of CO_2 either in the deep ocean or in the geological media has become increasingly realistic. Candidate geological media include saline aquifers, oil/gas reservoirs and coal formations.[153–155] Since the last decade, some CO_2 storage projects are in operation in different regions all over the world.[156–158]

Pressure and temperature in a geological formation depend on its depth. The mean temperature gradient in a geological formation varies between 25 and 30°C/km although in some cases reaches 60°C/km.[21] The surface temperature ranges between 5 and 20°C and the pressure ranges from 10 bar on the surface to 500 bar in the deepest aquifers.[21] Most of the proposed reservoirs to store the CO_2 are deeper than 500 meters. By taking a look at the phase diagram of CO_2, we see that it becomes supercritical at $T > 31.1°\mathrm{C}$ and $P > 73.8$ bars.[69] Then, if we consider a mean temperature gradient of 30°C/km to 60°C/km, CO_2 will be supercritical at a depth close to 800 meters. In terms of salinity, the main part of the geological formations have a high salinity, greater than 100 g/l, with typically chloride as the dominant anion and sodium as the dominant cation.[22,159] Only reservoirs with high salinity can be considered for CO_2 storage as the rest are restricted for irrigation or human supply. However, the knowledge of these deep formations and the processes which affect CO_2 diffusion, as well as the effect of the CO_2 on the other properties of the CO_2-brine mixture, still remain poorly understood. This is why simulation models can be used to predict and understand the behavior of these systems under reservoir conditions by considering the geochemical, hydrological, and mechanical processes that take place in reservoirs.

Reservoir simulation models are used to study the impact of CO_2 injection both in oceans and in geological formations. For the diffusion of CO_2 into deep oceans, the models more often used are box type models.[160,161] The quantity of CO_2 dissolved in the ocean is calculated by considering the amount of CO_2 present in the atmosphere and taking into account the acid-base equilibrium of CO_2 in water. Oceans are modeled as the sum of two parts: the superficial ocean which exchanges CO_2 in an active way with the atmosphere and the deep ocean in which CO_2 diffuses. For the geological sequestration of CO_2 reactive transport models are used to describe the evolution of CO_2 in space and time scales.[162] Reactive transport modeling integrates the geochemical, hydrological, and mechanical processes that characterize dynamic geological systems. These processes, which include chemical reactions, fluid flow, heat transfer, and mechanical stress and strain, are interdependent and must be modeled simultaneously to simulate the true behavior of geologic systems. Reservoir simulation methods require some experimental data such as solubility of CO_2 in brine mixtures and its diffusion coefficient at different thermodynamic and salinity conditions.

Determination of solubility of dissolved gases in brine is possible experimentally. However, the measurement of diffusion coefficients of such mixtures is extremely difficult since it requires the implementation of very complex experimental protocols. Moreover, the influence of possible impurities makes experiments very difficult. As an alternative, different theoretical approaches have been used to describe mass transport in multicomponent systems. These approaches, which include hydrodynamic theory, kinetic theory or the so-called Maxwell-Stefan (MS) equations, are, in general, of limited application. However, some authors have shown that MS relations, combined with the use of molecular simulation techniques, can provide mass transport parameters, including diffusion coefficients or electrical conductivities for systems containing an arbitrary number of species.[23,24,27] Therefore, Molecular dynamics simulations (MD) are a good complement to experiments to determine physical properties in complex systems. In this respect, Zabala et al. have succeeded in modeling mass diffusion coefficients of CO_2-hydrocarbon mixtures at reservoir conditions by means of molecular dynamics simulations.[163] In that reference, the obtained quantities are Maxwell-Stefan mutual diffusion coefficients. With the calculation of the so-called thermodynamic factor one obtains the corresponding Fick diffusion coefficients.

Another way to analyze the dynamic behavior of CO_2 in brine is to explore the reoriententional relaxation time of the different species in the system. Orientation relaxation dynamics of water molecules in CO_2-brine mixtures would give us indirect information about the hydrogen bond pattern and how it is affected by increasing salt concentration, temperature, and CO_2 concentration. In this context, by defining relevant vectors in water and CO_2 molecules, we can study whether rotations around some of this axis are affected by the different conditions.

The aim of this chapter is to calculate CO_2 mass diffusion coefficients, self diffusion, as well as rotational relaxation times, in brine mixtures under the thermodynamic conditions of water reservoirs, using molecular dynamics simulations. The intermolecular potentials for the different species in the mixture have been taken from the literature. To the best of our knowledge, a prediction of this kind has not been done, neither experimentally nor using MD simulations, yet. Hence, our results are the first estimation of mass-diffusion and rotational relaxation times of CO_2 in deep saline aquifers. Finally, we calculate in addition the electrical conductivities of CO_2-brine mixtures under the same thermodynamic conditions, and compare them to an experimental correlation available in the literature for the case where its use is prescribed.

4.2 Theoretical Methods

4.2.1 Diffusion

Diffusive mass transfer in mixtures can be described by Fick's law. Fick's law is a phenomenological law that relates the molar diffusion flux of a solute species (referred to as 2, the index 1 is reserved to the solvent, from now on) with the gradient of concentration for the solute species. In a binary mixture it reads:

$$J_2 = -c_t D \nabla x_2 \tag{4.1}$$

where J_2 is the solute molar diffusive flux, c_t is the mixture molar density, x_2 is the mole fraction of the solute, and D is the binary Fick diffusion coefficient of the mixture. This phenomenological law expresses the underlying linear relationship between the dissipative flux J_2 (more specifically the molar velocity $v_2 = J_2/c_2$, where c_2 is the mole concentration of species 2) and the conjugated thermodynamic force $-\frac{c_2}{RT}\nabla_{P,T}\mu_2$ where the subscripts T and P stand for constant temperature and pressure and μ_2 is the chemical potential of species

2.[164] In the multicomponent system one writes in general

$$J_i = -c_t \sum_{\substack{j=1 \\ i\neq j}}^{n} [D]_{ij} \nabla x_j \tag{4.2}$$

By construction, $\sum_{i=1}^{n} J_i = 0$ and $\sum_{i=1}^{n} x_i = 1$, with n being the total number of species. Moreover, $[D]_{ij}$ is the ij-element of the $(n-1)\times(n-1)$ matrix of diffusion coefficients. Eq 4.2 also expresses the coupling between the diffusive flux of one species with all gradients of composition. Therefore, in a binary solution D_{22} stands for the Fick diffusion coefficient of the solute 2 in the mixture with solvent 1. From a practical point of view, the diffusion coefficients are strongly dependent functions of the thermodynamic state for non-ideal mixtures. On the other hand, the Maxwell-Stefan theory that we will use along the paper considers that the thermodynamic force acting on species i is instantaneously balanced by a *mechanical friction* with the rest of the species present in the system, the latter defined as $d_{ij} = (x_j J_i - x_i J_j)/c_t D_{ij}^{\mathrm{MS}}$. Then, equalling d_{ij} to the conjugated thermodynamic force we obtain the following equation:

$$-\sum_{j\neq 1} d_{ij} - \frac{x_i}{RT}\nabla_{T,P}\mu_i = 0 \tag{4.3}$$

The coefficients D_{ij}^{MS} are referred to as the Maxwell-Stefan coefficients, which satisfy $D_{ij}^{\mathrm{MS}} = D_{ji}^{\mathrm{MS}}$ due to the Onsager symmetry relations.[25] One of these equations is redundant due to the fact that $\sum_{i,j\neq i} d_{ij} = 0$, by construction, and $\sum_i \frac{x_i}{RT}\nabla_{T,P}\mu_i = 0$ due to the Gibbs-Duhem equation. In the Maxwell-Stefan theory (MS), then the equivalent to eq 4.2 takes the form

$$J_i = -c_t \sum_{j=2}^{n} [B^{-1}]_{ij} (x_j \nabla_{T,P}\mu_j) \tag{4.4}$$

where the elements of the matrix $[B]$ are defined in terms of the phenomenological MS diffusion coefficients as follows:

$$B_{ii} = \frac{x_i}{D_{i1}^{\mathrm{MS}}} + \sum_{\substack{k=1 \\ k\neq i}}^{n} \frac{x_k}{D_{ik}^{\mathrm{MS}}} \tag{4.5}$$

$$B_{ij} = -x_i \left(\frac{1}{D_{ij}^{\mathrm{MS}}} - \frac{1}{D_{i1}^{\mathrm{MS}}} \right) \qquad i,j = 2,\ldots,n \tag{4.6}$$

Then, the relationship between the Fick diffusion coefficients and the MS coefficients is given through a matrix of thermodynamic factors $[Q]$ defined as:[23,25]

$$[Q]_{ij} = \delta_{ij} + x_i \left(\frac{\partial \ln \varphi_i}{\partial x_j} \right) \tag{4.7}$$

where φ_i is the fugacity coefficient of species i, and δ_{ij} stands for the Kronecker symbol. Therefore, it is assumed that

$$[D] = [B]^{-1}[Q] \tag{4.8}$$

In this work, we straightforwardly determine the elements of the matrix $[B]^{-1}$ through molecular dynamics simulation. However, once known $[B]^{-1}$, one can obtain the matrix of Maxwell-Stefan coefficients $[D^{\mathrm{MS}}]$ from eqs 4.5 and 4.6. Equivalently, the matrix of Fick diffusion coefficients can also be obtained from eq 4.8 by calculating the thermodynamic matrix $[Q]$ from appropriate models for the fugactiy coefficient φ_i using, for instance, equations of state (EOS) or thermodynamic activity coefficient models. In general, for non-ideal mixtures, in one hand, $[Q]$ is a strong function of mixture composition while D_{12}^{MS} is generally weakly composition dependent. On the other hand, for the case of thermodynamic ideal liquid mixtures, $\varphi_i = 1$ and, consequently, $[Q]$ tends to the identity matrix [1]. In this last situation, in a binary mixture, the Fick diffusivity is equal to the MS diffusivity. In the multicomponent case, one has in this limit $[D] = [B]^{-1}$. Of course, this is also the case in a dilute solution.

From molecular dynamics simulations, MS diffusion coefficients can be calculated from the elements Λ_{ij} of an n-dimensional symmetric matrix of the so-called Onsager coefficients $[\Lambda]$. These coefficients are evaluated from the correlations in the system, according to either generalized Einstein's relations[24]

$$\Lambda_{ij} = \frac{1}{6N} \lim_{\Delta t \to \infty} \frac{1}{\Delta t} \left\langle (\sum_{k=1}^{N_i} \vec{r}_{i,k}(t+\Delta t) - \sum_{k=1}^{N_i} \vec{r}_{i,k}(t)) \cdot (\sum_{m=1}^{N_j} \vec{r}_{j,m}(t+\Delta t) \sum_{m=1}^{N_j} \vec{r}_{j,m}(t)) \right\rangle \tag{4.9}$$

or the equivalent Green-Kubo expressions.

$$\Lambda_{ij} = \frac{1}{3N} \int_0^\infty \left\langle \left(\sum_{k=1}^{N_i} \vec{V}_{i,k}(0) \cdot \sum_{m=1}^{N_j} \vec{V}_{j,m}(t) \right) \right\rangle \tag{4.10}$$

Notice that the variables of the correlation in both eqs 4.9 and 4.10 are the baricenters of the mass distribution of each species. These expressions need not to be confused with expressions for the self-diffusion coefficients. The elements Λ_{ij} satisfy the mass balance constraint given by

$$\sum_i M_i \Lambda_{ij} = 0 \tag{4.11}$$

Here, $\vec{r}_{i,k}(t)$ is the center-of-mass position vector of molecule k, belonging to species i, $\vec{V}_{j.m}(t)$ is the center-of-mass velocity vector of molecule m, belonging to species j, M_i is the molecular mass of species i, N is the total number of molecules, and N_i is the number of molecules of the ith species. The Onsager coefficients are related to the elements of an $(n-1)$-dimensional matrix $[\Delta]$ by[24]

$$\Delta_{ij} = (1 - x_i)\left(\frac{\Lambda_{ij}}{x_j} - \frac{\Lambda_{i1}}{x_1}\right) - x_i \sum_{\substack{k=1\\k\neq i}}^{n} \left(\frac{\Lambda_{kj}}{x_j} - \frac{\Lambda_{k1}}{x_1}\right) \tag{4.12}$$

The matrix inverse of $[\Delta]$ is precisely the $[B]$ matrix and, hence,

$$[B]^{-1} = [\Delta] \tag{4.13}$$

For the case of binary mixtures ($n = 2$), the matrices $[\Delta]$ and $[B]$ are scalars, and so is $[Q]$. Using eq 4.5 and remembering that $\sum_{i=1}^{n} x_i = 1$, the MS diffusion coefficient D_{12}^{MS} is obtained,

$$B_{11} = \frac{1}{\Delta_{11}} = \frac{x_1}{D_{12}^{\mathrm{MS}}} + \frac{x_2}{D_{12}^{\mathrm{MS}}} = \frac{1}{D_{12}^{\mathrm{MS}}} \tag{4.14}$$

$$D_{12}^{\mathrm{MS}} = \Lambda_{11} = x_2\left(\frac{\Lambda_{11}}{x_1} - \frac{\Lambda_{12}}{x_2}\right) - x_1\left(\frac{\Lambda_{21}}{x_1} - \frac{\Lambda_{22}}{x_2}\right) = \frac{x_2\Lambda_{11}}{x_1} + \frac{x_1\Lambda_{22}}{x_2} - \Lambda_{12} - \Lambda_{21} \tag{4.15}$$

The equations for ternary mixtures ($n = 3$) and quaternary mixtures ($n = 4$) are presented in the Supporting Information section.

For the purpose of this chapter, it is interesting to consider that the system is diluted. In particular, that the mole fraction of the solvent (water) x_1 is of order 1 and one order of magnitude larger than that of the ionic species in the brine x_i, $i = 3, 4, \ldots, n$, which, in turn, are one order of magnitude larger than the mole fraction of the dissolved CO_2, x_2. Furthermore, from the definition of eq 4.9 we observe that $\Lambda_{ij} \propto x_i x_j$. In addition, if $i \neq j$ the variable rapidly changes sign, giving a smaller contribution than the $i = j$ case. Hence, if we denote by ϵ

the order of magnitude of the small quantities (the mole fractions of the solutes as well as the contributions of the off-diagonal elements), then $\Lambda_{ij} \propto \epsilon^2$ for $i = j$, and $\Lambda_{ij} \propto \epsilon^3$ for $i \neq j$. We will consider that the dependent diffusive flow is that of the solvent (species 1). Notice, that the particular case of Λ_{11} could be conceived as the larger term, according to the previous arguments. However, in view of eq 4.11, this contribution is at least of the order of $\Delta_{i1} \propto \epsilon^3$ with $i \neq 1$. Therefore, due to the considerations just made, the off-diagonal elements of the Onsager matrix of coefficients are much smaller than the diagonal ones. The matrix $[\Delta]$ under these approximation takes the form

$$\Delta_{ij} \approx (1 - x_i)\left(\frac{\Lambda_{ii}}{x_i}\right)\delta_{ij} + \left(\frac{\Lambda_{ij}}{x_j}\right)(1 - \delta_{ij}) + \mathcal{O}(\epsilon^3) \tag{4.16}$$

Therefore, from eq 4.4 and 4.16, up to the leading order for diagonal and off-diagonal terms, the diffusive fluxes can be written as ($i \neq 1$)

$$J_i = -c_t \sum_{j=2}^{n} \left[(1 - x_i)\left(\frac{\Lambda_{ii}}{x_i}\right)\delta_{ij} + \left(\frac{\Lambda_{ij}}{x_j}\right)(1 - \delta_{ij})\right] x_j \nabla_{P,T}\mu_j \tag{4.17}$$

Under this approximation, the Fick diffusion coefficients are given from eq 4.8 by

$$D_{ij} \cong \sum_{k=2}^{n} \left[(1 - x_i)\left(\frac{\Lambda_{ii}}{x_i}\right)\delta_{ik} + \left(\frac{\Lambda_{ik}}{x_k}\right)(1 - \delta_{ik})\right] Q_{kj} \tag{4.18}$$

The leading order reads

$$D_{ij} \cong \left(\frac{\Lambda_{ii}}{x_i}\right) Q_{ij} \tag{4.19}$$

Notice that $D_{ij} \neq D_{ji}$ for the Fick's diffusion coefficients, according to the notation used along this work. This expression cannot be further approximated without an explicit knowledge of the elements of the matrix of thermodynamic factors, although in most cases will be dominated by the diagonal elements. To obtain the MS diffusivities, requires a little bit more of algebra. Effectively, according to our hypothesis, the matrix $[\Delta]$ is dominated by the diagonal terms. Therefore, we can invert (left inverse) this matrix using the off-diagonal terms as a perturbation. The inverse matrix is an approximation of the $[B]$ matrix, which, up to first order, reads

$$B_{ij} \approx \frac{x_i}{\Lambda_{ii}}\delta_{ij} - \frac{x_i \Lambda_{ij}}{\Lambda_{ii}\Lambda_{jj}}(1 - \delta_{ij}) + \mathcal{O}(\epsilon) \tag{4.20}$$

On the other hand, eqs 4.5 and 4.6 can also be approximated with regard to the concentrations. Eq 4.5 can be approximated as

$$B_{ii} \approx \frac{x_1}{D_{i1}^{\mathrm{MS}}} + \mathcal{O}(\epsilon) \tag{4.21}$$

From this expression and from eq 4.19 we finally find that

$$D_{i1}^{\mathrm{MS}} \cong \frac{x_1}{x_i}\Lambda_{ii} \cong \frac{\Lambda_{ii}}{x_i} \tag{4.22}$$

This equation indicates that the element that has a larger influence in the motion of a solute i is the friction with the more abundant solvent, as we may have guessed. From eq 4.6, we can obtain the terms D_{ij}^{MS}, for $j \neq 1$. However, to preserve the symmetry of the matrix of Maxwell-Stefan coefficients, we derive the expression from the sum of the two elements that contain D_{ij}^{MS}, namely, B_{ij} and B_{ji}. Then, using eq 4.22 and the off-diagonal elements in eq 4.20, one obtains the approximate expression

$$D_{ij}^{\mathrm{MS}} \approx \frac{(x_i + x_j)\Lambda_{ii}\Lambda_{ij}}{(x_i + x_j)\Lambda_{ij} + \frac{x_i^2}{x_1}\Lambda_{jj} + \frac{x_j^2}{x_1}\Lambda_{ii}} \qquad i, j = 2, \ldots, n; \quad i \neq j \tag{4.23}$$

The evaluation of the MS coefficients under dilute solution conditions is subject of a large uncertainty if obtained through the Onsager elements Λ_{ij}. Therefore, large error bars are expected due to the lack of representative elements in the averaging procedure (based on the motion of the baricenter of the species) and the oscillatory nature of the integrand, for the off-diagonal terms.

Finally, to increase the accuracy of the measure, we introduce here a formal simplification of the problem through the consideration of the brine as an effective solvent, as if it were a single species. In this approximation, it is implicitly considered that the relative composition of the constituents of the brine is not affected by the diffusion of the solute (CO_2, in our case). In this case, the evaluation of the Onsager matrix reduces to a 2 × 2 matrix, whose elements are calculated summing over all the species of the brine except CO_2 in eqs 4.9 or 4.10. One can verify that

$$\begin{aligned} \Lambda_{2b} &= \sum_{i \neq 2}^{n} \Lambda_{2i} \cong \Lambda_{21} \\ \Lambda_{bb} &= \sum_{\substack{i \neq 2 \\ j \neq 2}}^{n} \Lambda_{ij} \cong \Lambda_{11} \end{aligned} \tag{4.24}$$

where the subscript b stands for brine. The element Λ_{22} remains the same. Therefore, we have verified that in the dilute limit, this approximation is consistent with the more formal treatment.

As far as the diffusion coefficients are concerned, this approximation reduces the problem to the diffusion of CO_2 in the brine and, therefore, to one single Fick's and MS diffusion coefficients. Nevertheless, we have calculated the four elements of the CO_2-brine Onsager matrix for completeness.

In addition to the calculation of the Onsager coefficients Λ_{ij}, related to the diffusive processes, properties related to other irreversible processes can be also obtained using the corresponding Einstein and GK formulations. An interesting quantity to obtain through MD simulations is the electrical conductivity κ, for which experimental data are available in the literature to compare with the simulation results.[27] The Einstein and GK expressions for κ are the following (eqs 4.25,4.26):

$$\kappa = \frac{1}{6k_BTV} \lim_{t\to\infty} \frac{d}{dt} \left\langle \left(\sum_{i=1}^{N} q_i \vec{r}_i(t) - \sum_{j=1}^{N} q_j \vec{r}_j(0) \right)^2 \right\rangle \tag{4.25}$$

$$\kappa = \frac{1}{3k_BTV} \int_0^{\infty} \left\langle \left(\sum_{i=1}^{N} q_i \vec{V}_i(t) \right) \cdot \left(\sum_{j=1}^{N} q_j \vec{V}_j(0) \right) \right\rangle \tag{4.26}$$

4.2.2 Reorientational dynamics

The rotational dynamics of water and CO_2 molecules in brine can be analyzed through temperature-dependent reorientational relaxation times. For water, the H-H and O-H relaxation can be obtained from ^{1}H-^{1}H and ^{17}O-^{1}H dipole relaxation NMR experiments. The correlation function of the dipole moment of water is experimentally obtained from optical measurements (Raman scattering, fluorescence depolarization and Kerr experiments).[165] For CO_2, O=C=O relaxation can be determined by ^{13}C, and ^{17}O NMR longitudinal relaxation times in conjunction with microwave spectroscopy at a wide range of pressures and temperatures.[166–168] Depolarized Rayleigh scattering measurements have also been applied by Versmold to study the molecular reorientation of CO_2.[169]

We have also computed the reorientation correlation time of several unit vectors, $\vec{e}$, depending on the geometry of the molecule. In the case of water, three vectors are defined i.e., that joining the two hydrogen atoms (H-H), the dipole moment (μ), and a vector perpendicular ($\perp$) to the plane of the molecule. For CO_2, only the vector aligned to the C=O bond is considered. The orientational autocorrelation functions can be defined as,

$$C_i^l(t) = \langle P_l(\vec{e_i}(t) \cdot \vec{e_i}(0)) \rangle \tag{4.27}$$

where P_l is a Legendre polynomial with $l = 1, 2$ for the first and second order, respectively. These functions are commonly fitted to Kohlrausch-William-Watts exponential functions,[170,171]

$$C_{i,\mathrm{KWW}}^l(t) = \exp[(-t/\alpha_i^l)^{\beta_i^l}] \tag{4.28}$$

for which the relaxation time can be obtained through,

$$\tau_i^l = \int_0^\infty C_{i,\mathrm{KWW}}^l(t)dt = \frac{\alpha_i^l}{\beta_i^l}\Gamma\left(\frac{1}{\beta_i^l}\right) \tag{4.29}$$

4.2.3 Soreide & Whitson thermodynamic model for electrolyte solutions

The thermodynamic factor Q has been estimated through the Soreide & Whitson equation of state (EOS) model.[172] CO_2 fugacity coefficient ($\ln \varphi_1$) at a given composition is obtained at the bubble pressure as calculated by the EOS at the same pressure and temperature. To numerically compute the derivative in eq 4.7 we slightly vary the mole fraction by an increment of $\Delta x_1 = 10^{-5}$ to the actual mole fraction.

4.3 Computational Methods

Molecular dynamics simulations were performed using the DLPOLY v2.19 code. The different properties computed have been obtained by post-treatment of trajectories generated with this code. Both water and carbon dioxide were treated as rigid molecules using pair potentials composed of Lennard-Jones (LJ) and Coulombic terms. The SPC/E model[26] was used for water-water interactions as it correctly reproduces transport, thermodynamic, and structural properties of water better than other available models in the literature,[173] but also because it has been widely used for modeling aqueous ionic solutions.[27,174–177] Carbon dioxide was treated as a rigid molecule with a quadrupole charge using the EPM2 intermolecular potential.[28] Na/Cl atoms were also described by LJ interaction centers plus point charges to describe the electrostatic interactions with the rest of the molecules in the system. For the ions, we have used the optimized potential of Wheeler and Newman,[27] since it better reproduces the density ionic-aqueous solutions than the intermolecular model derived by Dang.[178] The LJ parameters for the different species are shown in Table 4.1 (for water molecules are given in Table 1.1).

Table 4.1: Intermolecular potential for the EPM2[28] model of CO_2, Na^+ and Cl^-.

	CO_2	
Bond distance (Å)	**d_{C-O}**	1.149
Atom (group)	**C**	**O**
M (g/mol)	12.0107	15.9994
ϵ (kJ/mol)	0.2339	0.6693
σ (Å)	2.757	3.033
q(e)	0.6512	-0.3256
	Ions	
Atom (group)	**Na^+**	**Cl^-**
M (g/mol)	22.9898	35.4530
ϵ (kJ/mol)	0.45980	0.45064
σ (Å)	2.350	4.420
q(e)	1.0	-1.0

The long-ranged electrostatic interactions were treated by the Ewald summation technique with a tolerance of 10^{-6} in the electrostatic energy. Crossed LJ interactions between the different force field centers were computed using the Lorentz-Berthelot mixing rules. The Verlet leapfrog algorithm has been used to integrate the equations of motion with a time step of 2 fs and a cut-off distance of 12.5 Å for all cases. A Verlet list with a second cut-off radius of 13.5 Å was used to improve CPU time. The rotational part of the equations of motion was integrated using the Fincham implicit quaternion algorithm[35] with a quaternion tolerance of 10^{-8}. All the MD simulations were carried out in cubic boxes with periodic boundary conditions. The number of water molecules for all the simulations was in the range of 3000-3200. The number of ions used in our simulations was determined by the molality concentration of the solution, and the number of molecules of CO_2 was determined by the saturation concentration at the desired temperature, pressure, and molality, according to the experimental values.[179] To determine the density of the mixture and, therefore, the box-size for the different systems, NPT simulations using the Nosé-Hoover thermostat-barostat were carried out before production runs. The relaxation times, τ_T and τ_P, controlling temperature and pressure fluctuations, are 0.1 and 1.0 ps, respectively. For equilibration and production runs, NVT-Nosé-Hoover ensemble was used with τ_T equal to 0.1 ps. For all the systems, the positions and the velocities for each atom on each molecule were stored every 20 time steps. To obtain the density of the mixture, NPT runs of $25 \cdot 10^4$ time steps were carried out. Equilibration runs were also done with $25 \cdot 10^4$ time steps while production runs were done with $75 \cdot 10^4$. Statistical uncertainties of the diffusion coefficient were estimated by using several runs starting from different independent initial conditions. We found values that are strongly dependent on the system's composition and on the nature of the coefficient (10-15 % for self-diffusion coefficients and 10-50 % for mutual diffusion).

Production trajectories were analyzed with the post-treatment code in order to compute MS diffusion coefficients trough eqs 4.5-4.6 and 4.9-4.13. Electrical conductivity is calculated through eqs 4.25 and 4.26, and rotational dynamics, through eqs 4.27 and 4.29. In order to validate the accuracy of the selected force fields, several simulations were done before considering the case of CO_2 in brine. Firstly, MS diffusivity of NaCl ions in water was determined at different molal concentrations and compared to both, simulation and experimental values.[27] Secondly, binary MS diffusion coefficient of CO_2 in water were computed and compared to the available experimental data in the literature, at atmospheric pressure and for several temperatures.[180–183] Due to the low solubility of CO_2 in water or in brine, all simulations were performed with the mole fraction of CO_2 greater or equal to 10^{-3}. This implies that one has, at least, 10 molecules of CO_2 on each simulation box, which is a small number. One important consequence of the low solubility of this gas in water at ambient conditions is the lack of statistical significance of the data, which is translated into large error bars in the evaluation of the terms $\Lambda_{CO_2-CO_2}$ and $\Lambda_{H_2O-CO_2}$, defined in eqs 4.9 and 4.10, even for quite long simulation runs (1.5 ns). This fact makes it difficult the comparison of simulation results with experiments at pressures close to the ambient. Additional calculations were done for MS diffusivity of CO_2 in water at different temperatures and pressures up to 1000 bar. In this region, the CO_2 mole fractions are of the order of 10^{-2}. The selected thermodynamic conditions of the different systems studied are summarized in Table 4.2, 4.3, and 4.4.

As a first approximation, for the CO_2 dissolved in pure water, especially at ambient conditions, we have that the thermodynamic factor is approximately equal to 1, since the mole fraction of CO_2 is very small in all the systems analyzed. Consequently, the binary Fick diffusion coefficient can directly be approximated by the MS diffusivity and thus compared to the available experimental data for this property at ambient pressure. Otherwise, one can use the equation 4.19 valid in the dilute limit. Unfortunately, experimental data for diffusion coefficients at pressures higher than the atmospheric pressure are lacking. Instead, as we are not far from infinite dilution of CO_2 in water, we can use a widely known correlation to estimate the diffusivity in non-electrolyte solutions to later compare our simulation results at higher pressures. The correlation used is the Wilke-Chang equation,[184]

$$D^0_{AB} = 7.4 \cdot 10^{-8} \frac{(\phi M_B)^{1/2} T}{\eta_B V_A^{0.6}} \tag{4.30}$$

where D^0_{AB} is the mutual diffusion coefficient of the solute A at very low concentration in the solvent B, M_B is the molecular mass of solvent B, T is the temperature, η_B is the viscosity of the solvent, V_A is the molar volume of the solute at its boiling point, and ϕ is a dimensionless parameter referred to as association factor. If the solvent is water, the recommended value for ϕ is 2.26.[185] The molar volume V_A can be estimated using the Tyn and Calus method:[186]

$$V_A = 0.285 V_C^{1.048} \tag{4.31}$$

where V_C is the critical molar volume.

Simulated electrical conductivity for CO_2-brine mixtures at some thermodynamic conditions were compared to a correlation from Fleury and Deschamps.[187] Fleury and Deschamps proposed the following relationship describing the effect of dissolved CO_2 on electrical conductivity κ of aqueous NaCl solutions.

$$\kappa_S(x_{\mathrm{CO_2}}, T) = \kappa_S(0, T_0)(1 - 6x_{\mathrm{CO_2}}) \left(\frac{T + 19.5}{T_0 + 19.5} \right) \tag{4.32}$$

where $\kappa_S(0, T_0)$ is the electrical conductivity of aqueous NaCl solution at a reference temperature T_0 when $x_{\mathrm{CO_2}}$ is equal to zero. This equation is valid if the temperature ranges between 35°C and 100°C.

Finally, to the best of our knowledge, there is no experimental data to compare to for reorientational dynamics of CO_2 dissolved neither in water nor in brine.

4.4 Results and discussion

4.4.1 Validation of the intermolecular potentials

4.4.1.1 Calculation of MS diffusion coefficients of the ions and the electrical conductivity of brine

To test the accuracy of the Na/Cl and water intermolecular potentials, we performed NPT MD simulations for aqueous NaCl solutions at different salt concentrations to compute solution densities, MS diffusion coefficients and electrical conductivity. The MD simulation results were compared to simulation results of Wheeler and Newman[27] and experimental data based on Chapman's fits of a compilation of experiments.[188] First of all, and before adopting a set of LJ parameters for ions, NPT MD simulations at $T = 298.15$ K and $P = 1.01325$ bar were performed in order to obtain solution densities. The first set of LJ parameters were those of Dang[178] and the second were the LJ parameters provided by Wheeler and Newman.[27] Three salt concentrations were chosen: 1, 2.5, 4 molal.

Figure 4.1 gives the simulated and experimental electrolyte solution densities as a function of molal concentration. We can observe that all force fields accurately reproduce the experimental solution densities for low salt concentrations within the error bars. At high salt concentrations (4m), however, simulations using the Wheeler and Newman (WN) parameters reproduce better the experimental solution density than the Dang's model. Hence, we decided to choose the WN potential to simulate Na^+ and Cl^- ions.

MS diffusion coefficients were calculated using the Einstein and GK formulations yielding the adequate Onsager's matrices Λ_{ij}, defined in eq 4.9. As shown in Figure 4.2, for the cases Na-H_2O and Cl-H_2O, the obtained diffusion coefficients compare well with the earlier simulation results given by Wheeler and Newman,[27] although the latter are in semi quantitative agreement with experimental data. Only $D^{\mathrm{MS}}_{\mathrm{Na^+-H_2O}}$ for a concentration of 4 molal, presents a significant deviation with respect to the experimental data larger than the 25%. As discussed in section 4.2.1, $D^{\mathrm{MS}}_{\mathrm{Na^+-H_2O}}$ and $D^{\mathrm{MS}}_{\mathrm{Cl^--H_2O}}$ are the more relevant coefficients for the system since are related to the friction of the ion with the surrounding solvent. For completeness, we also estimate $D^{\mathrm{MS}}_{\mathrm{Na^+-Cl^-}}$ despite the small value and the large uncertainty of the data. Thus, we cannot be conclusive with the opposite trend observed for this magnitude with respect to the salt

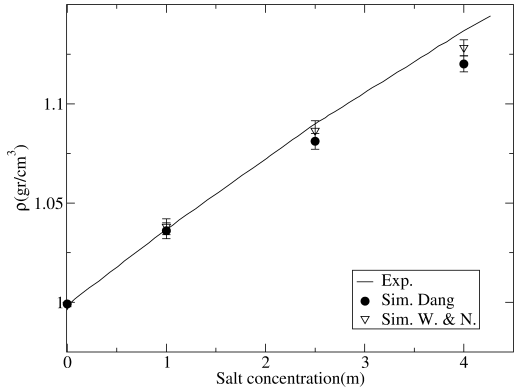

Figure 4.1: Simulated and experimental solution densities as a function of salt concentration. Dark circles and empty triangles correspond to solution densities calculated using Dang[178] and Wheeler and Newman[27] potentials for ions, respectively. Experimental data from ref [188].

concentration as compared to the experimental data. We have also verified that the mass balance constraint (eq 4.11) was satisfied (the computed value is of the order of 10^{-4}, which is acceptable considering the large fluctuations observed in the calculations of the elements of the Onsager matrix $[\Lambda]$). Full comparison of the obtained MS diffusion coefficients either using GK or Einstein formulations with experimental data and Wheeler and Newman simulations is given in the Table A.1 of the Appendix.

The last property calculated for our validation test was the electrical conductivity κ. Our simulation results are shown in Table 4.2 and in Figure 4.3. Simulations under predict the experimental conductivity mainly for high salt concentrations. This trend was also observed by Wheeler and Newman.[27] Electrical conductivity is a property that is precisely very sensitive to ion-ion interactions. Together with the previous results on the MS diffusion coefficients, the values obtained for the electrical conductivity confirm that it is likely that the chosen potentials for water and ions imply either too strong ion-ion interactions or too weak H_2O-ions interactions. The polarizability of water and ions at high ion concentration, disregarded in the models used along this work, can be the origin of the observed discrepancies, although this analysis lies outside the scope of the present work.

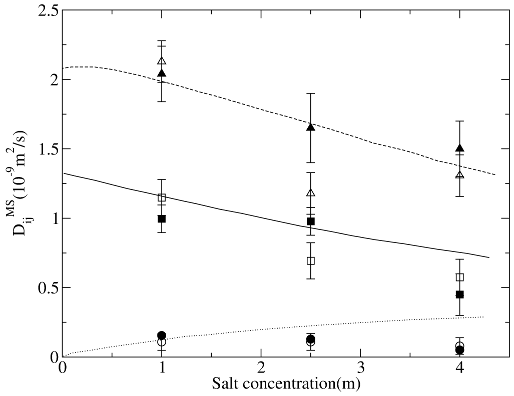

Figure 4.2: Simulated and experimental MS diffusion coefficients for Na-Cl-water systems as a function of salt concentration. Lines correspond to experimental data, empty symbols correspond to the simulated MS diffusion coefficients obtained by Wheeler and Newman,[27] while full symbols correspond to our calculation using GK formulation. Circles and dotted line correspond to Na-Cl results, squares and solid line correspond to water-Na results while triangles and dashed line correspond to water-Cl results.

Table 4.2: Comparison of the simulation results for the electrical conductivity for Na-Cl-water systems at different salt concentrations and 298.15 K with the experimental data and simulation results of Wheeler and Newman.

conc. (m)	N_{ions}	κ exp. (S/cm)	κ calc. GK / Einst.(S/cm) /dev. exp.	κ calc. Wheeler & New. (S/cm) /dev. exp.
1	54	0.076	0.085/0.082	0.073
			11.8%/7.9%	4.0%
2.5	135	0.159	0.137/0.117	0.104
			13.8%/26.4%	34.6%
4	216	0.212	0.159/0.158	0.119
			25.0%/25.5%	43.9%

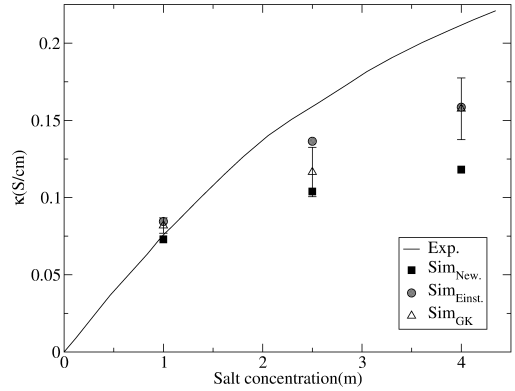

Figure 4.3: Simulated and experimental electrical conductivities for Na-Cl-water systems as a function of salt concentration. Dark squares correspond to the simulation results of Wheeler and Newman,[27] while grey circles and empty triangles correspond to our calculation using Einstein and GK formulations respectively.

4.4.1.2 Calculation of MS diffusion coefficients for CO_2-water mixtures

We have computed the MS diffusion coefficient of CO_2 in water at different thermodynamic conditions in order to explore the accuracy of the EPM2 potential for CO_2 with regard to this property. In a first step, we performed NVT MD simulations with a simulation pressure $P = 1.013$ bar (atmospheric pressure) and $T = 283.15$, 298.15 K. Experimental data at atmospheric pressure are available in the literature.[189,190] The number of molecules of CO_2 to be introduced in the simulation box was determined from experimental data on the saturation concentration at the desired temperature and pressure. As the CO_2 mole fraction is very small under the conditions of interest, three MD simulations, taking different initial conditions, were performed in order to average the obtained MS diffusion coefficient and to reduce the statistical uncertainty. As we are at low pressure and small solute mole fraction, the binary Fick diffusion coefficient for CO_2 can be well approximated by the corresponding MS coefficient, since the thermodynamic factor Q is almost 1 under these thermodynamic conditions (it is calculated as 0.991 at 283.15 K and 0.994 at 298.15 K). Diamond et. al. have recently estimated using a large collection of experimental data that this assumption is correct if the mole fraction of CO_2 is below 2%.[191] Hence, as it follows from eq 4.8 and eq 4.19, $D_{22} \cong \Lambda_{22}/x_2 \cong D_{21}^{\mathrm{MS}}$. This equation indicates that, on the one hand, in dilute solution the Fick diffusion coefficient is approximately given by the self-correlation function of the solute and, on the other, that the friction (represented by the inverse of the MS coefficient) is that of the solute with the solvent.

The thermodynamic conditions and simulation results are shown in Table 4.3. Despite the statistical uncertainty due to the small CO_2 mole fraction, we can consider that our simulation results are in rather good agreement with the experimental data. For the case of 298.15 K, we obtained, however, a non negligible deviation of 25% from the experimental value which is an acceptable result considering the small number of CO_2 molecules and the length of the simulation; 1.5 ns.

Table 4.3: Comparison of the simulation results for the MS diffusion coefficient for CO_2-water systems at $P = 1.013$ bar and different temperatures with the experimental data in the literature.[189,190] The simulation data is obtained through NVT simulations after NPT simulations at $P = 1.013$ bar have been used to determine the actual density.

T(K)	$N_{\mathrm{CO_2}}$	N_{w}	ρ_{avg} (g/cm^3)	D_{22} exp. (10^{-9} m^2/s)	D_{22} calc. GK / Einst. (10^{-9} m^2/s) dev. exp.
283.15	3	3175	1.005	1.46	1.83/1.82 24.7%/25.3%
298.15	2	3250	0.998	1.98	1.98/2.04 0%/3.0%

Uncertainty could be reduced by increasing the size of the system keeping the density constant, but our system already lied on the limit of a reasonable use of the computational resources (20 molecules of CO_2 correspond to 32500 molecules of water). However, due to the fact that the system is diluted and that we expect the solute-solute interactions to be small, one can increase the number of CO_2 molecules by increasing the pressure of the system up to 1000 bar (yielding a ratio of about 100 CO_2 molecules to 3000 water molecules), without significantly affecting the dynamic results. Due to the lack of experimental data to compare to, we have used the well known Wilke Chang correlation[184] to obtain an estimate of the diffusion coefficients at the selected temperatures and pressures (see eq

4.30). The Wilke-Chang correlation gives, however, the diffusion coefficient at infinite dilution. In our simulations, the CO_2 mole fractions are always less than or equal to 10^{-2}, and therefore we are under the conditions of validity of the Wilke-Chang correlation. Thermodynamic conditions, and simulation results as compared to Wilke-Chang predictions are shown in Table 4.4. For the estimate of the latter, viscosities of water at the different thermodynamic pressures and the molar volume of CO_2 at its boiling point were obtained from the NIST data base.

Table 4.4: Comparison of the simulation results for the MS diffusion coefficient for CO_2-Water systems at $P > 1.013$ bar and different temperatures with the Wilke-Chang correlation.[184]

T(K)/ P(bar)	N_{CO_2}	ρ_{avg} (gr /cm^3)	D_{22} WCh (10^{-9}m^2/s)	D_{12}^{MS} calc. GK/Einst. (10^{-9}m^2/s) /dev.exp	Q_{22}	D_{22} calc. GK/Einst. (10^{-9}m^2/s)
303.15/100	73	1.014	2.19	2.55/2.80 16.4%/27.8%	0.768	1.96/2.15
303.15/1000	120	1.060	2.16	1.90/1.87 12.0%/13.4%	0.644	1.22/1.20
333.15/100	55	0.990	4.09	3.40/3.30 16.9%/19.3%	0.815	2.77/2.69
333.15/1000	103	1.037	3.90	2.85/2.76 26.9%/29.2%	0.679	1.93/1.87

In general, we observe that the MS as well as Fick diffusivities increase when increasing the temperature and decrease when increasing the pressure. This was the intuitively expected trend, also followed by the diffusion coefficients obtained from Wilke-Chang correlation. However, the correlation data show that there is not a strong dependence of the diffusion coefficient with pressure, due to the fact that the density is the most important factor at constant temperature. At very high pressure the local structure of water is furthermore altered and thus it affects the diffusivities, although this factor seems to have only a weak effect in the range of pressure studied. On the other hand, in our simulations there is a reduction of about 15-30% of the MS coefficient when the pressure is increased from 100 bar to 1000 bar. This fact can be the consequence of an overestimation of the CO_2-H_2O interactions. In fact, Lisal et al. have noticed that the CO_2 solubility in water obtained with EPM2 and SPC/E model overestimates the experimental values.[192] These authors attribute this behavior to a too strong CO_2-H_2O interaction. Anyway, in the comparison of the Wilke-Chang diffusivities with the simulated MS diffusivities, the average deviation is in average about the 17%. However, the estimated values for the Fick diffusion coefficients from our simulations are in larger disagreement with the Wilke-Chang correlation, except for the initial value, at 303.15 K and 100 bar. The fact that the Wilke-Chang does not contain any dependence in activity coefficients suggests that these values should better follow the trends of the MS diffusivities than Fick's diffusivities, as we observe.

4.4.2 Study of CO_2-brine mixtures

Once the accuracy of chosen potentials for different species were checked, we can proceed to the simulation of the CO_2-brine mixtures. We have performed MD simulations at thermodynamic conditions representative of deep saline aquifers. Temperature ranges from 333.15 K to 453.15 K and pressure from 50 to 500 bar. Three Na/Cl molal concentrations were chosen; 1,2, and 4 m. The number of CO_2 molecules at each thermodynamic condition is given in Tables A.3-A.11 of the Appendix, and ranges from about 10 molecules at lower pressure to 100 at the higher pressures. The corresponding CO_2 mole fractions range from 10^{-3} to $3 \cdot 10^{-2}$. It is important to bear in mind that, according to experiments, the CO_2 mole fraction increases by increasing the pressure and by decreasing salt concentration. As a result, for the lowest pressure and the higher salt concentration cases, larger error bars are expected for thermophysical properties in comparison with cases with larger x_{CO_2}.

4.4.2.1 Calculation of solution densities of CO_2-brine mixtures

In order to obtain solution densities of the mixtures for the different P and T thermodynamic conditions, NPT MD simulations were performed. Figure 4.4 gives the simulated densities of the mixture CO_2+brine as a function of pressure for all considered temperatures and salt concentrations. Simulation results show that solution densities increase by increasing the pressure and salt concentration and decrease by increasing temperature. These are all expected trends. Only a few studies measuring solution densities of CO_2+brine systems can be found in the literature. For instance, Li et al.[22] measured densities for binary systems of CO_2+Weyburn formation brine at a temperature of 332.15 K and pressures similar to those of our study. Weyburn formation brine contains more dissolved species than present in our simulations, like calcium, magnesium or potassium. In this case, sodium and chloride ions are the major ionic species, with molal concentrations of 1.27 m and 1.48 m, respectively, with a measured solution density, at 333.15 K and 101.4 bar, equal to 1.0555 g/cm^3. Simulation results at a similar temperature and pressure (333.15 K and 100 bar) and salt concentrations (1 m and 2 m) yield 1.0232 g/cm^3 and 1.0538 g/cm^3, respectively. If we considered Na/Cl salt concentrations similar to those present in Weyburn formation brine, we would expect a CO_2-brine solution density around 1.039 g/cm^3. However, as we said before, Weyburn formation brine contains also species with larger molecular masses than Na^+ and Cl^-. Hence, a larger solution density than in our simulation is expected when comparing with experimental data.[22]

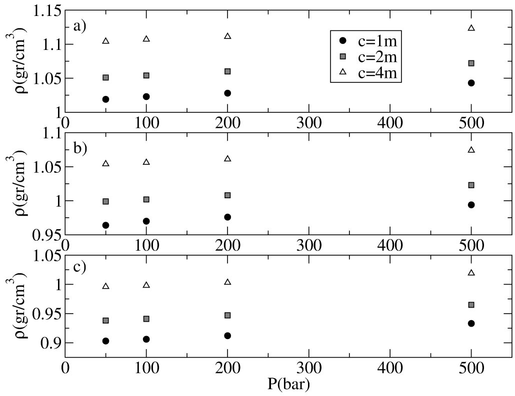

Figure 4.4: Simulated solution densities for CO_2-brine systems at a) $T = 333.15$ K, b) $T = 393.15$ K and c) $T = 453.15$ K as a function of pressure and for different salt concentrations.

4.4.2.2 MS diffusion coefficient of CO_2 in brine

Ms diffusion coefficients at selected thermodynamic conditions were obtained using both Einstein and GK formulations. Once the NVT MD simulations were performed, trajectories were post-treated obtaining the different MS diffusivities. To reduce the uncertainty of the results, two simulations were carried out at each thermodynamic condition and final MS diffusivities were obtained by averaging the two values obtained after post-treatment. As indicated in 4.2.1, the MS diffusion coefficient of CO_2 in such brine is obtained from the computation of Λ_{22}, according to eqs 4.9 (conversely, 4.10) and 4.22. In the following we analyze the more relevant trends.

a. Temperature dependence of MS diffusion coefficients

MS diffusivity of CO_2 in brine was obtained as a function of temperature for different pressures and salt concentrations. Simulation results at 100 bar and 200 bar using Einstein relations are shown in Figure 4.5. Data are listed in Tables A.3-A.11 of the Appendix. For all pressures, MS diffusivities increase with temperature, which was the expected trend. However, from the simulation results, we cannot conclude that MS diffusivities have a clear dependence on salt concentration. However, Figure 4.5 may suggest that D_{2b}^{MS} at $c = 1$ m is larger than for $c = 2$ and 4 m, nevertheless, this trend was not observed for pressures equal to 50 and 500 bar (results not shown). Due to the low concentration of solutes, as well as the non-charged and quadrupolar nature of CO_2 interaction with the ions, it is expected a weak dependence of the MS diffusion coefficient with ion concentration at the studied conditions. Furthermore, our results are affected by large error bars due to the fluctuations of the simulated variable. In some cases, we observe a relative dispersion of our data on the D_{2b}^{MS} as much as 25%. This situation occurs especially at low pressures and at high temperatures.

In fact, one has to take into account that we set the number of CO_2 molecules for each thermodynamic condition from solubility experimental data. Then, if we fix the salt concentration and the pressure, the evolution of D_{2b}^{MS} with temperature involves calculations with different number of CO_2 molecules for each temperature However, since the system is very dilute for the CO_2 and the difference between CO_2 mole fractions along the simulations are small in all conditions, we do not expect any influence of the CO_2 concentration on D_{2b}^{MS}.

The calculation of the thermodynamic factor Q for all studied conditions shows values that are greater than 0.78, as can be seen in Figure 4.6, which means that the CO_2 behaves almost ideally from a thermodynamic point of view and, therefore, the Fick diffusion coefficient D_{22} is very close to the MS diffusion coefficient although slightly smaller (results given in Tables A.3-A.11 of the Appendix). Consequently, from now on, we will only discuss the behavior of the MS diffusion coefficient.

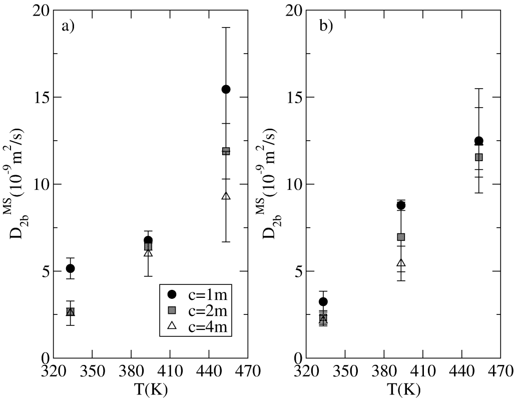

Figure 4.5: Simulated MS diffusion coefficients of CO_2 in brine as a function of temperature at a) P = 100 bar and b) P = 200 bar and for different salt concentrations. Results were obtained using Einstein formulation (eq 4.9, together with eq 4.22.

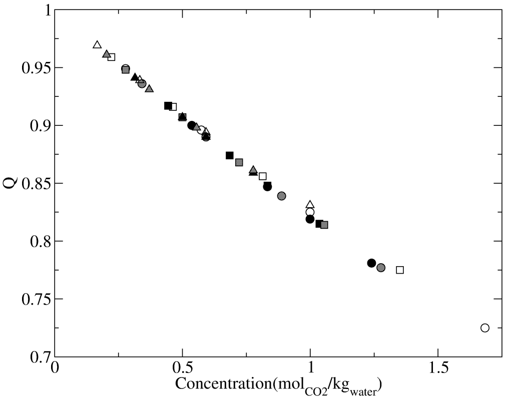

Figure 4.6: Variation of the thermodynamic factor Q of CO_2 in brine in function of the temperature, pressure and salt concentration. Full symbols correspond to T = 333.15 K, grey symbols to T = 393.15 K, and empty symbols to T = 453.15 K. Circles correspond to c = 1 m, squares to c = 2 m, and triangles to c = 4 m.

b. Dependence of MS diffusion coefficients with pressure, CO_2, and salt concentration

In Figure 4.7 we observe that the D_{2b}^{MS} does not significantly depend upon the pressure under the conditions studied. Notice that this statement can be done due to the fact that the solution is dilute and no interactions between solute molecules is expected. Thus, although the number of CO_2 molecules changes, the whole variation of D_{2b}^{MS} with the pressure would be caused by the structural changes at the local scale induced by change of pressure.

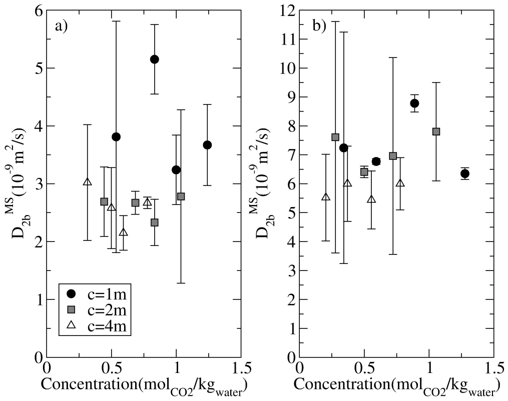

Figure 4.7: Simulated MS diffusion coefficients of CO_2 in brine as a function of CO_2 concentration at a) $T = 333.15$ K and b $T = 393.15$ K and for different salt concentrations. Results were obtained using Einstein formulation.

Again, due to the high dilution for both CO_2 and NaCl, it is expected a weak effect of the salt concentration on the CO_2 diffusivity.

4.4.2.3 Electrical conductivity of CO_2-brine mixtures

Together with the inherent interest of the electrical conductivity of these CO_2-brine mixtures, the evaluation of this quantity is affected by lower error bars than D_{2b}^{MS} and, therefore, it constitutes a good test of the accuracy of the simulations as well as of the predictive behavior of the potential used for the CO_2. We hence proceed to the analysis of this property.

Figure 4.8a gives the simulated electrical conductivity as a function of temperature at $P = 100$ bar for different salt concentration using Einstein formulation. As observed for D_{2b}^{MS}, the electrical conductivity increases with increasing temperature. This effect has been observed for all pressures. Such a behavior is expected in view of the decrease of the viscosity of the solution (mostly water) with increasing temperature. Thus the mobility of the charge carriers increases inversely proportional.

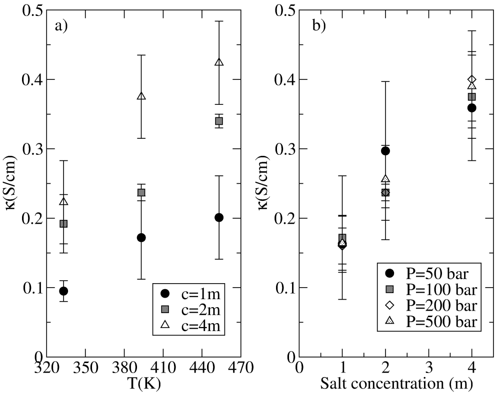

Figure 4.8: Simulated electrical conductivity for CO_2-brine mixtures as a function of temperature at $P = 100$ bar for different salt concentrations (Fig. 4.8a), and simulated electrical conductivity for CO_2-brine mixtures as a function of salt concentration at $T = 393.15$ K (Fig. 4.8b) for different pressures. Results were obtained using Einstein formulation.

As expected due to the increase of the charge carriers in the solution, the electrical conductivity increases by increasing salt concentration, as shown in Figure 4.8b. This trend can be clearly observed for all pressures, even for $P = 50$ bar, where a large dispersion in the values of the MS diffusivities was obtained. No pressure-dependence for electrical conductivity is observed from simulation results inside the range of certainty. The effect is weak in the high dilution limit of the dissolved CO_2. Effectively, the decrease of the conductivity with the pressure should be proportional to the decrease of the mole fractions of the conducting species due to the increase of the dissolved gas in the system. This effect would dominate over any other effect on the structure of a rather incompressible fluid due to the pressure in the range of pressures studied. Simulated electrical conductivities at $T = 333.15$ K and at salt concentration equal to 1 m and 2 m can be compared to the values using Fleury-Deschamps correlation (see eq 4.32), which reflects such a decrease of the conductivity with the increase of the pressure.

The comparison between electrical conductivity as a function of x_{CO_2} obtained with our simulations and the Fleury-Deschamps correlation can be observed in Figure 4.9. Simulation results shown in Figure 4.9 have a mean deviation of 18% with respect to the data obtained with the aforementioned correlation, which systematically gives larger values of the conductivity as compared to the simulations. The underestimation of the simulation results could arise from subtle details of the intermolecular potentials, probably from the fact that the SPC/E model might not be able to correctly describe the water-ions dynamic behavior, particularly at high salt concentrations. Despite the large error bars, the simulation results are systematically lower than the correlation.

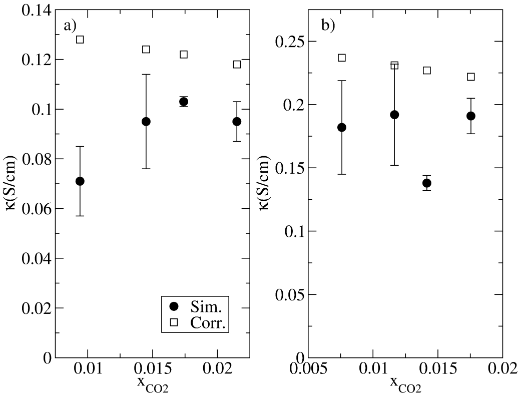

Figure 4.9: Comparison between simulation and correlation data for electrical conductivity as a function of CO_2 concentration at $T = 333.15$ K and $c = 1$ m (Fig. 4.9a) and $c = 2$ m (Fig. 4.9b). Simulation data was obtained using Einstein formulation and correlation data from eq 4.32.

4.4.2.4 Rotational relaxation time of CO_2 and water in brine

The last property analyzed was the relaxation dynamics of water and CO_2 molecules from the dynamic behavior of several vectors defined in section 4.2.1. The variation of the relaxation times $\tau^{1,2}_{\mathrm{H-H}}$, $\tau^{1,2}_{\mu}$, and $\tau^{1,2}_{\perp}$, as defined in eq 4.29, with the temperature at different salt concentrations at 100 bar can be observed in Figure 4.10, and the data are listed in the Appendix, Tables A.14-A.16. We have chosen a fixed pressure to perform our calculations since neither D_{2b}^{MS} nor any of the rotational relaxation times for CO_2 seem to be a function of pressure, according to our results of the previous section. We can notice that $\tau_\mu^1 > \tau_{\mathrm{H-H}}^1 > \tau_\perp^1$, and $\tau_{\mathrm{H-H}}^2 > \tau_\mu^2 > \tau_\perp^2$ for all conditions investigated. The same ordering is observed in liquid water at standard conditions.[90,193] We also observe that all relaxation times increase when temperature decrease or salt concentration increases.[176,194] In fact, when temperature is kept constant, all relaxation times are almost linear functions of salt concentration (figure not shown). From Figure 4.10 we have extracted, by means of an Arrhenius fitting ($\tau = A\exp(\Delta E/k_BT)$), the activation energy (ΔE) for the three different relaxation times. On one hand, $\Delta E_{\mathrm{H-H}}$($\approx$ 14.7 kJ/mol) and $\Delta E_\perp$($\approx$ 13.8 kJ/mol) are weakly affected by ion concentration. On the other hand, ΔE_μ clearly increases with salt concentration($\approx$ 13 to 15 kJ/mol). This fact is expected since τ_μ reflects the relaxation time of the dipole moment of water molecules, which are strongly perturbed by the increment of ion concentration.

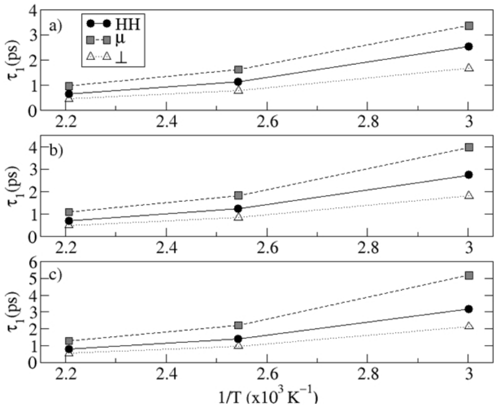

Figure 4.10: Variation of relaxation times of the different vectors defined for water molecules as a function of temperature and salt concentrations at 100 bar and at $c = 1$ m (Fig 4.10a), $c = 2$ m (Fig 4.10b), and $c = 4$ m (Fig 4.10c). Only results for the Legendre polynomial of grade 1 are shown.

Finally, the relaxation time of the bond vector for CO_2 at different temperatures and salt concentrations can be seen in Figure 4.11. We can observe an increase of the relaxation time with the decrease of the temperature. Like in water molecules, $\tau_{\mathrm{C=O}}$ also increases with the salt concentration reflecting the overall slowing down of the dynamics of the system.

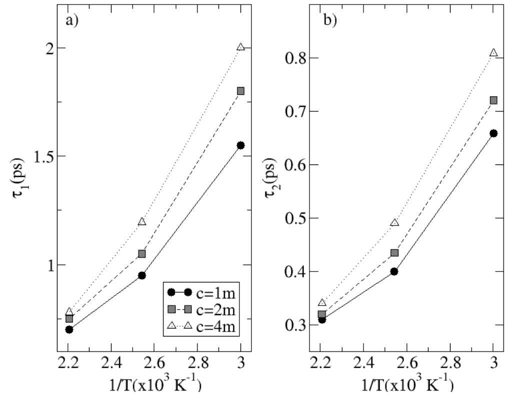

Figure 4.11: Variation of the relaxation time for the C=O bond vector as a function of temperature and salt concentration at 100 bar. Results from the Legendre polynomial of grade 1 (left, Fig 4.11a) and 2 (right, Fig 4.11b).

4.4.2.5 Prediction of the Maxwell-Stefan mutual diffusion coefficients of CO$_2$ in brine from rotational relaxation times and self-diffusivity data

We have seen so far that the main problem in computing the MS diffusion coefficient of CO$_2$ in water (either experimentally or by computer simulation) is its low solubility. The small number of molecules makes that the baricenter of the CO$_2$ strongly fluctuates in the derivation of the appropriate Onsager coefficient, according to eq 4.9. In this section, we will propose an alternative way to estimate D_{2b}^{MS} in brine from the measurement of the rotational relaxation time and, ultimately, from state variables of easy access.

Together with the direct determination of the diffusion coefficient, one can estimate D_{2b}^{MS} by using several correlations such as that of Darken

$$D_{2b}^{\mathrm{MS}} = x_2 D_b^{\mathrm{self}} + x_b D_2^{\mathrm{self}} \cong x_b D_2^{\mathrm{self}} \tag{4.33}$$

where D_i^{self} stands for the self-diffusion coefficients of species i.[195] The second is valid in the limit of high dilution of CO_2. One also has the Cadwell and Babb approximation for D_{2b}^{MS}, which relies on a linear combination of the diffusion coefficient of species i evaluated at infinite dilution, namely D_i^{∞} ($D_{2b}^{\mathrm{MS}} = x_2 D_b^{\infty} + x_b D_2^{\infty}$).[196] It is known that the Darken's relation gives a reasonable prediction of the mutual diffusion coefficient, particularly when one component is close to the infinite dilution, which is the case of CO_2 in brine. This is in agreement with what we have derived in our analysis of section 4.2.1. In this sense, the Cadwell and Babb relation neglects the fact that the MS diffusion coefficient is usually non ideal in water solutions at low solute concentrations[25] and, therefore, its use for estimation purposes is not suitable. On the one hand, to the best of our knowledge, there is no other correlation or approach that can be used to estimate of the MS diffusion coefficient of CO_2 in brine.

However, the use of the Darken relation translates the problem of the estimate of the diffusion coefficient to the estimate of the self-diffusion coefficient. Experimentally, self-diffusion coefficient (D_i^{self}) and rotational relaxation times can be measured by Proton magnetic resonance (^{1}H-MR) for water and Spin-lattice NMR for $^{13}CO_2$. However, we have not been able to find any data on these properties to straightforwardly make the estimate using the Darken relation and to compare to our simulation results. Hence, in this section we propose an alternative route using the information on the rotational relaxation times, or the calculated self-diffusion coefficients (given in Tables A.3-A.11 of the Appendix) in order to predict D_{2b}^{MS} at different thermodynamic conditions.

To derive this correlation, firstly we recall that the rate of rotational relaxation is commonly explained by using the viscosity-dependence and the orientational correlation time, τ_R, which is given by the well-known Debye-Stokes-Einstein (DSE) relation[197]

$$\tau_R = \frac{C_R \eta v_s}{k_B T} \tag{4.34}$$

where v_s is the specific volume of the solute molecule, C_R is a constant equal to 3 in the DSE theory but left in general as a fitting constant, and η is the viscosity of the solvent. From eq 4.34 we can see that τ_R/η is a constant for a particular solute-solvent pair. It was suggested that the rotation of a probe molecule in a viscous liquid should be coupled to the structural relaxation of the surrounding solvent,[197] thus, in this sense, it is analogous to the self-diffusion. Starting from the Stokes-Einstein (SE) relation it is known that the translational diffusion of one solute molecule (D_i^{self}) may also be expressed in terms of solvent viscosity

(η) and the radius of the molecule (R), according to

$$D_i^{\text{self}} = \frac{k_B T}{C_T \eta R} \tag{4.35}$$

Here, C_T is another constant. A direct relation can be then expressed between eqs 4.34 and 4.35, as follows,

$$\tau_R D_i^{\text{self}} = \frac{C_R v_S}{C_T R} \tag{4.36}$$

which depend only on constants and geometric dimensions of the molecule. In ref [197] the author found a microscopic expression for the constant in eq 4.36 relating them to dynamic structure factors obtained from mode coupling theory. Notice that this equation does not depend on the solvent viscosity and that it can be generalized to different dissolved gas molecules with the only condition of low concentration (infinite dilution). We should mention, however, that such an approximation is only valid on relatively dense systems (liquids), where the relaxation dynamics of the dissolved molecule is governed by the friction with the surrounding medium. We thus use 4.36 to determine C_R and C_T for CO_2 dissolved in brine using our simulation results of $D_{CO_2}^{\text{self}}$ and $\tau_{C=O}$. The advantage of this procedure is that the self-diffusion coefficient of CO_2 shows less statistical fluctuation than the MS diffusion coefficient since the independent molecules all contribute to the statistics instead of only the baricenter (see Tables A.3-A.11 in the Appendix). We have also assumed that CO_2 has no other relaxation time than $\tau_{C=O}$. Then, from the more precise evaluation of the self-diffusion coefficient as well as the rotational relaxation time, the unknown constants can be fitted, according to a linear function of the density

$$\tau_{C=O}^{l} D_{CO_2}^{\text{self}} \frac{R_{CO_2}}{v_{CO_2}} = \frac{C_R}{C_T} = (a_1(l) + a_2(l)\rho) \tag{4.37}$$

where l is the order of the associated Legendre polynomial (i.e., $l = 1, 2$), a_1 and a_2 are constants and ρ is the system density (in g/cm^3). Here we have used the fact that the product $\tau_{C=O}^{l} D_{CO_2}^{\text{self}}$ depends only on the system density[198,199] and structural properties of the molecules, which of course remain constant. In the determination of the coefficients of eq 4.37 we have used $v_S = 29.1936 \cdot 10^{-30}$ m^3 and $R_{CO_2} = 1.9101 \cdot 10^{-10}$ m, which are the molar volume and hydrodynamic radius of the EPM2 model of CO_2 respectively. Details of the fitting procedure of eq 4.37 and estimation of v_S and R_{CO_2} are available in the Appendix. In order to estimate $D_{CO_2}^{\text{self}}$ with eq 4.37 we need to express the variation of the rotational relaxation of CO$_2$ in function of temperature and salt concentration (c in molal). This was done by an Arrhenius fitting of the $\tau_{\mathrm{C=O}}$ data shown in Figure 4.11. We obtain for a salinity of 1 m$< c <$ 4 m and $T <$ 453.15 K,

$$A(l,c) = a_3(l)c^{a_4(l)} \tag{4.38}$$

and

$$\Delta E(l,c) = a_5(l)\ln(c) + a_6(l) \tag{4.39}$$

again, a_i ($i = 3, 4, 5,$ and 6) are constants which depend on the associated Legendre polynomial. Parameters a_i are shown in Table 4.5.

Table 4.5: Coefficients a_i obtained for equations 4.37, 4.38, and 4.39.

Coefficient	l	Value	units
a_1	1	18.444	dimensionless
	2	8.8153	dimensionless
a_2	1	-14.042	cm^3/g
	2	-6.9448	cm^3/g
a_3	1	0.0749	s^{-1}
	2	0.0365	s^{-1}
a_4	1	-0.1877	dimensionless
	2	-0.1284	dimensionless
a_5	1	1.061	kJ/mol
	2	0.804	kJ/mol
a_6	1	8.378	kJ/mol
	2	7.942	kJ/mol

Eq 4.37, together with eqs 4.38 and 4.39 permit to find an estimate of the self-diffusion coefficient of CO$_2$ in brine in terms of the rotational relaxation time and state variables. We have finally used the predictions of eq 4.37 for the self-diffusion coefficient into eq 4.33, and compared the results with the mutual diffusion coefficient of CO$_2$ in brine obtained from simulations, at all temperatures and salt concentrations in Figure 4.12. We observe a general good agreement between the values simulated and predicted, with an absolute deviation of about 15.4% for the MS diffusion of CO$_2$. Recently, Yeh et al. proposed a correlation to correct the results for the self-diffusion coefficient for the finite size effect unavoidable in common molecular dynamics simulations.[200] We did not correct our simulation results for this effect however, since we have used a quite large number of particles (at least 3000 water molecules). We

estimate that our reported values for self-diffusion may be under predicted by a maximum 6.5%. Therefore, the general good agreement of the correlation may suggest that the direct evaluation of the MS diffusion coefficients at high dilution strongly deviates from what is expected, in view of our previous analysis.

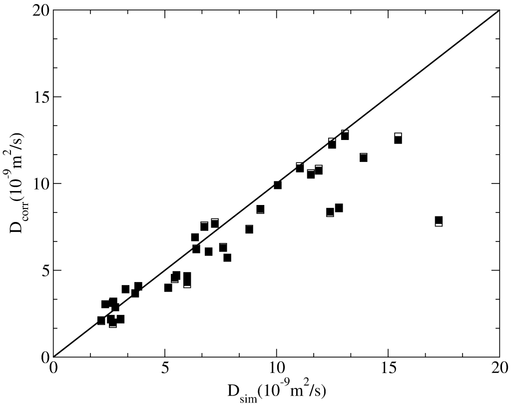

Figure 4.12: Comparison of the MS diffusion coefficient, D_{2b}^{MS}, obtained with the correlation of eq 4.33 (with $l = 1$, full symbols, $l = 2$ empty symbols) with the simulation results for the MS diffusion coefficient using Einstein formulation. The points that deviate from the line $D_{2b}^{\mathrm{MS}}(\mathrm{sim.})=D_{2b}^{\mathrm{MS}}(\mathrm{corr.})$ are the simulations at high temperatures and $c = 4$ m. These simulations are precisely affected by a large dispersion of the data, and, therefore, the disagreement may not be significative.

4.5 Conclusions

We have computed MS as well as Fick diffusion coefficients of CO_2 in brine at thermodynamic conditions representative of deep saline aquifers using MD simulations. To achieve his goal, Einstein and GK formulations have been used.

To test the accuracy of the chosen intermolecular potentials for the different species, validation tests were performed for NaCl-water and CO_2-water systems. For aqueous ionic solutions, WN Lennard-Jones parameters for ion-ion interactions were chosen as they reproduce better electrolytic solution densities for high salt concentrations than Dang set of LJ parameters. Simulation results for

MS diffusion coefficients of ions in water agree with experimental data (mean deviation $\approx$ 10%) and with WN simulation results. Simulated MS diffusivities of Na^+ in Cl^- did not have the correct trend with salt concentration. The calculated electrical conductivity of aqueous NaCl was also compared to experimental data. Although for low salt concentrations our results are in agreement with experiments, electrical conductivity is under predicted for 4 m salt concentrations. Simulated MS diffusion coefficients of CO_2 in water were computed at $P = P_{\text{atm}}$ and $P > P_{\text{atm}}$. Results were compared with experiments and with values obtained using Wilke-Chang correlation. For $P = P_{\text{atm}}$, simulation results at $T = 298.15$ K agree with experiments, while results at $T = 283.15$ K have a deviation of 25% from experiments. This observed deviation was due to the low number of CO_2 molecules present in the system (2 and 3, respectively). For $P > P_{\text{atm}}$ a mean deviation of 18% was obtained between our simulation results and Wilke-Chang correlation results. It was an expected result as the Wilke-Chang correlation gives the mutual diffusion coefficient at infinite dilution.

The next step was the calculation of CO_2 MS diffusion coefficient in brine. The influence of temperature, CO_2 concentration and salinity was analyzed. MS diffusivities increase with temperature. For all fixed pressures, no effect of CO_2 pressure was observed. The evaluated MS diffusion coefficient show a small dependence with the salinity. Electrical conductivity of CO_2-brine mixtures was also computed for all thermodynamic conditions using Einstein and GK formulations. As observed for MS diffusivities, electrical conductivities are clearly functions of salinity, increasing when the salt concentration increases. No CO_2 concentration dependence for electrical conductivity was clearly observed. Finally, simulated electrical conductivities at $T = 333.15$ K and $c = 1$ m and 2 m were compared with values obtained using Fleury-Deschamps correlation. A shift is observed between simulation and correlation values.

MS diffusivity dependence with CO_2 concentration is a known difficult trend to determine not only by molecular simulation but also experimentally. We have proposed a correlation to estimate the diffusion coefficient based on the variation of the product $\tau^{l}_{\text{C=O}} D^{\text{self}}_{\text{CO}_2}$, as a function of the system density. In this case, we were able to correlate our simulation results to predict the self diffusion coefficient and MS diffusion coefficient with about 10% to 15% of absolute deviation. However, both experimental and simulated Fick diffusion coefficients of even simple mixtures present large fluctuations with the quantity of CO_2 dissolved. In the literature, Zabala et al.[163] compared simulated Fick binary diffusion coefficients of CO_2 dissolved in nC10 as a function of x_{CO_2} at saturation with experimental data.[201] Large average deviations with respect to the experimental data were also observed. Even experimental data presented large fluctuations. Hence, if we take into account that our system contains ions, it is not surprising to see dispersed values at plotting MS diffusion coefficients as a function of CO_2 concentration as we have obtained from MD simulations.

Although at low temperature D_{2b}^{MS} decrease when increasing salt concentration, this trend is not observed for higher temperatures. However, computed self diffusion coefficients decrease when increasing salt concentration at all temperatures and pressures. Hence, as CO_2 is present in the mixture at low dilution, D_{2b}^{MS} should follow the same trend.

Chapter 5

Conclusions

This thesis is divided into two well-defined parts. On the one hand, I undertake the study of the structure and dynamics of water confined inside $Mo_{132}(SO_4)$ and $Mo_{132}(HCO_2)$ polyoxometalates, and, on the other hand, the study of the diffusion of CO_2 in aqueous ionic solutions. Both analyses have been performed using classical molecular dynamics simulations with suitable models for the potential fields of the molecules. Here we give the most important conclusions of each part.

In the first chapter, we have studied the structure and dynamics of water confined inside a $Mo_{132}(SO_4)$ polyoxomolybdate molecular cluster at ambient conditions. The obtained radial density profiles of water oxygens indicate that the three-dimensional hydrogen bond network present in bulk water is distorted inside the cavity where water organizes instead in concentric layered structures. Hydrogen bonding, tetrahedral order and orientational distribution analyses indicate that water molecules form three hydrogen bonds with other molecules to stabilize the layered structure, while the remaining hydrogen bond bridges neighboring layers. We thus have proposed, based on the previous argument, that these layered structures should belong to the buckyball family, that is, structures with 12 pentagons, imposed by the external cast induced by the geometry of the cavity, and a variable number of hexagons. The analysis of the dynamics of water indicates that the main modes of motion at short times are correlated fluctuations of the entire system with a characteristic frequency. The transfer of water molecules between layers are events that rarely occur during the simulation. We have observed that the jump of a given particle from one layer to another necessarily involves the simultaneous switch of in fact two water molecules at neighboring layers. At long times, the system shows a power law decay (pink noise) in the fluctuations in the number of water molecules in shells containing the structures and the total dipole moment as well. Finally, some of the dynamic results, have been compared to experimental data and theoretical analyses done in reverse micelles of similar size. A slower decay of the dynamics of water inside $Mo_{132}(SO_4)$ is observed, for instance, from rotational correlation functions, which can be tested experimentally, indicating the more rigid nature of water inside these nanocapsules as compared to reverse micelles.

The effect of the ligand on the structural and dynamical properties of encapsulated water inside Mo_{132}(ligand) has been studied by replacing the sulfate ligands (SO_4^{2-}) by formate ligands (HCO_2^-). Radial and spatial distribution function analyses at ambient conditions show that water oxygen atoms occupy a new position next to the outermost water layer not observed when sulfates were inside the capsule. Then, the well-defined buckyball structures observed in the

$Mo_{132}(SO_4)$ POM are not formed in this case, although a given structure for water molecules still remains due to the constraints imposed by the confining surface. The analysis of the HB statistics and the tetrahedral parameter also agree with that view. However, when the temperature is decreased to 198 K, we observe that water molecules tend to form buckyball structures which agree with X-ray measurements at these conditions. We attribute the different scenario observed, at both temperatures, with respect to the simulation results for the $Mo_{132}(SO_4)$, to the lower volume and lower van der Waals repulsion of HCO_2^- ligands as compared to SO_4^{2-} ligands, as well as to the electrostatic attraction between the negatively charged water oxygen atoms and the positive hydrogen and carbon atoms of the formate ligand, which lead water molecules to occupy a new position under the pores inside the $Mo_{132}(HCO_2)$ capsule. The less structured spatial distribution function at $T = 298$ K for the $Mo_{132}(HCO_2)$ has as a consequence that water molecules diffuse much faster in the latter than inside the $Mo_{132}(SO_4)$ capsule. This behavior is observed from the analysis of the mean-squared displacement and the variation of the position of water oxygen atoms with time. In this case, the transfer of water molecules between different regions inside the $Mo_{132}(HCO_2)$ capsule is observed for all confined water molecules. The effect of the less constrained environment present when formates are the chosen ligand, has also been studied by means of rotational correlation functions and compared to that of reverse micelles of similar size. The obtained results indicate that water molecules have more freedom to rotate than inside the $Mo_{132}(SO_4)$ capsule. At the same time the reorientational dynamics of water inside the $Mo_{132}(HCO_2)$ become then similar to that observed for the more mobile water molecules inside reverse micelles of similar size.

Finally, the comparative analyses between the two sulfate and formate capsules reveal a strong sensitivity of the structure to the details of the inner side of the cavity that can suggest a coupling between the constraints due to the confinement and the two suggested forms of water, high density and low density water, even at ambient conditions.

The last chapter of the thesis is devoted to the calculation of mass diffusion coefficients of CO_2 in brine at thermodynamic conditions representative of deep saline aquifers. We have studied the influence of temperature, CO_2 concentration and salinity on the MS diffusion coefficient. We observe an increase of the Maxwell-Stefan diffusion coefficient with the temperature, but no clear dependence is identified with the salinity or CO_2 mole fraction. In this case, we noticed an important dispersion on the values of the obtained quantities leading to the calculation of the diffusion coefficient which impairs any conclusive statement about the effect of the gas concentration on the mobility of the CO_2 molecules. Rotational relaxation times for water and CO_2 increase by decreasing the temperature or increasing the salt concentration. We have proposed a correlation for the self-diffusion coefficient in terms of the rotational relaxation time, which can ultimately be used to estimate mutual diffusion coefficient of CO_2 in brine. Electrical conductivity of the CO_2-brine mixtures has also been calculated under different thermodynamic conditions. Electrical conductivity tends to increase with the temperature and salt concentration. However, we do not observe any influence of this property with the CO_2 concentration. The simulated electrical conductivities at 333.15 K and 1 and 2 molal have been compared with the Fleury-Deschamps correlation, with a good qualitative agreement. In general, the simulation results follow the same temperature variation of this property as the estimate from the Fleury-Deschamps correlation, but a slight shift is identified at low salinity. Our results give a first evaluation of CO_2-brine mass diffusion coefficient, rotational relaxation times, and electrical conductivity under the thermodynamic conditions typically encountered in deep saline aquifers, with the subsequent interest for industrial applications.

Appendix A

A.1 Calculation of the molar volume and hydrodynamic radius of CO_2

The specific volume of the CO_2 molecule, $v_{\mathrm{CO_2}}$ model for the EPM2 model is the sum of the colored volumes of Figure A.1. Knowing that the volume of a spherical cap of height h for a sphere of radius R is $V = \frac{\pi}{3}h^2(3R - h)$, and following the nomenclature explained in Figure A.1, the specific volume $v_{\mathrm{CO_2}}$ is computed as follows,

$$v_{\mathrm{CO_2}} = V_1 + V_2 + V_3 \tag{A.1}$$

If we analyze each term for separated we have that,

- V_1 is the volume of a sphere of radius R_{O} : $V_1 = \frac{4\pi}{3}R_{\mathrm{O}}^3$.
- V_2 is the volume of a sphere of radius R_{O} minus twice the volume of a spherical cap of height h' for a sphere of radius R_{O} :

$$V_2 = \frac{4\pi}{3}R_{\mathrm{O}}^3 - 2\left[\frac{\pi}{3}h'^2(3R_{\mathrm{O}} - h')\right] \tag{A.2}$$

- V_3 is the volume of an sphere of radius R_{C} minus the overlap of this sphere with the other two of radius R_{O}; that is twice the volume of a spherical cap of height h_c for a sphere of radius R_{C}, twice the volume of a spherical cap of height h_O for a sphere of radius R_{O} and we have to subtract at the end the overlapping of the two spheres of radius R_{O}:

$$\begin{aligned} V_3 &= \frac{4\pi}{3}R_{\mathrm{C}}^3\left[2\left(\frac{\pi}{3}h_c^2(3R_{\mathrm{C}}-h_c)\right)+2\left(\frac{\pi}{3}h_O^2(3R_{\mathrm{O}}-h_cO)\right)\right] \\ &\quad -\frac{4\pi}{3}R_{\mathrm{C}}^3\left[2\left(\frac{\pi}{3}h'^2(3R_{\mathrm{O}}-h')\right)\right] \end{aligned} \tag{A.3}$$

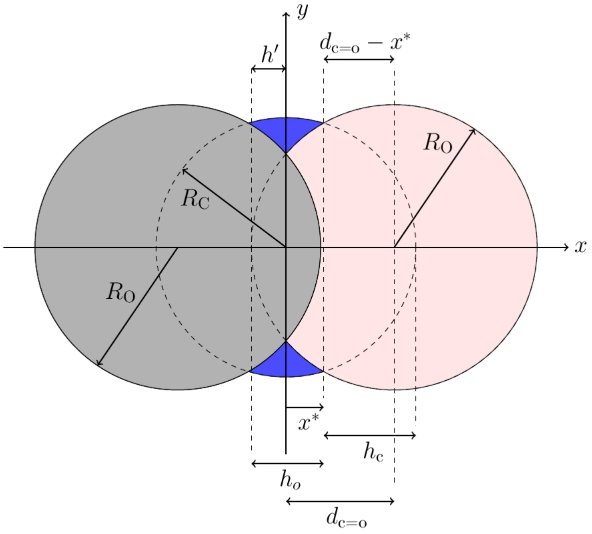

Figure A.1: Atomic geometry of the EPM2 model of CO_2. $R_{\mathrm{C}} = \sigma_{\mathrm{C}}/2$ and $R_{\mathrm{O}} = \sigma_{\mathrm{O}}/2$ and $d_{\mathrm{C=O}}$ is the bond length between O and C atoms. Note that in this model $R_{\mathrm{O}} > d_{\mathrm{C=O}}$, so there is overlapping between the two oxygens. The intersection of carbon and oxygen spheres occurs at abcisses $\pm x^*$. We call V_1 the volume of the gray sphere, V_2 the pink volume and V_3 the blue volume.

If we sum the three terms we obtain the specific volume $v_{\mathrm{CO_2}}$:

$$v_{\mathrm{CO_2}} = \frac{4\pi}{3}(R_{\mathrm{C}}^3 + 2R_{\mathrm{O}}^3) - 2\left(\frac{\pi}{3}h_c^2(3R_{\mathrm{C}}-h_c)\right) - 2\left(\frac{\pi}{3}h_O^2(3R_{\mathrm{O}}-h_O)\right) \tag{A.4}$$

Using the following relations,

$$h_c = R\mathrm{C} - x^* \tag{A.5}$$

$$h_O = R_{\mathrm{O}} - (d_{\mathrm{C=O}} - x^*) \tag{A.6}$$

$$h' = R_{\mathrm{O}} - d_{\mathrm{C=O}} \tag{A.7}$$

$$x^* = \frac{(d^2_{\mathrm{C=O}} + R^2_{\mathrm{C}} - R^2_{\mathrm{O}})}{2d_{\mathrm{C}}} \tag{A.8}$$

where x^* has been calculated from the intersection of one of the spheres of radius R_{O} with the sphere of radius R_{C}, and rearranging the terms, the equation A.4 becomes,

$$\begin{aligned} v_{\mathrm{CO_2}} = \frac{4\pi}{3}(R^3_{\mathrm{C}} + 2R^3_{\mathrm{O}}) - 2[\frac{\pi}{12d_{\mathrm{C=O}}}(R_{\mathrm{O}} + R_{\mathrm{C}} - d_{\mathrm{C=O}})^2(d^2_{\mathrm{C=O}} + \\ +2d_{\mathrm{C=O}}R_{\mathrm{C}} - 3R^2_{\mathrm{C}} + 2d_{\mathrm{C=O}}R_{\mathrm{O}} + 6R_{\mathrm{O}}R_{\mathrm{C}} - 3R^2_{\mathrm{O}})] \end{aligned} \tag{A.9}$$

Using the LJ parameters of the EPM2 model ($R_{\mathrm{C}} = \sigma_{\mathrm{C}}/2 = 1.3785$ Å and $R_{\mathrm{O}} = \sigma_{\mathrm{O}}/2 = 1.5165$ Å) we obtain a value of 29.1936 Å^3.

The hydrodynamic radius of CO_2 is estimated as the radius of a sphere having the same volume as $v_{\mathrm{CO_2}}$,

$$R_{\mathrm{CO_2}} = \sqrt[3]{\frac{3}{4\pi}v_{\mathrm{CO_2}}} \tag{A.10}$$

we have obtained a value of 1.9101 Å.

A.2 Correlation between self-diffusion coefficient and the rotational relaxation time

We can use the values of $D^{\mathrm{self}}_{\mathrm{CO_2}}$ and $\tau^{l}_{C=O}$ obtained in our simulation results for $\mathrm{CO_2}$ dissolved in brine to evaluate the equation 4.37. The resulting fitting can be observed in Figure A.2.

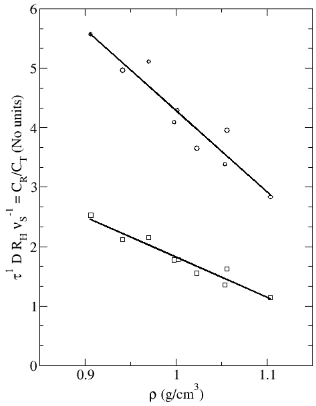

Figure A.2: Variation of the coefficient C_R/C_T in function of the density for $l = 1$ (circles) and $l = 2$ (squares) at 100 bar. Lines are fitting to the simulation data.

A.3 Simulation data for aqueous NaCl solutions

Table A.1: Results for MS diffusivities for aqueous NaCl, $T = 298.15$ K, $P = 1.013$ bar.

c(m)	$D_{\mathrm{Na-Cl}}$ Einst. /GK	$D_{\mathrm{w-Na}}$ Einst. /GK	$D_{\mathrm{w-Cl}}$ exp. /GK	D_{Na} $_{-\mathrm{Cl}}$ exp.	D_{w} $_{-\mathrm{Na}}$ exp.	D_{w} $_{-\mathrm{Cl}}$ exp.	dev. $D_{\mathrm{Na/Cl}}$ Eins. /GK(%)	dev. $D_{\mathrm{w/Na}}$ Eins. /GK(%)	dev. $D_{\mathrm{w/Cl}}$ Eins. /GK(%)
1	0.140	1.086	1.796	0.126	1.179	2.000	11.11	7.88	10.20
	/0.155	/0.996	/2.040				/23.02	/15.52	/2.00
2.5	0.202	0.850	1.542	0.232	0.947	1.705	12.93	10.24	9.56
	/0.129	/0.977	/1.650				/44.40	/3.20	/3.20
4	0.051	0.409	1.564	0.295	0.758	1.411	82.71	46.04	10.84
	0.051	0.450	1.500				/82.71	/39.50	/6.30

Table A.2: Results for electrical conductivity of aqueous NaCl, $T = 298.15$ K, $P = 1.013$ bar.

c(m)	κ Eins. (S/cm)	κ GK (S/cm)	κ exp. (S/cm)	dev. κ Eins.-exp (%)	dev. κ GK-exp (%)	dev. κ WN-exp (%)
1	0.085	0.082	0.076	11.84	7.89	3.69
2.5	0.137	0.117	0.159	13.84	26.42	34.50
4	0.159	0.158	0.212	25.00	25.47	44.10

A.4 Simulation data for CO_2-brine mixtures

In this subsection, we provide the simulation results for the diffusion of CO_2 in brine, as well as the calculated electrical conductivities of that mixture at the selected thermodynamic conditions.

Table A.3: Results for CO_2/brine mixture, $c = 1$ m, $T = 333.15$ K. The number of water molecules, N_w, is 3000 for all cases.

P (bar)	N_{CO_2}	ρ (g/ cm^3)	$D^{\mathrm{self}}_{\mathrm{CO}_2}$ (10^{-9} m^2/s)	D^{MS}_{2b} Eins. /GK (10^{-9}m^2/s)	dev D^{MS}_{2b} Eins. /GK (10^{-9}m^2/s)	κ. Eins. /GK (S/cm)	dev κ Eins. /GK (S/cm)	Q	D_{22} Eins. /GK (10^{-9}m^2/s)
50	29	1.019	3.76	3.81 /3.69	2.0 /2.5	0.071 /0.090	0.014 /0.019	0.900	3.43 /3.32
100	45	1.023	3.70	5.15 /4.45	0.6 /1.1	0.095 /0.099	0.019 /0.043	0.847	4.36 /3.77
200	54	1.028	3.82	3.24 /3.14	0.6 /1.5	0.103 /0.097	0.002 /0.007	0.819	2.65 /2.57
500	67	1.043	3.60	3.67 /3.85	0.7 /1.0	0.095 /0.106	0.008 /0.009	0.781	2.87 /3.01

Table A.4: Results for CO_2/brine mixture, $c = 1$ m, $T = 393.15$ K.

P (bar)	N_{CO_2}	N_w	ρ (g/ cm^3)	$D^{self}_{CO_2}$ (10^{-9} m^2/s)	D^{MS}_{2b} Eins. /GK (10^{-9}m^2/s)	dev D^{MS}_{2b} Eins. /GK (10^{-9}m^2/s)	κ. Eins. /GK (S/cm)	dev κ Eins. /GK (S/cm)	Q	D_{22} Eins. /GK (10^{-9}m^2/s)
50	20	3250	0.964	7.22	7.24 /7.20	4.0 /1.6	0.163 /0.146	0.041 /0.080	0.936	6.78 /6.74
100	32	3000	0.970	8.44	6.77 /6.71	0.1 /1.0	0.172 /0.160	0.089 /0.100	0.890	6.03 /5.97
200	48	3000	0.976	7.99	8.78 /7.95	0.3 /1.4	0.160 /0.155	0.026 /0.012	0.839	7.37 /6.67
500	69	3000	0.994	8.05	6.35 /5.75	0.2 /2.5	0.164 /0.193	0.039 /0.053	0.777	4.93 /4.47

Table A.5: Results for CO_2/brine mixture, $c = 1$ m, $T = 453.15$ K. The number of water molecules, N_w, is 3000 for all cases.

P (bar)	N_{CO_2}	ρ (g/ cm^3)	$D^{self}_{CO_2}$ (10^{-9} m^2/s)	D^{MS}_{2b} Eins. /GK (10^{-9}m^2/s)	dev D^{MS}_{2b} Eins. /GK (10^{-9}m^2/s)	κ. Eins. /GK (S/cm)	dev κ Eins. /GK (S/cm)	Q	D_{22} Eins. /GK (10^{-9}m^2/s)
50	15	0.903	13.60	13.07 /11.67	6.0 /6.0	0.222 /0.231	0.038 /0.046	0.949	12.40 /11.07
100	31	0.906	12.49	15.45 /16.08	6.0 /6.0	0.201 /0.212	0.069 /0.015	0.896	13.84 /14.41
200	54	0.912	12.68	12.49 /11.60	4.0 /6.0	0.246 /0.230	0.120 /0.110	0.825	10.31 /9.57
500	91	0.933	12.25	13.90 /13.81	1.0 /0.5	0.226 /0.244	0.057 /0.078	0.725	10.07 /10.01

Table A.6: Results for CO_2/brine mixture, $c = 2$ m, $T = 333.15$ K. The number of water molecules, N_w, is 3000 for all cases.

P (bar)	N_{CO_2}	ρ (g/ cm^3)	$D_{CO_2}^{self}$ (10^{-9} m^2/s)	D_{2b}^{MS} Eins. /GK (10^{-9}m^2/s)	dev D_{2b}^{MS} Eins. /GK (10^{-9}m^2/s)	κ. Eins. /GK (S/cm)	dev κ Eins. /GK (S/cm)	Q	D_{22} Eins. /GK (10^{-9}m^2/s)
50	24	1.051	2.85	2.69 /2.64	0.6 /0.4	0.182 /0.161	0.037 /0.071	0.917	2.47 /2.42
100	37	1.054	2.95	2.67 /2.21	0.2 /0.4	0.192 /0.193	0.042 /0.040	0.874	2.33 /1.93
200	45	1.060	3.63	2.33 /2.38	0.4 /0.1	0.138 /0.157	0.006 /0.010	0.848	1.98 /2.02
500	56	1.072	2.78	2.78 /2.82	1.5 /1.5	0.191 /0.220	0.014 /0.006	0.815	2.27 /2.30

Table A.7: Results for CO_2/brine mixture, $c = 2$ m, $T = 393.15$ K. The number of water molecules, N_w, is 3000 for all cases.

P (bar)	N_{CO_2}	ρ (g/ cm^3)	$D^{self}_{CO_2}$ (10^{-9} m^2/s)	D^{MS}_{2b} Eins. /GK (10^{-9}m^2/s)	dev D^{MS}_{2b} Eins. /GK (10^{-9}m^2/s)	κ. Eins. /GK (S/cm)	dev κ Eins. /GK (S/cm)	Q	D_{22} Eins. /GK (10^{-9}m^2/s)
50	15	0.999	5.27	7.61 /7.25	4.0 /5.0	0.297 /0.305	0.110 /0.130	0.948	7.21 /6.87
100	27	1.002	6.44	6.41 /6.26	0.2 /0.3	0.237 /0.245	0.012 /0.001	0.907	5.81 /5.68
200	39	1.008	5.59	6.96 /6.15	3.4 /1.9	0.237 /0.237	0.068 /0.088	0.868	6.04 /5.34
500	57	1.023	7.50	7.80 /8.14	1.7 /1.6	0.256 /0.265	0.041 /0.019	0.814	6.35 /6.63

Table A.8: Results for CO_2/brine mixture, $c = 2$ m, $T = 453.15$ K. The number of water molecules, N_w, is 3000 for all cases.

P (bar)	N_{CO_2}	ρ (gr/ cm^3)	$D^{self}_{CO_2}$ (10^{-9} m^2/s)	D^{MS}_{2b} Eins. /GK (10^{-9}m^2/s)	dev D^{MS}_{2b} Eins. /GK (10^{-9}m^2/s)	κ. Eins. /GK (S/cm)	dev κ Eins. /GK (S/cm)	Q	D_{22} Eins. /GK (10^{-9}m^2/s)
50	12	0.938	13.31	11.05 /10.04	4.6 /4.5	0.308 /0.337	0.025 /0.011	0.959	10.60 /9.64
100	25	0.941	10.4	11.89 /9.23	1.6 /2.5	0.340 /0.347	0.005 /0.018	0.916	10.89 /8.45
200	44	0.947	10.25	11.54 /9.69	0.7 /2.8	0.374 /0.347	0.121 /0.111	0.856	9.88 /8.29
500	73	0.965	8.66	10.06 /9.15	2.5 /3.5	0.269 /0.302	0.056 /0.096	0.775	7.80 /7.09

Table A.9: Results for CO_2/brine mixture, $c = 4$ m, $T = 333.15$ K. The number of water molecules, N_w, is 3000 for all cases.

P (bar)	N_{CO_2}	ρ (gr/ cm^3)	$D^{\mathrm{self}}_{\mathrm{CO_2}}$ (10^{-9} m^2/s)	D^{MS}_{2b} Eins. /GK (10^{-9}m^2/s)	dev D^{MS}_{2b} Eins. /GK (10^{-9}m^2/s)	κ. Eins. /GK (S/cm)	dev κ Eins. /GK (S/cm)	Q	D_{22} Eins. /GK (10^{-9}m^2/s)
50	17	1.104	2.40	3.02 /2.92	1.0 /1.0	0.184 /0.197	0.025 /0.045	0.941	2.84 /2.78
100	27	1.107	2.22	2.58 /2.22	0.7 /0.7	0.223 /0.209	0.066 /0.100	0.907	2.34 /2.01
200	32	1.111	2.68	2.15 /2.00	0.3 /0.1	0.184 /0.175	0.068 /0.047	0.890	1.91 /1.78
500	42	1.123	2.31	2.67 /2.45	0.1 /0.2	0.273 /0.289	0.039 /0.002	0.859	2.29 /2.10

Table A.10: Results for CO_2/brine mixture, $c = 4$ m, $T = 393.15$ K. The number of water molecules, N_w, is 3000 for all cases.

P (bar)	N_{CO_2}	ρ (gr/ cm^3)	$D^{self}_{CO_2}$ (10^{-9} m^2/s)	D^{MS}_{2b} Eins. /GK (10^{-9}m^2/s)	dev D^{MS}_{2b} Eins. /GK (10^{-9}m^2/s)	κ. Eins. /GK (S/cm)	dev κ Eins. /GK (S/cm)	Q	D_{22} Eins. /GK (10^{-9}m^2/s)
50	11	1.054	5.06	5.52 /5.11	1.5 /1.7	0.359 /0.365	0.078 /0.058	0.961	5.31 /4.91
100	20	1.056	5.20	6.00 /5.16	1.3 /2.1	0.376 /0.446	0.078 /0.020	0.931	5.59 /4.80
200	30	1.061	7.17	5.44 /4.62	1.0 /1.0	0.400 /0.448	0.112 /0.148	0.898	4.89 /4.15
500	42	1.074	4.82	6.00 /5.49	0.9 /0.8	0.394 /0.356	0.090 /0.051	0.861	5.17 /4.73

Table A.11: Results for CO_2/brine mixture, $c = 4$ m, $T = 453.15$ K. The number of water molecules, N_w, is 3000 for all cases.

P (bar)	N_{CO_2}	ρ (gr/ cm^3)	$D^{self}_{CO_2}$ (10^{-9} m^2/s)	D^{MS}_{2b} Eins. /GK (10^{-9}m^2/s)	dev D^{MS}_{2b} Eins. /GK (10^{-9}m^2/s)	κ. Eins. /GK (S/cm)	dev κ Eins. /GK (S/cm)	Q	D_{22} Eins. /GK (10^{-9}m^2/s)
50	9	0.996	8.33	12.80 /13.12	6.0 /8.0	0.391 /0.380	0.230 /0.240	0.969	12.40 /12.71
100	18	0.998	8.23	9.28 /8.89	2.6 /1.8	0.424 /0.460	0.094 /0.038	0.939	8.71 /8.35
200	32	1.003	9.03	12.40 /12.40	2.0 /3.0	0.368 /0.316	0.031 /0.119	0.894	11.09 /11.09
500	54	1.019	8.49	17.27 /17.25	6.0 /4.0	0.538 /0.540	0.191 /0.174	0.831	14.34 /14.33

A.5 Comparison of CO_2-brine conductivities with Fleury-Deschamps correlation

Table A.12: Comparison between simulation and correlation data for electrical conductivity of CO_2/brine mixtures, $c = 1$ m, $T = 333.15$ K.

$x_{\mathrm{CO_2}}$	κ Eins./GK (S/cm)	κ corr. (S/cm)	dev (sim-corr) Eins./GK (%)
0.094	0.071/0.090	0.128	44.53/29.69
0.0145	0.095/0.099	0.124	23.39/20.16
0.0174	0.103/0.097	0.122	15.57/20.49
0.0215	0.095/0.106	0.118	19.49/10.17

Table A.13: Comparison between simulation and correlation data for electrical conductivity of CO_2/brine mixtures, $c = 2$ m, $T = 333.15$ K.

$x_{\mathrm{CO_2}}$	κ Eins./GK (S/cm)	κ corr. (S/cm)	dev (sim-corr) Eins./GK (%)
0.0076	0.182/0.161	0.237	23.21/32.07
0.0117	0.192/0.193	0.231	16.88/16.45
0.0142	0.138/0.157	0.227	39.21/30.84
0.0176	0.191/0.220	0.222	13.96/0.90

A.6 Simulation data for water and CO_2 rotational relaxation times

Table A.14: Results for rotational relaxation times, $c = 1$ m, $P = 100$ bar

T(K)	τ_1^{μ} (ps)	τ_2^{μ} (ps)	τ_1^{HH} (ps)	τ_2^{HH} (ps)	$\tau_1^{\perp}$ (ps)	$\tau_2^{\perp}$ (ps)	$\tau_1^{\mathrm{C=O}}$ (ps)	$\tau_2^{\mathrm{C=O}}$ (ps)
333.15	3.361	0.984	2.544	1.184	1.665	0.705	1.550	0.658
393.15	1.620	0.455	1.146	0.530	0.780	0.322	0.950	0.400
453.15	0.965	0.268	0.650	0.302	0.452	0.192	0.700	0.310

Table A.15: Results for rotational relaxation times, $c = 2$ m, $P = 100$ bar

T(K)	τ_1^{μ} (ps)	τ_2^{μ} (ps)	τ_1^{HH} (ps)	τ_2^{HH} (ps)	$\tau_1^{\perp}$ (ps)	$\tau_2^{\perp}$ (ps)	$\tau_1^{\mathrm{C=O}}$ (ps)	$\tau_2^{\mathrm{C=O}}$ (ps)
333.15	3.980	1.130	2.740	1.340	1.814	0.797	1.800	0.720
393.15	1.830	0.520	1.230	0.590	0.845	0.363	1.050	0.435
453.15	1.086	0.302	0.700	0.337	0.486	0.215	0.750	0.320

Table A.16: Results for rotational relaxation times, $c = 4$ m, $P = 100$ bar

T(K)	τ_1^{μ} (ps)	τ_2^{μ} (ps)	τ_1^{HH} (ps)	τ_2^{HH} (ps)	$\tau_1^{\perp}$ (ps)	$\tau_2^{\perp}$ (ps)	$\tau_1^{\mathrm{C=O}}$ (ps)	$\tau_2^{\mathrm{C=O}}$ (ps)
333.15	5.180	1.487	3.175	1.730	2.134	1.018	2.000	0.808
393.15	2.214	0.620	1.401	0.718	0.976	0.437	1.195	0.490
453.15	1.290	0.353	0.785	0.390	0.550	0.250	0.780	0.340

List of Publications

- M. Garcia-Ratés, P. Miró, J. M. Poblet, C. Bo, and J. Bonet Avalos, *Dynamics of Encapsulated Water inside* Mo_{132} *cavities*, J. Phys. Chem. B **115**, 5980 (2011).
- M. Garcia-Ratés, J. C. de Hemptinne, J. Bonet Avalos, and C. Nieto-Draghi, *Molecular modeling of diffusion coefficient and ionic conductivity of* CO_2 *in aqueous ionic solutions*, J. Phys. Chem. B (submitted).
- M. Garcia-Ratés, P. Miró, J. M. Poblet, C. Bo, and J. Bonet Avalos, *The effect of the ligand on the structure and the dynamics of encapsulated water inside* Mo_{132} *cavities*, J. Phys. Chem. B (submitted).

Bibliography

1. R. K. Pathria, *Statistical Mechanics*, 2nd ed. (Butterworth Heinemann, Oxford, 1996).
2. D. Frenkel, and B. Smith, *Understanding Molecular Simulation, from Algorithms to Applications*, 2nd ed. (Academic, San Diego, 1996).
3. M. P. Allen, and D. J. Tildesley, *Computer Simulation of Liquids*, 1st ed. (Clarendon, Oxford, 1989).
4. M. Griebel, S. Knapek, and G. Zambusch, *Numerical Simulation in Molecular Dynamics: Numerics, Algorithms, Parallelization, Applications.* (Springer, Heidelberg, 2007).
5. D. Eisenberg, and W. Kauzmann, *The Structure and Properties of Water.* (Oxford University Press, New York, 1969).
6. K. A. Dill, and S. Bromberg, *Molecular driving forces: statistical thermodynamics in chemistry and biology.* (Garland Science, New York, 2003).
7. J. Marti, G. Nagy, E. Guardia, and M. C. Gordillo, J. Phys. Chem. B **110**, 23987 (2006).
8. L. Huang, L. Zhang, Q. Shao, J. Wang, L. Lu, X. Lu, S. Jiang, and W. Shen, J. Phys. Chem. B **110**, 25761 (2006).
9. O. Byl, J. Liu, Y. Wang, W. Yim, J. K. Johnson, and J. T. Yates, Jr, J. Am. Chem. Soc. **128**, 12090 (2006).
10. J. Shiomi, T. Kimura, and S. Maruyama, J. Phys. Chem. C **111**, 12188 (2007).

11. P. L. Luisi, and B. E. Straub, *Reverse Micelles: Biological and Technological Relevance of Amphiphilic Structures in Apolar Media* (Plenum, New York, 1984).
12. T. De, and A. Maitra, Adv. Colloid Interface Sci. **59**, 95 (1995).
13. N. Levinger, Science **298**, 5599 (2002).
14. J. Faeder, and B. M. Ladanyi, J. Phys. Chem. B **104**, 1033 (2000).
15. D. E. Rosenfeld, and C. A. Schmuttenmaer, J. Phys. Chem. B **110**, 14304 (2006).
16. P. A. Pieniazek, Y.-S. Lin, J. Chowdhary, B. M. Ladanyi, and J. L. Skinner, J. Phys. Chem. B **113**, 15017 (2009).
17. M. R. Harpham, B. M. Ladanyi, N. E. Levinger, and K. W. Herwig, J. Chem. Phys. **121**, 7855 (2004).
18. M. T. Pope, and A. Müller, *Polyoxometalates: From Platonic Solids to Anti-Retroviral Activity.* (Kluwer Academic Publishers, Dordrecht, 1994).
19. D. L. Long, Tsunashima, and L. Cronin, Angew. Chem. **49**, 1736 (2010).
20. T. Mitra, P. Miro, A. R. Tomsa, A. Merca, H. Bögge, J. B. Avalos, J. M. Poblet, C. Bo, and A. Müller, Chem. Eur. J. **15**, 1844 (2009).
21. E. Brosse, Pétrole et Techniques, **435**, 50 (2001).
22. Z. Li, M. Dong, S. Li, and L. Dai, J. Chem. Eng. Data **49**, 1026 (2004).
23. R. Krishna, and J. A. Wesselingh, Chem. Eng. Sci. **52**, 861 (1997).
24. R. Krishna, and J. M. van Baten, Ind. Eng. Chem. Res. **44**, 6939 (2005).
25. R. Taylor, and R. Krishna, *Multicomponent Mass Transfer*, (John Wiley & Sons, Inc:, New York, 1993).
26. H. J. C Berendsen, J. R. Grigera, and T. P. Straasma, J. Phys. Chem. **91**, 6269 (1987).
27. D. R. Wheeler, and J. Newman, J. Phys. Chem. B **108**, 18353 (2004).
28. J. G. Harris, and K. H. Yung, J. Phys. Chem. **99**, 12021 (1995).

29. H. Goldstein, *Classical Mechanics*, 3rd ed. (Addison-Wesley, San Francisco, 2002).

30. A. D. Sokal, *Monte Carlo Methods in Statistical Mechanics: Foundations and New Algorithm*, Lectures at the Càrgese Summer School on *Functional Integration: Basics and Applications*, Càrgese, 1996.

31. W. Smith, and T. R. Forester, J. Mol. Graph. **14**, 136 (1996).

32. D. P. Landau, and K. Binder, *A Guide to Monte Carlo Simulations in Statistical Physics*, 2nd ed. (Cambridge University Press, Cambridge, 2005).

33. J. P. Ryckaert, G. Cicotti, and H.J.C. Berendsen, J. Comput. Phys. **23**, 327 (1977).

34. D. J. Evans, Molec. Phys. **34**, 317 (1977).

35. D. Fincham, Mol. Sim. **8**, 165 (1992).

36. L. V. Woodcock, Chem. Phys. Lett. **10**, 257 (1971).

37. H. C. Andersen, J. Chem. Phys. **72**, 2384 (1980).

38. S. Nosé, Mol. Phys. **52**, 255 (1984).

39. W. G. Hoover, Phys. Rev. **A31**, 1695 (1985).

40. S. Melchionna, G. Ciccotti, and B. L. Holian, Molec. Phys. **78**, 533 (1993).

41. A. R. Leach, *Molecular Modelling, Principles and Applications*, (Longman, London, 1996)

42. J. P. Hansen, and I. R. McDonald, *Theory of Simple Liquids*, 2nd ed. (Academic, London, 1991).

43. C. L. Kong, J. Chem. Phys. **59**, 2464 (1973).

44. M. Waldman, and A. T. Hagler, J. Comput. Chem. **14**, 1077 (1993).

45. J. Delhommelle, and P. Millié, Molec. Phys. **99**, 619 (2001).

46. P. P. Ewald, Ann. Phys. **64**, 253 (1921).

47. K. Esselink, Comp. Phys. Comm. **87**, 375 (1995).

48. P. Ungerer, B. Tavitian, and A. Boutin, *Applications of molecular simulation in the oil and gas industry. Monte Carlo Methods.* (Ed. Technip, Paris, 2005).

49. W. L. Jorgensen, J. D. Madura, and C. J. Swenson, J. Am. Chem. Soc. **106**, 813 (1984).

50. B. Smit, S. Karaborni, and J. I. Siepmann, J. Chem. Phys. **102**, 2126 (1995).

51. M. G. Martin, and J. I. Siepmann, J. Phys. Chem. B **102**, 2569 (1998).

52. J. M. Haile, *Molecular Dynamics Simulation, Elementary Methods*, (John Wiley and Sons, New York, 1992).

53. A. H. Narten, and H. A. Levy , J. Chem. Phys. **55**, 2263 (1971).

54. Y. E. Gorbaty, and Y. N. Demianets, Mol. Phys. **55**, 571 (1985).

55. G. Hura, J. M. Sorenson, R. M. Glaeser, and T. Head-Gordon, J. Chem. Phys. **113** 9140 (2000).

56. A. K. Soper, F. Bruni, and M. A. Ricci, J. Chem. Phys. **106**, 247 (1997).

57. I. T. Jolliffe, *Principal Component Analysis, 2nd ed. (Springer-Verlag, New York, 2002).*

58. M. Chapling, *Water structure and science* (http://www.lsbu.ac.uk/water/index2.html), (2003).

59. L. Pauling, *The Nature of the Chemical Bond*, 2nd ed. (Cornell University Press, New York, 1948).

60. F. Bartha, O. Kapuy, C. Kozmutza, and C. Van Alsenoy, J. Mol. Struct. (Teochem) **666-667**, 117 (2003).

61. T. H. Plumridge, G. Steele, and R. D. Waigh, Phys. Chem. Comm. **8**, (2000).

62. X. -B. Wang, X. Yang, J. B. Nicholas, and L. -S. Wang, Science **294**, 1322 (2001).

63. P. E. Mason, J. M. Cruikshank, G. W. Neilson, and P. Buchanan, Phys. Chem. Chem. Phys. **5**, 4686 (2003).

64. O. N. Pestova, Yu. P. Kostikov, and M. K. Khripun, Russian J. Appl. Chem. **77**, 1066 (2004).

65. C. Tanford, *The hydrophobic effect*, 2nd ed. (Wiley, New York, 1980).

66. F. Franks, *Water, a comprehensive treatise.* (Plenum Press, New York, 1972).

67. H. E. Stanley, and J. Teixeira, J. Chem. Phys. **73**, 3404 (1980).

68. G. S. Kell, J. Chem. Eng. Data **12**, 66 (1967).

69. P. J. Lindstrom, and W. G. Mallard, NIST Chemistry WebBook, NIST Standard Reference Data Number 69, (2005).

70. K. E. Bett, and J. B. Cappi, Nature **207**, 620 (1965).

71. T. DeFries, and J. Jonas, J. Chem. Phys. **66**, 896 (1977).

72. C. A. Angell, E. D. Finch, and P. Bach, J. Chem. Phys. **65**, 3065 (1976).

73. E. F. Burton, and W. F. Oliver, Proc. Roy. Soc. London Ser. A **153**, 166 (1936).

74. O. Mishima, L. D. Calvert, and E. Whalley, Nature **310**, 393 (1984).

75. O. Mishima, L. D. Calvert, and E. Whalley, Nature **314**, 76 (1985).

76. P. H. Poole, T. Grande, F. Sciortino, H. E. Stanley, and C. A. Angell, J. Comp. Mat. Sci. **4**, 373 (1995).

77. G. Franzese, and H. E. Stanley, J. Phys.: Cond. Mat. **14**, 2201 (2002).

78. G. Franzese, and H. E. Stanley, Physica A **314**, 508 (2002).

79. G. Franzese, and H. E. Stanley, J. Phys.: Cond. Mat. **14**, 2193 (2002).

80. G. Franzese, M. I. Marques, and H. E. Stanley, Phys. Rev. E **67**, 011103 (2003).

81. G. Franzese, and H. E. Stanley, J. Phys.: Cond. Mat. **19**, 205126 (2007).

82. S. Sastry, P. Debenedetti, F. Sciortino, and H. E. Stanley, Phys. Rev. E **73**, 6144 (1996).

83. P. H. Poole, F. Sciortino, U. Essmann, and H. E. Stanley, Nature **360**, 324 (1992).

84. R. J. Speedy, J. Phys. Chem. **86**, 982 (1982).

85. C. A. Angell, Science **319**, 582 (2008).

86. K. Stokely, M. G. Mazza, H. E. Stanley, and G. Franzese, Proc. Natl. Acad. Sci. U.S.A. **107**, 107 (2010).

87. A. Rahman, and F. H. Stillinger, J. Chem. Phys. **55**, 3336 (1971).

88. A. Ben-Naim, and F. H. Stillinger in *Water and Aqueous Solutions.* (ed. R. A. Horne, Wiley Interscience, New York, 1972).

89. F. H. Stillinger, and A. Rahman, J. Chem. Phys. **60**, 1545 (1974).

90. A. Glättli, X. Daura, and W. F. van Gunsteren, J. Chem. Phys. **116**, 9811 (2002).

91. K. Krynicki, C. D. Green, and D. W. Sawyer, Faraday Discuss. Chem. Soc, **66**, 199 (1978).

92. *Handbook of Chemistry and Physics*, (ed. R. C. Weast, CRC, Boca Raton, 1976).

93. O. Teleman, B. Jönsson, and S. Engström, Mol. Phys. **74**, 193 (1987).

94. A. Wallqvist, and O. Teleman, Mol. Phys. **74**, 515 (1991).

95. L. X. Dang, and B. M. Pettitt, J. Phys. Chem. **91**, 3349 (1987).

96. I. G. Tironi, R. M. Brunne, and W. F. van Gunsteren, Chem. Phys. Lett. **250**, 19 (1996).

97. E. Sanz, C. Vega, J. L. F. Abascal, and L. G. MacDowell, Phys. Rev. Lett. **92**, 255701 (2004).

98. W. L. Jorgensen, J. Chandrasekhar, J. D. Madura, R. W. Impey, and M. L. Klein, J. Chem. Phys. **79**, 926 (1983).

99. W. N. Lipscomb, Inorg. Chem. **4**, 132 (1965).

100. M. T. Pope, ibid. **11**, 952 (1977).

101. C. F. Clark, and D. H. Hall, Acta Crystallogr. **B32**, 1545 (1976).

102. V. W. Day, M. F. Fredrich, and W. G. Klemperer, J. Am. Chem. Soc. **99**, 952 (1977).

103. A. Müller, and C. Serain, Acc. Chem. Res. **33**, 2 (2000).

104. A. Müller, E. Krickemeyer, H. Bögge, M. Schmidtmann, and F. Peters, Angew. Chem., Int. Ed. **37**, 3360 (1998).

105. A. Ziv, A. Grego, S. Kopilevich, L. Zeiri, P. Miró, C. Bo, A. Müller, and I. A. Weinstock, J. Am. Chem. Soc. **131**, 6380 (2009).

106. a) P. Ball, H_2O: *A Biography of Water*, Weidenfeld & Nicolson, London 1999; b) P. Ball, Chem. Rev. **108**, 74 (2008); c) P. Ball, Cell. Mol. Biol. **47**, 717 (2001); d) P. Ball, Nature **452**, 291 (2008).

107. a) M. F. Chaplin, Biophys. Chem. **83**, 211 (2000) ; b) M. F. Chaplin, Nat. Rev. Mol. Cell Biol. **7**, 861 (2006).

108. N. Giovambattista, P. G. Debenedetti, and P. J. Rossky, Phys. Rev. Lett. **102**, 050603 (2009).

109. G. Hummer, and A. Szabo, Proc. Natl. Acad. Sci. U.S.A. **98**, 3658 (2001).

110. D. Donadio, G. Cicero, E. Schwegler, M. Sharma, and G. Galli, J. Phys. Chem. B. **113**, 4170 (2009).

111. P. M. Wiggins, Microbiol. Rev. **54**, 432 (1990).

112. P. M. Wiggins, Cell. Mol. Biol. **47**, 735 (2001).

113. P. H. Poole, F. Sciortino, U. Essmann, and H. E. Stanley, Nature **360**, 324 (1992).

114. S. T. Harrington, R. Zhang, P. H. Poole, F. Sciortino, and H. E. Stanley, Phys. Rev. Lett. **78**, 2409 (1997).

115. S. T. Harrington, P. H. Poole, F. Sciortino, and H. E. Stanley, J. Chem. Phys. **107**, 7443 (1997).

116. H. Tanaka, Phys. Rev. E **62**, 6968 (2000).

117. H. Tanaka, Phys. Rev. Lett. **80**, 5750 (1998).

118. H. Tanaka, J. Chem. Phys. **11**, 799 (2000).

119. M. Rovere, and P. Gallo, Eur. Phys. J. E. **12**, 77 (2003).

120. M. Rovere, M. A. Ricci, D. Vellati, and F. Bruni, J. Chem. Phys. **108**, 23 (1998).

121. A. Malani, K. G. Ayappa, and S. Murad, J. Phys. Chem. B **113**, 13825 (2009).

122. D. S. Venables, K. Huang, and C. A. Schmuttenmaer, J. Phys. Chem. B **105**, 9132 (2001).

123. G. Onori, and A. Santucci, J. Phys. Chem. **97**, 5430 (1993).

124. I. R. Piletic, D. E. Moilanen, D. B. Spry, N. E. Levinger, and M. D. Fayer, J. Phys. Chem. A. **110**, 4985 (2006).

125. A. M. Dokter, S. Woutersen, and H. J. Bakker, Proc. Natl. Acad. Sci. U.S.A. **103**, 15355 (2006).

126. P. Gallo, M. Rovere, and, E. Spohr, Phys. Rev. Lett. **85**, 4317 (2000).

127. P. Gallo, M. Rovere, and E. Spohr, J. Chem. Phys. **113**, 11324 (2000).

128. N. Nandi, and B. Bagchi, J. Phys. Chem. B **101**, 10954 (1997).

129. J. Faeder, and B. M. Ladanyi, J. Phys. Chem. B **105**, 11148 (2001).

130. C. Hartnig, W. Witschel, E. Spohr, P. Gallo, M. A. Ricci, and M. Rovere, J. Mol. Liq. **85**, 127 (2000).

131. M. Zulauf, and H.-F. Eicke, J.Phys. Chem. **83**, 480 (1979).

132. R. Ludwig, and A. Appelhagen, Angew. Chem. Int. Ed. **44**, 811 (2005).

133. V. Chihaia, S. Adams, and W. F. Kuhs, Chem. Phys. **297**, 271 (2004).

134. M. Sasai, I. Ohmine, and R. Ramaswamy, J. Chem. Phys. **96**, 3045 (1991).

135. A. Müller, H. Bogge, and E. Diemann, Inorg. Chem. Commun. **6**, 52 (2003).

136. L. Euler, *Elementa doctrine solidorum*, (Novi Comentarii academiae scientarum imperialis petropolitanae **4**, 109-160, 1752-1753).

137. The $g(r)$ calculated in ref [20] is proportional to the number of water molecules in a given layer instead of the density, as in this work. Therefore, the former corresponds to $4\pi r^2 \rho_{\mathrm{b}} g(r)$.

138. A. Luzar, D. Chandler, J. Chem. Phys. **98**, 8160 (1993).

139. E. Guardia, J. Marti, J. A. Padro, L. Saiz, and A. V. Komolkin, J. Mol. Liq. **96**, 3 (2002).

140. S. Mukamel, *Principles of Nonlinear Optical Spectroscopy*, (Oxford, New York, 1995).

141. S. Park, and M. D. Fayer, Proc. Natl. Acad. Sci. U.S.A. **104**, 16731 (2007).

142. In this mapping we have used the local field instead of the effective field, given in ref [16], due to the fact that the definition of this effective field refers to ions that are not present in our system. Then, we have thus followed the same approach as in ref [143].

143. Y.-S. Lin, B. M. Auer, and J. L. Skinner, J. Chem. Phys. **131**, 144511 (2009).

144. P. L. Chau, and A. Geiger, Mol. Phys. **103**, 511 (1999).

145. X. Lopez, C. Nieto-Draghi, C. Bo, J. B. Avalos, and J. M. Poblet, J. Phys. Chem. A **109**, 1216 (2005).

146. F. Leroy, P. Miro, J. M. Poblet, C. Bo, and J. B. Avalos, J. Phys. Chem. B **112**, 8591 (2008).

147. A. Chaumont, and G. Wipff, Phys. Chem. Chem. Phys. **10**, 6940 (2008).

148. P. Miro, J. M. Poblet, J. B. Avalos, and C. Bo, Can. J. Chem. **87**, 1296 (2009).

149. A. Chaumont, and G. Wipff, J. Phys. Chem. C **113**, 18233 (2009).

150. A. K. Rappe and W. A. Goddard, J. Phys. Chem. **95**, 3358 (1991).

151. IPCC Third Assessment Report: Climate Change 2001. Cambridge University Press. (2001).

152. T. B. Johansson, R. H. Williams, H. Ishitani, and J. A. Edmonds, Energy Policy **24**, 985 (1996).

153. S. Bachu, W. D. Gunter, and E. H. Perkins, Energy Convers. Managt. **35**, 269 (1994).

154. S. Bachu, Energy. Convers. Managt. **41**, 953 (2000).

155. B. Hitchon, W. D. Gunter, T. Gentzis, and R. T. Bailey, Energy Convers. Managt. **40**, 825 (1999).

156. R. Korbol, and A. Kaddour, Energy Convers. Managt. **36**, 509 (1995).

157. D. J. White, G. Burrowes, T. Davis, Z. Hajnal, K. Hirsche, I. Hutcheon, E. Majer, B. Rostron, and S. Whittaker, *Greenhouse gas sequestration in abandoned oil reservoirs: The International Energy Agency Weyburn pilot project*, GSA Today, 14, 4 (2004).

158. Information has been taken from http://www.albertaasap.com

159. S. Portier, *Solubilité de CO_2 dans les saumures des bassins sédimentaires, PhD Thesis*, Strasbourg (2005).

160. H. Oeschger, U. Siegenthaler, U. Schotterer, and A. Gugelmann, Tellus, **27**, 168 (1975).

161. E. Maier-Reimer, and K. Hasselmann, Climate Dynamics, **2**, 63 (1987).

162. V. Lagneau, A. Pipart, and H. Catalette, Oil & Gas Science and Technology-Rev. IFP, **60**, 231 (2005).

163. D. Zabala, C. Nieto-Draghi, J.-C de Hemptinne, and A. Lopez de Ramos, J. Phys. Chem. B **112**, 16610 (2008).

164. S. Kjeltsup, D. Bedeaux, E. Johannessen, and J. Gross, *Non-equilibrium thermodynamics of engineers*, (World Scientific, New Jersey, 2010).

165. a) W. G. Rothschild, *Dynamics of Molecular Liquids*, (Wiley, New York, 1984); b) B. J. Berne, and R. Pecora, *Dynamic Light Scattering*, (Wiley, New York, 1976); c) R. Fleming, *Chemical Applications of Ultrafast Spectroscopy*, (Oxford University Press, New York, 1986).

166. J. McConell, *The Theory of nuclear Magnetic Relaxation in Liquids*, (Cambridge University, Cambridge, 1987).

167. M. Holz, R. Haselmeier, A. J. Dyson, and H. Huber, Phys. Chem. Chem. Phys. **2**, 1717 (2000).

168. T. Umecky, M. Kanakubo, and Y. Ikushima, J. Phys. Chem. B **107**, 12003 (2002).

169. H. Versmold, Mol. Phys. **43**, 383 (1981).

170. F. Kohlrausch, Pogg. Ann. **119**, 337 (1863).

171. G. Williams, and D. C. Watts, Trans. Faraday Soc. **66**, 80 (1970).

172. I. Soreide, and C. Whitson, Fluid Phase Equilib. **77**, 217 (1992).

173. M. Pekka, and N. Lennart, J. Phys. Chem. A **105**, 9954 (2001).

174. E. Guardia, D. Laria, and J. Marti, J. Mol. Liq. **125**, 107114 (2006).

175. E. Guardia, J. Marti, and J. A. Padro, Theor. Chem. Acc. **115**, 161169 (2006).

176. E. Guardia, D. Laria, and J. Marti, J. Phys. Chem. B **110**, 6332 (2006).

177. E. Guardia, J. Marti, L. Garcia-Tarres, and D. Laria, J. Mol. Liq. **117**, 6367 (2005).

178. L. X. Dang, J. Am. Chem. Soc. **117**, 6954 (1995).

179. Z. Duan, and R. Sun, Chem. Geo. **193**, 257 (2003).

180. D. M. Himmelblau, Chem. Rev. **64**, 527 (1964).

181. A. K. Saha, S. Bandyopadhyay, and A. K. Biswas, J. Chem. Eng. Data **38**, 78 (1993).

182. A. Tamini, E. B. Rinker, and O. C. Sandall, J. Chem. Eng. Data **39**, 330 (1994).

183. G. F. Versteeg, and W. P. M. Van Swaalj, J. Chem. Eng. Data **33**, 29 (1988).

184. C. R. Wilke, and P. Chang, Am. Inst. Chem. Eng. J. **1**, 264 (1955).

185. W. Hayduk, and H. Laudie, Am. Inst. Chem. Eng. J. **20**, 611 (1974).

186. M. T. Tyn, and W. F. Calus, Processing **21**, 16 (1975).

187. M. Fleury, and H. Deschamps, J. Chem. Eng. Data **53**, 2505 (2008).

188. T. W. Chapman, *The Transport Properties of Concentrated Electrolytic Solutions, Ph. D. Thesis*, University of California (1967).

189. J. F. Davidson, and M. A. Cullen, A. Trans. Inst. Chem. Eng. **35**, 51 (1957).

190. International Critical Tables, McGraw-Hill Book Co., vol. 3, pp. 259 (1928).

191. L. Diamond, and N. Akinfiev, Fluid Phase Equilib. **208**, 265 (2003).

192. M. Lisal, W. R. Smith, and K. Aim, Fluid Phase Equilib. **226**, 161 (2004).

193. J. Marti, G. Nagy, E. Guardia, and M. C. Gordillo, J. Phys. Chem. B, **110**, 23987 (2006).

194. E. Guardia, and J. Marti, J. Phys. Rev. E **69**, 11502 (2004).

195. L. S. Darken, Trans. Am. Inst. Mining Metall. Eng. **175**, 184 (1948).

196. C. S. Caldwell, and A. L. Babb, J. Phys. Chem. **60**, 51 (1956).

197. B. Bagchi, J. Chem. Phys. **115**, 2207 (2001).

198. S. Ravichandran, and B. Bagchi, J. Chem. Phys. **111**, 7505 (1999).

199. M. P. Allen, P. J. Camp, C. P. Monson, G. T. Evans, and A. J. Masters, J. Chem. Phys. **105**, 11175 (1996).

200. I. C. Yeh, and G. J. Hummer, J. Phys. Chem. B **108**, 15873 (2004).

201. A. T. Grogan, V. W. Pinczewski, G. Ruskauff, and F. M. Orr Jr, SPE Reservoir Engineering, **83**, 14897 (1988).